Imperial College London

Centre of Research Excellence
British Heart Foundation
Imperial College London

Assessment of the Nano-mechanical Properties of Healthy and Atherosclerotic Coronary Arteries by Atomic Force Microscopy

Fotios Savvopoulos, CID: 01158471

This thesis is submitted for the degree of Master of Philosophy (MPhil) of Imperial College London

Copyright Declaration

Statement of Originality

I hereby declare that this submission is my own work and contains no material previously published, except where due acknowledgement has been made in the text.

Fotios Savvopoulos

Abstract

Coronary atherosclerosis is a major cause of mortality and morbidity worldwide. Despite its systemic nature, atherosclerotic plaques form and develop at "predilection" sites often associated with disturbed biomechanical forces. Therefore, computational approaches that analyse the biomechanics (blood flow and tissue mechanics) of atherosclerotic plaques have come to the forefront over the last 20 years. Assignment of appropriate material properties is an integral part of the simulation process. Current approaches for derivation of material properties rely on macro-mechanical testing and are agnostic to local variations of plaque stiffness to which collagen microstructure plays an important role. In this work we used Atomic Force Microscopy to measure the stiffness of healthy and atherosclerotic coronary arteries and we hypothesised that are those are contingent on the local microstructure. Given that the optimal method for studying mechanics of arterial tissue with this method has not been comprehensively established, an indentation protocol was firstly developed and optimised for frozen tissue sections as well as a co-registration framework with the local collagen microstructure utilising the same tissue section for mechanical testing and histological staining for collagen. Overall, the mechanical properties (Young's Modulus) of the healthy vessel wall (median = 11.0 kPa, n=1379 force curves) were found to be significantly stiffer ($p=1.34 \cdot 10^{-10}$) than plaque tissue (median=4.3 kPa, n=1898 force curves). Within plaques, lipid-rich areas (median=2.2 kPa, n=392 force curves) were found significantly softer ($p=1.47 \cdot 10^{-4}$) than areas rich in collagen, such as the fibrous cap (median=4.9 kPa, n=1506 force curves). No statistical difference (p=0.89) was found between measurements in the middle of the fibrous cap (median=4.8 kPa, n=868 force curves) and the cap shoulder (median=5.1 kPa, n=638 force curves). Macro-mechanical testing methods dominate the entire landscape of material testing techniques. Plaques are very heterogenous in composition and macro-mechanical methods are agnostic to microscale variations in plaque stiffness. Mechanical testing by indentation may be better suited to quantify local variations in plaque stiffness, that are potent drivers of plaque rupture.

Acknowledgements

This thesis is the result of many years of work and would not have been possible without the help of many people I would like to take this opportunity to thank them for all their contributions.

First and foremost, I would like to thank my supervisors, Dr. Ranil de Silva and Prof. Rob Krams, for their support over the last four years. Also, I would like to thank Dr. Núria Gavara and Dr. Michael Keeling for their patient guidance in this new field that I found myself in. I am hugely indebted to British Heart Foundation Centre of Research Excellence which funded my research.

I would also like to thank the members of my research group Miten Patel, Dr. Nicholas Fogell, Jarka Naser for creating a safe space for me to express my ideas and also their support and understanding during some difficult times. Also, it would be an omission not to acknowledge previous members of the lab, Roza Nikolopoulou, Danai Kati, Roosje Ruis, as well as members of the Weinberg lab for our long discussions and some fun times we had together: Kai Riemer, Dr. Yean Chooi, Dr. Zahra Mohri, Dr. Eleni Bazigou, Dr. Ethan Rowland.

I would like to thank the QMUL team, Prof Rob Krams, Alex Delahunty, Sean Herault, Dr. Danielle Carassiti, Dr. Russell Bailey (AFM facility), Dr. Jan Soertaert (Blizard Institute).

A huge thank you to my therapists, Dr. Agorastos Agorastos and Ms. Mary Fitzerald for keeping me accountable and helping me to structure my routine during extended periods of lockdown which shielded myself against potential relapses of depression.

This list wouldn't be complete without mentioning my friends Dr. Karlos Kazinakis and Dr. Christina Salpingidou and my family. They believed in me at times that it was difficult to believe in myself.

I dedicate this thesis to all people in academia fighting silently against depression.

Fotios Savvopoulos

Table of Contents

List of Figures

Secondary flow crosswise main direction of flow. Large shear gradients in the outer curvature than inner curvature that is prone to separation. (D) flow profile distal branch ostium and regions of high and low shear. Shear is determined by the local velocity gradient and the local viscosity There is a temporal aspect to these profiles which here is simplified by taking steady flow. Figure reproduced from Winkel et al. (2015).

Figure 11 Pressure and flow waveforms of coronary arteries (LAD, LCx and RCA) during rest and light exercise. Figure reproduced from Kim et al. (2010)

Figure 12 Schematic of the biomechanical forces acting on a blood vessel in normalcy and advanced plaques. (A) Blood pressure and shear stress are externally applied (solid lines) and these result in internal loads i.e. axial stress and circumferential stress (dashed lines). (B) Forces on the normal vessel wall. (C) Schematic of a segment of the diseased wall with a fibroatheroma and resulting stress concentration. Reproduced from Pedrigi et al. (2014).

Figure 13 Stretch-activated signalling pathways in ECs contributing to a healthy and dysfunctional endothelium. Image reproduced from Jufri et al. (2015).

Figure 14 Signalling pathways and biochemical crosstalk between ECs and SMCs when exposed to disturbed flow and stretch. Adapted from Lu and Kassab (2011)

Figure 15 Imaging modalities to extract coronary plaque geometry (A) Magnetic Resonance imaging (resolution: 400μm) (B) intravascular ultrasound (resolution: 150-200μm), (C) Optical Coherence Tomography (resolution: 5-15μm), (D) Histology. To obtain more reliable estimates of in vivo plaque biomechanics both imaging and mechanical characterisation might need to take place at the microscale level. Combined image created from Barrett et al. (2019) and Tang et al. (2004).

Figure 16 Mechanical characterisation techniques and their area of probation scale. MMT: macro-mechanical testing, IND: indentation testing, AFM: atomic force microscopy, MRE: magnetic resonance elastography, OST: oscillatory shear testing. Figure adapted from Budday et al. (2019)

Figure 17 Summary of mechanical properties (circumferential stress – stretch) of human atherosclerotic intima from aortic, carotid, iliac and coronary arteries. Compression is unconfined. Note the much softer properties measured from micro-indentation test in Barrett et al. (2009) and Chai et al. (2013). Plot reproduced from Akyildiz, Speelman, and Gijsen (2014).

Figure 18 Overview of an atomic force microscope. (A) Experimental set-up: An inverted (epifluorescence or standard light) microscope sits on a vibration isolation table to minimise noise (B - top) Principle of measurement: a laser beam is continually focused on the back side of a cantilever that reflects towards a photodiode that measures voltage. The cantilever's vertical position (z) is measured by a piezoelectric transducer. While the cantilever indents a sample, it bends thereby altering the position of the laser spot on the photodiode which, in turn, generates a voltage proportional to the deflection of the cantilever. (B - bottom) Detail of the sample mounting area. The temperature and hydration of the sample can be regulated with a heating and perfusion systems. Figure adapted from Gautier et al. (2015).

Figure 19 A typical example of a force-curve with different stages of contact noted (1-5). Blue and red curves correspond to approach and retraction stages respectively. (1) approaching, (2) initial contact, and (3) repulsive contact until threshold Fi. (4) adhesion and (5) noncontact

regimes recorded upon retracting the cantilever and sample. Reproduced from Wonseok et al. (2016)

Figure 20 Contact models for most common tip geometries used for probing biological tissue. F: Force, E: Young's Modulus, v: Poisson's ratio, δ: indentation depth. Schematics adapted from Cárdenas-Pérez et al. (2019).

Figure 21 Stenotic stent. Figure reproduced from Foin et al. (2013).

Figure 22 Overview of the experimental and computational pipeline used to study the colocalization of disturbed biomechanics and advanced plaques. Material properties of coronary arteries are a necessary requirement for downstream computational modelling. In this work we used Atomic Force Microscopy as a high-resolution alternative to macroscale testing methods.

Figure 23 Details of the tissue substrate to enable mechanical testing and co-registration with collagen microstructure. (A) Sectional view of the testing substrate; grey: plastic petri dish, light grey: gridded coverslip, yellow: poly-L-lysine coating, red: tissue section, blue: PBS. (B) Detailed view of coverslip with 50μm imprinted grid.

Figure 24 The MNSL- 10 probe. A) The cantilevers of the chip A(0.07N/m), B(0.02N/m), C (0.01N/m), D(0.03N/m), E(0.1N/m), F(0.6N/m). Cantilevers E and F were used in the optimisation process B) SEM picture of tip of each of the cantilevers C) Diagram of the geometry of the tip with important dimensions noted D) Technical specifications of the cantilever E.

Figure 25 Topography experiment to determine optimal Z-length. Brightfield images of the selected indentation locations are shown. The cantilever in use is pointed with the yellow arrow. (L): lumen.

Figure 26 Effect of time on structural integrity of tissue assessed by Young's Modulus (top, left), indentation depth (top, right) and adhesion forces (bottom, left). The same indentation location consisting of a 5x5 grid (25 force curves) was measured at 6 timepoints. Temperature (~ 22^{o}C), scanning parameters and probe (legend) remained constant during the measurements. Bar heights and error bars represent average and standard deviation, respectively. Comparisons with paired t-test (*= $p< 0.05$, **: $p<0.01$, ***=$p<0.001$, n.s.: not significant).

Figure 27 Effect of the indentation speed on adhesion force. For each case multiple locations were measured, and the Results were pooled together: 2μm/sec - n=93 curves, 4μm/sec - n=137 curves, 6μm/sec n=98 curves. Bar heights and error bars represent average and standard deviation, respectively. All locations resided in the media layer.

Figure 28 Effect of force setpoint/threshold on indentation depth. 10, 15, 20nN correspond to Bar heights and error bars represent average and standard deviation, respectively. All locations resided in the media layer.

Figure 29 Effect of Optimal Cutting Temperature compound rinsing and tip contamination on adhesion forces. All measurements took place in the medial layer with measurement parameters as shown (right). (A) Clean cantilever (from package) and no rinsing step (n=144 curves), (B) Clean cantilever (from package) with rinsing step (n=255 curves), (C) second scan with cantilever from (B) with Optimal Cutting Temperature compound rinsed but not cleaned. The probe was not previously de-contaminated (n=245 curves) Bar heights and error bars

represent average and standard deviation, respectively. All locations resided in the media layer. Comparisons with paired t-test (*= p< 0.05, **: p<0.01, n.s.: not significant.

Figure 30 (A-E) Examples of force curves which were excluded from downstream analyses. For all graphs, X axis: Vertical tip position, Y axis: Relative Force, Light blue: extension curve, Dark blue: retraction curve.

Figure 31 (left) Raw force-displacement curve (or force curve) imported to JPKSPM Data Processing software. Y axis: Vertical deflection/ Force (nN), X axis: Height (μm). Light blue: extension, Dark blue: retraction. (top left) List of standard operations each denoted by a square. (right) Viewing parameters.

Figure 32 (left) Operation 1: Smoothing of raw curve. Y axis: Vertical deflection/ Force (nN), X axis: Height (μm). Light blue: extension, Dark blue: retraction. (right) The smoothing parameters remained constant across all force curves.

Figure 33 Operation 3: Correction of offset and tilt of baseline part of extension curve. As the force is always relative to a baseline, this baseline is subtracted from the entire curve. Please notice the difference in the numbering of the Y axis. Light blue curve: extension, dark blue curve: retraction. **(right)** Correction parameters.

Figure 34 Operation 4: Location of contact point. Please notice the change of X axis numbering. The zero point is where the contact point is estimated to be. Light blue curve: extension, dark blue curve: retraction.

Figure 35 Operation 8: Extraction of indentation depth (denoted as *Height* at 100% *Relative Force,* **down right**). Light blue curve: extension, dark blue curve: retraction.

Figure 36 Fitting of Hertzian contact model (light green curve) to the extension part of the force curve. Light blue curve: extension, dark blue curve: retraction.

Figure 37 Co-registration pipeline of AFM-derived mechanical properties with local collagen microstructure. The tissue section was laid on a coverslip with an imprinted square grid (size=50μm) that facilitated the co-registration process. The indentation locations (e.g. square H12) were selected on the basis of presumed collagen fibre density (dark bands) from bright-field images. (A) Brightfield image of the cantilever (triangular shape) with the measurement grid (yellow) before an indentation on square H12. (B) Force curve (black line) in 1 of the 25 locations of the measurement grid and contact model fit (YM=19.8 kPa, RMS=26 nN) is shown in green. (C, D) Stained tissue Picrosirius Red under (C) polarised light (different collours represent different thicknesses of collagen fibres) (E) Binary image after thresholding the red channel of (C) and derivation of collagen area density (=62%).

Figure 38 Co-registration pipeline from tissue mechanics to histology. (A) Brightfield image of a representative section from a healthy coronary artery (higher power images were combined to form a low power image). The square grid (square unit: 50μm x 50μm) imprinted on the coverslip where tissue was laid on enabled co-registration of tissue properties and histological metrics with high accuracy. (B) Brightfield image of the cantilever (triangular shape) and the tissue with the measurement grid. Twenty five (n=25) force curves were acquired within each ROI (e.g. C9). The collagen content of the targeted areas was measured post-hoc by staining with Picrosirius Red. (C, D) Stained tissue with Picrosirius Red under (C) brightfield and (D) polarised light with the ROI shown in yellow. (E) The polarised light colour image was converted to grayscale and it was thresholded to produce a binary image. ROI dimensions: 50μm x 50μm.

Figure 39 Analysis of raw force curves. (A) Raw force curve signal, dark blue: extension, light blue: retraction, (B) Smoothed force curve, (C) Extraction of Young's Modulus by fitting a

Hertzian contact model on the force curve (light green line). The contact point is defined where vertical tip position is zero. This force curve yields a modulus value of 4.2 kPa and root mean square of force residuals (Residual RMS) is 118.6 pN.

Figure 40 Box and whisker plot of Young's Modulus values stratified in four quartiles of collagen fibre density. Measurements conducted in media-intima layers. Lower whisker: first quartile, middle line: median, upper whisker: third quartile. No statistically significant differences were found between groups.

Figure 41 Frequency distribution of Young's modulus (A, B) and collagen fibre density values (C, D). Young's Modulus was found to follow a log-normal distribution, whereas collagen fibre density did not. (E) Scatter plot between log-normalised Young's Modulus and collagen fibre density. A positive (R^2=0.17, p=0.00143) correlation was found to relate the variables.

Figure 42 Representative examples of healthy coronary artery tissue sections stained with Picrosirius Red stain and imaged with linearly polarised light (dark field). Despite presence of red-hued noise, it can be observed that collagen is organised in thick bundles that align with the circumferential direction. Scale bar: 100μm.

Figure 43 Approach to co-registration of AFM measurement locations to the local collagen microstructure in atherosclerotic coronary plaques. (A) Brightfield image of a tissue section with indentation locations (50μm x 50μm) shown in yellow. (B) Same section stained with Picrosirius Red imaged with brightfield light, (C) Same section stained with Picrosirius Red imaged with linearly polarised light, (D) Adjacent section stained with Hematoxylin and Eosin, (E) Adjacent section stained with Oil-Red-O (lipids).

Figure 44 (left) Frequency distributions of log-normalised Young's Modulus values of different histology groups. (A) Healthy: blue, plaque: red. (B) Plaque: green, fibrous cap: red, lipid-rich: blue. Lipid-rich areas were defined as areas with <5% collagen density and with paucity of cells on H&E and high in lipid (red stain) in Oil-Red-O stain. (C) Updated scatterplot containing co-registered measurements of Young's Modulus and collagen fibre density in healthy tissue (n=57) sections and on fibrous cap (n=24) within diseased tissue sections. No correlation (R^2=0.008, p=0.1563) was found to relate the variables.

List of Tables

Abbreviations

2-D: two dimensional
3-D: three dimensional
ACS: acute coronary syndrome
AFM: atomic force microscopy
apo-E$^{-/-}$: apolipoprotein E-knockout
CAD: coronary artery disease
CFD: computational fluid dynamics
CVD: cardiovascular disease
EC(s): endothelial cell(s)
ECM: extracellular matrix
ET : endothelin
FD-OCT: fourier domain – optical coherence tomography
FEA: finite element analysis
FSI: fluid-structure interaction
GAG: glycosaminoglycan
HDL: high-density lipoprotein
ICAM : intercellular adhesion molecule
IFN : interferon
IL : interleukin
IVUS: intravascular ultrasound
LAD: left anterior descending artery
LCx: left circumflex coronary artery
LCCA: left common carotid artery
LDL: low-density lipoprotein
LSCM: laser scanning confocal microscopy
MCP : monocyte chemoattractant protein
MMP : matrix metalloproteinase
NADPH: nicotinamide adenine dinucleotide phosphate
NF-κB: nuclear factor kappa-light-chain-enhancer of activated B cells
NIRS: near-infrared spectroscopy
NO : nitric oxide
oxLDL: oxidised low-density lipoprotein
PDGF : platelet-derived growth factor;
PECAM-1: platelet endothelial cell adhesion molecule-1
PIT: pathological intimal thickening
PLM: polarised light microscopy
RCA: right coronary artery
RCCA: right common carotid artery
SALS: small-angle light scattering
SHG: second harmonic generation
SMC(s): smooth muscle cell(s)
SREBP : sterol regulatory elements binding protein
TCFA: thin cap fibro-atheroma
TF : transcription factor
TGF : transforming growth factor
ThCFA: thick cap fibroatheroma
TNF : tumour necrosis factor
t-PA : tissue plasminogen activator

TPFLM: two-photon fluorescence microscopy
US: ultrasound
VCAM: vascular cell adhesion factor
VEGF : vascular endothelial growth factor
VH-IVUS: virtual histology IVUS
μCT: micro-computed tomography

Motivation and Scope

Coronary atherosclerosis is a chronic, inflammatory disease of the cardiovascular system. Aside from systemic risk factors, such as low-density lipoprotein (LDL) cholesterol blood plasma levels, and genetic predispositions, local factors seem to be at play that lead to the patchy manifestation of the disease. Endothelial shear stress (ESS), i.e. the frictional force blood flow exerts on the inner most layer of the arterial wall, is distributed non-uniformly along the coronary vasculature. While forward laminar flow promotes vascular health, disturbed flow, native to inner side of curvatures and branch ostia gradually impairs endothelial function. At those sites the integrity of the endothelial barrier is compromised and becomes permeable to circulating LDL cholesterol particles that accumulate in the sub-endothelial layer constituting an early lesion or a "fatty streak". Over time the atheromatous process leads to the formation of an advanced atherosclerotic plaque. Early lesions are largely quiescent, but those that progress to the advanced stages display the highest risk for an acute coronary syndrome and sudden cardiac death – a diagnostic and patient risk management challenge for interventional cardiologists.

Advanced coronary plaque rupture accounts for the vast majority (60-75%) of sudden cardiac death cases in patients presenting with acute coronary syndrome. In the most fatal of cases, plaque rupture leads to coronary thrombosis that can totally occlude the arterial lumen that limits perfusion of the downstream cardiac muscle resulting in tissue necrosis and heart failure. According to histopathological reports, ruptured plaques exhibit a particular morphology. The innermost layer of the arterial wall, the intima, is considerably thickened encapsulating a large cholesterol-rich, acellular core surrounded by a thin, inflamed, collagen-rich fibrous cap (<65μm). In those plaques – termed as **vulnerable** – rupture occurs 60% of the time at the shoulder region (where fibrous cap meets the fibrous intima) and 40% at the thinnest point of the fibrous cap. Identification of morphological characteristics of advanced plaques with intracoronary imaging modalities such as intravascular ultrasound (IVUS) and optical coherence tomography (OCT) currently provide a low positive predictive value for prediction of acute coronary syndromes and more tools are warranted for that reason.

The sensitivity of the manifestation of the disease in areas of disturbed ESS has stimulated the development of approaches to obtain three-dimensional biomechanical profiling of coronary plaques in search of biomechanically "vulnerable" spots within coronary plaques. To fully define the biomechanics (mechanical stress) of a material requires knowledge of the geometry, material properties, externally applied loads. In most cases, this cannot be achieved analytically and, as a result, it requires the use of computational methodologies, such as finite element analysis (FEA), or more sophisticated methods such as fluid-structure interaction (FSI) that simulate the coupled interaction of blood flow and distension of the arterial wall in response to blood pressure. Previous computational attempts to simulate the mechanics of plaques (carotid, femoral, coronary) indicate that increased stress (concentrations) occurs at the interface of materials with different stiffness. Stress concentrations also rely on geometrical parameters such as the thickness of the fibrous cap and the size of the necrotic core. Such findings from histology-based geometries align with histopathological observations of ruptured plaques.

Although there has been considerable progress in the biomechanical modelling diseased vessels during the last 20 years, such pipelines are still away from application in the clinic. The Achilles' heel of contemporary modelling approaches is two-fold. Firstly, it is the widespread use of virtual histology IVUS (VH-IVUS) for 3-D reconstruction of coronary plaques for downstream biomechanical modelling. Despite being an *in vivo* modality, VH-IVUS is incapable of detecting vulnerable plaques due to its coarse resolution (150-200μm). Secondly, most computational models use material properties from tensile/ compressive testing which are agnostic to local variations of tissue stiffness and, as a result, limited to assess the effect of local changes in composition and structure on local tissue stiffness. According to pathohistological reports, soft (lipid) and stiff (collagen) components can be situated only a few microns apart which can lead to locally increased stress (stress concentration) and can advance to a plaque rupture. Unless higher resolution imaging modalities and material testing techniques are used, any attempts to refine plaque rupture thresholds is going is going to add little to our understanding of local factors driving plaque rupture and vulnerability.

To the degree that plaque rupture is a local phenomenon, where local material stresses exceed local material strength, accurate prediction of plaque rupture location in accordance with histological rupture depends primarily on two pillars: accurate geometrical reconstruction of vessels in health and disease and more detailed methods of measurement of material properties of coronary arteries. As for the latter, Atomic Force Microscopy is an alternative, *ex vivo,* material testing technique that measures local material properties by indentation. By utilising a high-resolution mechanical testing modality this work aims to provide nano-mechanical material properties of healthy and atherosclerotic coronary arteries which could be used refine material modelling approaches coming from macroscopic testing towards the generation of bio-inspired three-dimensional models of coronary arteries.

Chapter 1: Background

1. Acute Coronary Syndrome – a healthcare challenge

Coronary artery disease (CAD) is a chronic vascular disease that after years of indolent growth can manifest in an acute and life-threatening manner. According to the World Health Organisation's Global Health Atlas, 7.3 million people die annually from an acute coronary syndrome (ACS) rendering it the leading cause of mortality worldwide (Thomas et al. 2011). CAD is a local manifestation of atherosclerosis; a chronic, lipid-driven, systemic, inflammatory disease of the circulatory system.

Myocardial infarction and sudden cardiac death are the most common and often irreversible complications in patients with coronary artery disease. While it is encouraging that CVD-related mortality has almost halved from 80 deaths per 100,000 in 2005 to 46 per 100,000 in 2015 (Bhatnagar et al. 2016) in the United Kingdom that has largely resulted from the technological advancements in pharmaceutical treatment, early intervention underpinned by advances in pathways of care intervention equipment and intracoronary imaging. However, declining mortality rates cannot counteract the increasing prevalence of CAD in the general population (Fuster and Mearns 2009), as obesity and its consequences, diabetes mellitus, hypertension and hyperlipidemia, can put a growing proportion of the population at an increased risk of an ACS (Libby and Pasterkamp 2015).

1.1. Coronary plaque rupture as the primary mechanism for coronary thrombosis and sudden cardiac death

The hallmark of the atherosclerotic process is the formation of atherosclerotic plaque. After years of silent growth, atherosclerotic plaques are characterised by significant thickening of the vessel wall (expansive remodelling) with excessive build-up of oxidized LDL cholesterol accompanied by inflammatory cell infiltration, smooth muscle proliferation, and extracellular matrix deposition (Wentzel et al. 2012; Falk et al. 2013a). It takes several decades for early lesions to progress to advanced ones in the absence of premonitory symptoms. While early lesions are largely quiescent, it is those that progress to the advanced stages (atherosclerotic plaques) that display the highest

risk for an acute coronary syndrome; a diagnostic challenge for interventional cardiologists.

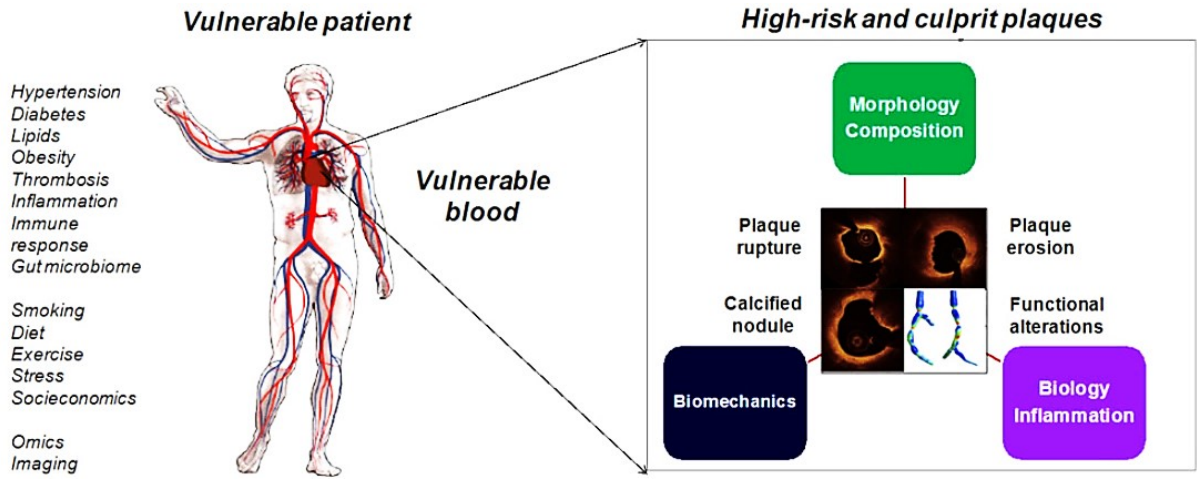

Figure 1 Major adverse cardiac events are likely to occur from development of vulnerable/ high risk plaques in vulnerable patients. A series of systemic risk factors (left) contribute to the cardiovascular health 'footprint" - the vulnerable blood. Due to the low specificity of systemic risk factors to predict MACE, the interplay of local risk factors such as anatomical plaque features, biomechanics and biochemical profile could improve the prediction of an acute coronary syndrome. Figure reproduced from Tomaniak et al. (2020).

The primary life-threatening event in advanced atherosclerosis is when plaques become thrombosed whereby plaque contents create a lumen-occluding thrombus upon contact with the bloodstream. There are four main mechanisms according to which advanced plaque can destabilise (**Figure 1**) and trigger a myocardial infarction (Tomaniak et al. 2020):

- **Plaque rupture** is the primary pathophysiological mechanism underlying ACS and accounts for the vast majority (~50-75%) of acute cases.
- In **plaque erosion** there is a disruption of the thrombogenic - thrombolytic equilibrium in the blood that if combined with a dysfunctional or absent endothelium they can create a fertile ground for spontaneous thrombus formation. Much less is known about plaque erosion that is responsible for ~20-40% of fatal coronary thrombi.
- The least common cause of coronary thrombosis is due to a heavily calcified plaque (**calcified nodule**).

– A fourth mechanism of thrombosis is through functional coronary alterations (e.g. in-stent thrombosis after revascularization)

At present the most detailed evidence regarding thrombosed plaques comes from retrospective autopsy studies (Falk et al. 2013b). According to those studies, plaques exhibiting expansive remodelling with a large lipid-rich acellular core and a thin and inflamed fibrous cap, were predominantly found to instigate thrombosis. Therefore, there seems to be some characteristics which render some plaques more vulnerable to rupture - henceforth will be referred to as rupture-prone - than others and the mechanisms which promotes these characteristics over others are still obscure.

1.2. Emergence of biomechanics as a local risk factor

A long list of systemic (genetic and environmental) risk factors can put people at an increased risk of an ACS (**Figure 1**, left). It has been now established that atherosclerosis is a lipid-driven disease; high levels (>0.39 mmol/l of circulating LDL in the blood plasma are sufficient to initiate and sustain the disease (Glass and Witztum 2001) even in the absence of other risk factors. Cigarette smoking, hypertension and LDL have been long known to contribute to overall cardiovascular vulnerability. Now, patients with an history of obesity and its consequences (diabetes mellitus, hypertension, dyslipidemia) and high triglycerides and low high-density lipoprotein (HDL), either in absolute terms or as a proportion of proportion of LDL, as well as women represent an increasing proportion of patients suffering from ACS (Libby and Pasterkamp 2015).

While systemic risk factors play a central role in determining a generic cardiovascular vulnerability and constitute important therapeutic targets for general cardiovascular health, their predictive specificity for an ACS is limited. In the last forty years the treatment strategies have shifted considerably from treating the stenotic aspect of plaques (coronary revascularisation or PCI) to a more holistic approach of estimating an overall ACS risk as a result of the complex interplay of immunobiology, anatomical and biochemical plaque features and thrombosis propensity of blood (**Figure 2**).

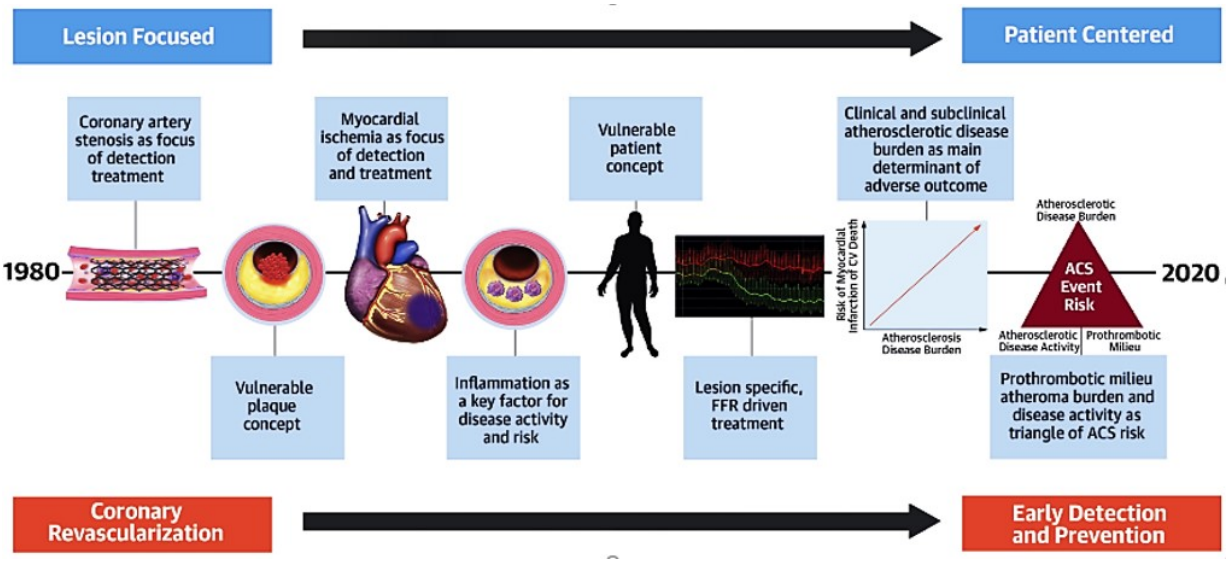

Figure 2 Evolution of treatment strategies for coronary artery disease in the last forty years. In the 1980s strategies were focused on the treatment of coronary stenosis but a greater understanding of the mechanisms of the disease has shifted the attention to a combination of local (disease burden) and systemic (inflammation and thrombosis biomarkers) to arrive to a patient-centred strategy. Figure reproduced from Arbab-Zadeh and Fuster (2019).

Technological advances in invasive and non-invasive imaging of coronary plaque have improved the understanding of the morphology of plaques *in vivo* (Bourantas et al. 2017a). The most widespread intracoronary imaging modalities are IVUS and OCT. Until recently, imaging precursors of culprit plaques based on the above modalities have had a low predictive value for an ACS. An imaging modality that is an exception to that is near-infrared spectroscopy intravascular ultrasound (NIRS-IVUS). Quite recently, it was demonstrated that NIRS-IVUS can identify plaques at risk for an ACS during a 24-month period (Waksman et al. 2019) in a large (n=1547 patients) prospective intracoronary imaging study. More multi-modality catheters are under development to further detect local markers of inflammation and molecular imaging (Bourantas et al. 2017b). In the field of pharmacotherapy, improved compounds have been developed to reduce cholesterol, thrombosis risk, and inflammation, however acute events continue to occur in patients receiving innovative and aggressive treatments (Ridker et al. 2017). It is the low specificity of systemic biomarkers to indicate the location and phenotype of a vulnerable plaque that promoted advancement of interdisciplinary approaches one of which is the field of plaque biomechanics.

The tendency of coronary artery disease to develop at arterial sites, namely inner sides of curvatures, bifurcations and branching points associated with disturbed blood

flow indicates that there may be risk factors related to the local arterial biomechanical environment creating a fertile ground for the disease. It is widely known that endothelial cells (ECs) are mechano-sensitive (i.e. they convert mechanical signals to biochemical ones). ECs are exposed to ESS; the frictional force blood flow exerts on the endothelium. While laminar ESS (forward flowing and physiological magnitude) promotes endothelial and vascular health, disturbed ESS (of altered magnitude and/or direction) has been long known to upregulate a series of proinflammatory, proatherogenic, molecules ultimately rendering the endothelial barrier permeable to LDL cholesterol (Frangos, Gahtan, and Bauer 1999; Koskinas et al. 2009; Winkel et al. 2015; Thondapu et al. 2017). In advanced stages, low ESS augments the expression of tissue disruptive enzymes (matrix metalloproteinases or MMPs) and thereby promotes the formation of thin-capped atheromata (Shah et al. 1995; Chatzizisis et al. 2011; Koskinas et al. 2013a); advanced plaques which have an increased tendency to rupture and cause an ACS.

Although disturbed ESS can trigger a series of pathological responses from the ECs, it is unable to threaten plaque integrity directly. Blood pressure-derived forces develop internally (plaque structural stress) within the arterial wall and are five orders of magnitude greater than ESS. In advanced plaque rupture the continuity of the fibrous cap is disrupted which in turn unleashes the thrombogenic contents of the plaque into the blood stream. Histopathological evidence shows that the fibrous cap ruptures where is the thinnest and at where it meets with the fibrous intima. In vulnerable plaques, plaque structural stress may act in concert with ESS to trigger TCFA rupture (Pedrigi et al. 2014). Early biomechanical models of coronary plaque have shown that those locations are locations of increased plaque structural stress (Richardson, Davies, and Born 1989; Cheng et al. 1993b). Due to the complexity of the geometry, numerical approaches are being utilised to estimate the forces that act on the plaque and are conducive to plaque rupture.

The life-threatening and asymptomatic nature of coronary artery disease creates a challenge for patient risk management. In most cases thrombosis is caused by plaque rupture. While standard clinical imaging modalities such as X-Ray Angiography, OCT and NIRS-IVUS can provide a morphological evaluation of coronary lesions to guide coronary revascularization procedures, their potential in predicting the occurrence of an ACS on the basis of advanced plaque morphology alone is low for clinical relevance

and more tools are warranted for that reason. Biomechanical modelling is a promising tool to assess biomechanical factors contributing to plaque rupture but currently they face limitations which do not allow translation to the clinic

1.3. Conclusions

Myocardial infarction is a leading cause of death. No therapeutic strategies have been developed specifically to prevent plaque rupture instead most therapies for myocardial infarction are directed at the events that follow acute plaque rupture by thrombolysis. It is well recognised that fatal coronary thrombi are predominantly caused by atherosclerotic plaque rupture; they constitute 60-75% of total sudden cardiac death cases. Clinical management of acute cases has been difficult due to the lack of warning symptoms in patients presenting with an ACS. While identification of imaging precursors of high-risk plaques has improved, they offer at present a rather limited positive predictive value. Analysis of the biomechanical environment of coronary lesions can be an additional tool for risk stratification if more physiologically relevant approaches are followed.

2. Pathology of advanced coronary plaques

2.1. The coronary vasculature

2.1.1. Anatomy and physiology

The coronary arteries are muscular arteries supplying the myocardium with blood, oxygen, and essential nutrients (**Figure 3**). They can be sub-divided into three categories, epicardial, transmural and perfusing. Epicardial vessels (arteries and veins), such as the left anterior descending (LAD), the left circumflex artery (LCx) and the right coronary artery (RCA) act as conduit vessels. They run over the periphery of the heart inside the pericardial cavity in a buffering and lubricating layer of adipose tissue. They constitute the major source of coronary compliance. Transmural vessels branch perpendicular to the epicardial vessels across the layers of the myocardium and perfusing vessels (arterioles and venules) regulate coronary resistance to flow and facilitate oxygen and nutrient transport by increasing the arterial cross-sectional area.

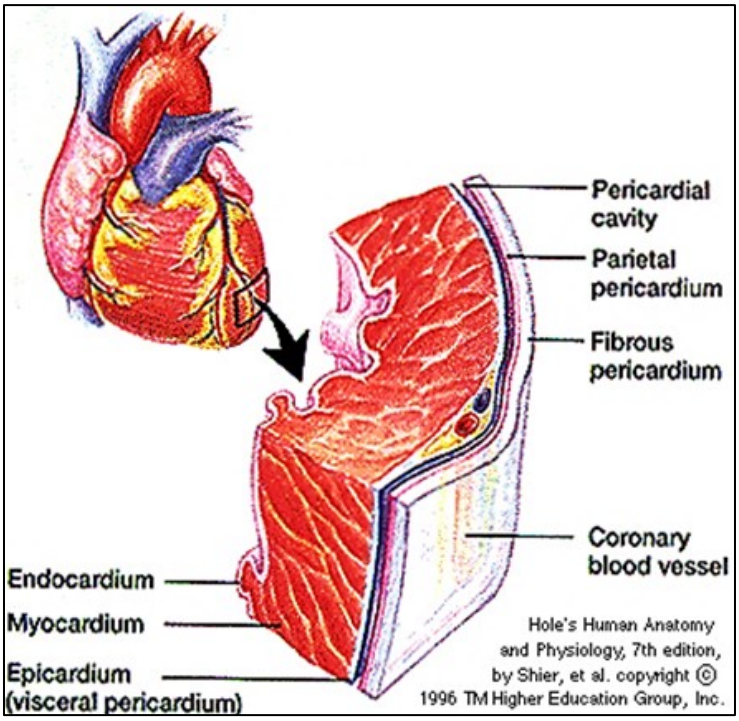

Figure 3 The layers of the heart. Some layers are active such as the myocardium while others are passive, such as the endocardium epicardium and pericardium. The epicardial coronary vessels run around the periphery of the heart in a casing of adipose tissue and sealed with the fibrous pericardium. Figure reproduced from Shier, Butler and Lewis (1996).

Unlike other conduit arteries, their perfusion takes place in diastole (Marques et al. 2002) when the heart muscle relaxes (ventricular relaxation). During the ejection phase, the myocardium contracts causing the perfusing arteries to collapse, thereby increasing dramatically distal coronary flow resistance. The positive pressure gradient further augments the size of re-circulation zones in the inner side of curvatures and branch ostia. Disturbed flow is known to predispose the endothelium to pro-inflammatory, pro-atherogenic phenotype at the presence of high LDL levels in the blood plasma rendering those locations predilection sites for development of coronary artery disease.

2.1.2. Composition & structure of the coronary arteries

The intima is the innermost layer of coronary arteries and consists of an endothelial cell lining and the sub-endothelial layer. ECs attach themselves to the internal elastic lamina via cell-membrane junctions. The functional role of the endothelium is predominantly mechanosensory leaving the media to carry the load bearing function of the arterial wall in physiological conditions. This is not to say that the intima is devoid of structure and is not of mechanical significance. For example, the coronary intima is rich in collagen, primarily types I and III (Shekhonin et al. 1987) and as the fibroproliferative process of coronary atherosclerosis advances with time, the diseased intima contributes considerably to the vessel mechanical properties as it has been shown in studies subjecting layer-specific mechanical properties of coronary arteries (Holzapfel et al. 2005) to tensile testing. Elastin is present as well organised endowing it with sufficient compliance.

The coronary media is the middle layer can be considered as a composite structure with active (cellular) and passive (extracellular matrix) components. The active part consists of smooth muscle cells (SMCs) whose contractile function regulates vascular tone but also adds to the total stiffness, particularly *in vivo* (Chen and Kassab 2017). The extracellular matrix is rich in protein fibres, namely collagen and elastin in a fluid-like matrix rich in proteoglycans and glycosaminoglycans (GAGs). This fibrous scaffold distributes the mechanical signals from blood flow and pressure to vascular cells. From a structural point of view SMCs are aligned along the circumferential direction with a small helical angle towards the axial direction (Zoumi et al. 2004). The

extracellular matrix is rich in elastin and collagen, with a collagen to elastin ratio of 3.74 and collagen content of approximately 20% (Chen et al., 2011a). Collagen appears to be intertwined with elastin as it is can be observed from label-free multiphoton imaging of healthy coronary arteries (Zoumi et al. 2004) (**Figure 4**). Arterial media is known for its highly organised lamellar structure in which elastin forms concentric radial layers of elastin sheets (Clark and Glagov 1985; O'Connell et al. 2008). Nevertheless, this lamellar structure appears to be less pronounced towards the periphery (Gasser, Ogden, and Holzapfel 2006), muscular arteries (e.g. coronaries) as opposed to conduit/elastic arteries (e.g. aorta).

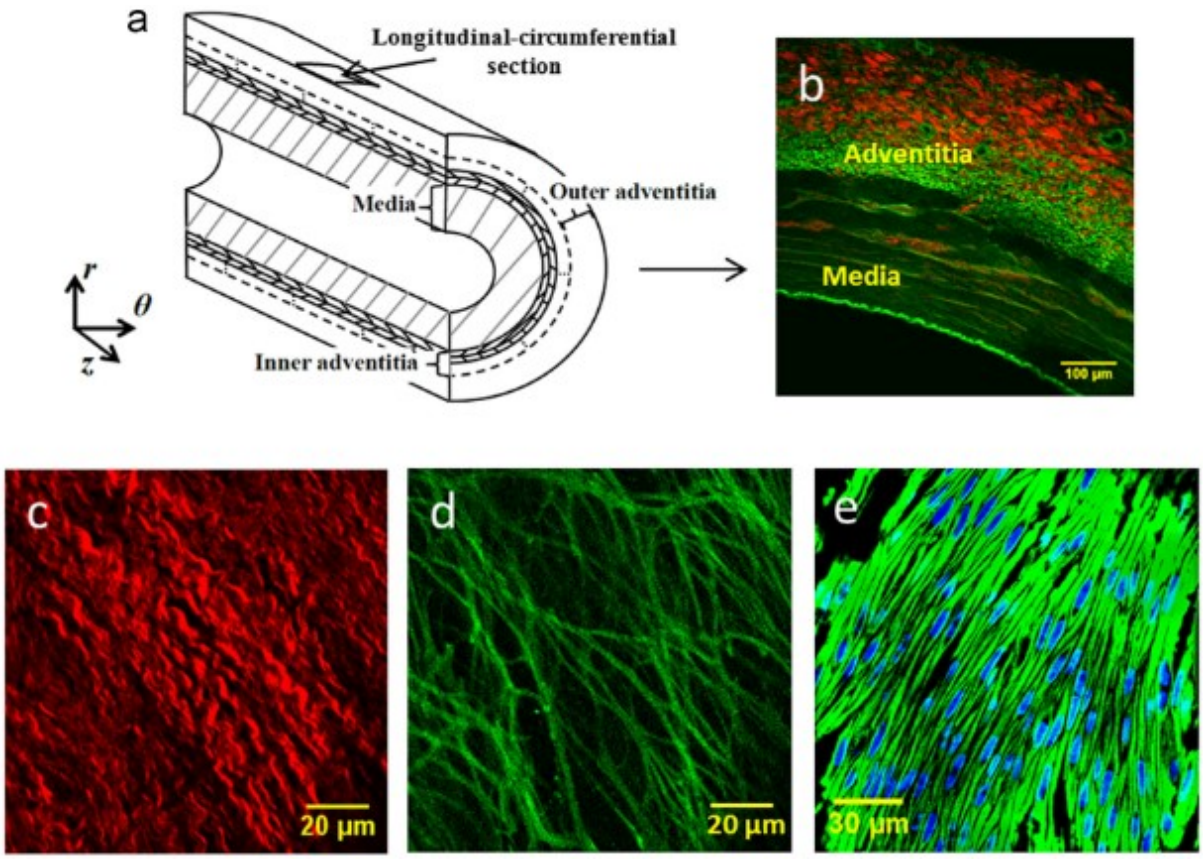

Figure 4 Label-free, second harmonic generation (SHG) imaging and two-photon excitation fluorescence (TPEF) microscopy of healthy porcine coronary arteries. (a) Schematic of the arterial wall. (b) Combined SHG and TPEF image of radial-circumferential plane of arterial wall: collagen (red) and elastin (green). (c) Longitudinal-circumferential section of collagen and elastin in adventitia, (d) confocal image SMCs in media stained for F-actin (green) and nucleus (blue). Figure reproduced from Chen and Kassab (2016).

Collagen fibres have a hierarchical structure that spans across multiple scales; from nano to microscale determining the mechanical properties of the arterial wall from the macroscale to the microscale (Fratzl 2008). Crosslinked tropocollagen molecules

comprise collagen microfibrils, fibrils, and fibres. The adventitia is mainly composed of undulated collagen fibres which are progressively recruited as blood pressure rises beyond physiological levels.

2.2. Atherogenesis

The reader is encouraged to consult citing literature for more detailed description of the pathobiological mechanisms. Herein, only the aspects which can affect arterial mechanics will be highlighted.

Elevated blood LDL levels are essential to initiate the cascade of pathological processes that render ECs dysfunctional. Direction of flow is very important for normal vessel function. While forward laminar flow promotes vascular health by upregulating anti-inflammatory, anti-thrombotic molecules, disturbed flow, native to inner side of curvatures and branch ostia gradually impairs endothelial function by upregulating pro-inflammatory, pro-thrombotic and vasocontricting pathways that puts it into an "activated" state.

Disturbed flow impairs production of nitric oxide (NO) by downregulating the gene expression of endothelial nitric oxide synthase (Gambillara et al. 2006; Cheng et al. 2005) (eNOs). Disturbed flow conditions play a central role in increasing the permeability of the intima by loosening of cellular junctions, impairing the regenerative process triggering apoptosis (Davies 2009b). As ECs are very sensitive to flow direction they transform from a fusiform, ellipsoidal (long axis direction of the flow), compact shape to a polygon shape which is believed to widen cell-cell junctions (Chiu and Chien 2011; Davies 2009b) thereby facilitating LDL transport through a defective endothelial barrier.

Recirculation zones increase the time LDL cholesterol stagnates which facilitate the trespassing of LDL cholesterol in the subendothelial space through a "porous" intima. LDL cholesterol is chemically modified with a resident surplus of oxidative enzymes such as nicotinamide adenine dinucleotide phosphate (NADPH) oxidase (Hwang et al. 2003) and xanthine oxidase (McNally et al. 2003). The ECs express adhesion molecules either on abluminal surface, mainly vascular cell adhesion

molecule-1 (VCAM-1), intracellular adhesion molecule-1 (ICAM-1), E-selectin and P-selectin (Hansson 2005) which contribute to recruitment of blood-borne immune cells to the region. Upon infiltration, the monocytes differentiate into macrophages and internalise the oxidised lipoproteins, a process known as phagocytosis. It has been demonstrated that oxidised LDL cholesterol along with the overexpression of monocyte chemoattractant protein-1 (MCP-1) by macrophages are powerful stimulants of the immune response (Libby 2012).

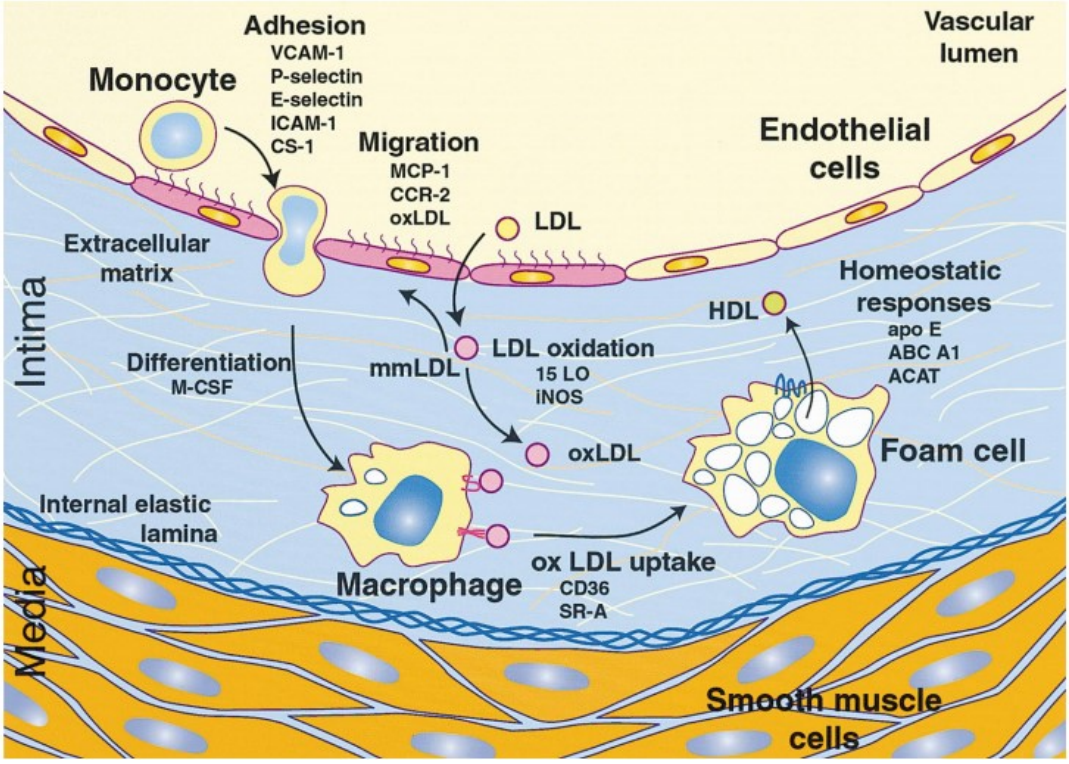

Figure 5 Biochemical events in the development of an early lesion. Figure reproduced from Glass and Witztum (2001).

As a result of above pro-atherogenic processes (**Figure 5**) the arterial intima thickens due to VSMC transmigration, proliferation and synthesis of a matrix rich in collagen and proteoglycans (Palumbo et al. 2002). Intimal VSMCs have a different phenotype to medial VSMCs and they do not possess contractile properties. Instead they are mainly involved in synthesis of ECM (Schwartz, Virmani, and Rosenfeld 2000). Adaptive intimal thickenings can progress to xanthomata or "fatty streaks" should the pro-atherogenic stimuli persist. Foam cells (i.e. macrophage cells that have internalised

oxidised LDL) can be observed through the microscope to populate the sub-endothelial space.

Table 1 Classification of coronary lesions based on morphological features based on the Virmani scheme. Reproduced from Virmani et al. (2000).

	Description	Thrombosis
Nonatherosclerotic intimal lesions		
Intimal thickening	The normal accumulation of smooth muscle cells (SMCs) in the intima in the absence of lipid or macrophage foam cells	Absent
Intimal xanthoma, or "fatty streak"	Luminal accumulation of foam cells without a necrotic core or fibrous cap. Based on animal and human data, such lesions usually regress.	Absent
Progressive atherosclerotic lesions		
Pathological intimal thickening	SMCs in a proteoglycan-rich matrix with areas of extracellular lipid accumulation without necrosis	Absent
Erosion	Luminal thrombosis; plaque same as above	Thrombus mostly mural and infrequently occlusive
Fibrous cap atheroma	Well-formed necrotic core with an overlying fibrous cap	Absent
Erosion	Luminal thrombosis; plaque same as above; no communication of thrombus with necrotic core	Thrombus mostly mural and infrequently occlusive
Thin fibrous cap atheroma	A thin fibrous cap infiltrated by macrophages and lymphocytes with rare SMCs and an underlying necrotic core	Absent; may contain intraplaque hemorrhage/fibrin
Plaque rupture	Fibroatheroma with cap disruption; luminal thrombus communicates with the underlying necrotic core	Thrombus usually occlusive
Calcified nodule	Eruptive nodular calcification with underlying fibrocalcific plaque	Thrombus usually nonocclusive
Fibrocalcific plaque	Collagen-rich plaque with significant stenosis usually contains large areas of calcification with few inflammatory cells; a necrotic core may be present	Absent

2.3. Advanced atherosclerotic plaques

Early lesions can either remain quiescent or progress to advanced lesions should pro-atherogenic stimuli persist. At this stage, the intima further enlarges and the total lipid content within the intima resides in both intracellular (as in foam cells) and extracellular form, as in cholesteryl ester-rich, lipid pools. In Pathological Intimal Thickening, extracellular lipids are dispersed within the intima but there is no sign of necrosis or cellular debris. Although this phenotype is termed as an advanced lesion in the Virmani scheme (**Table 1**), there are cases in which is considered as a predecessor to more advanced lesions thus it is a loosely defined morphology. This ranking may stem from the concept that more advanced plaques are prone to develop acute events. Interestingly, it was found to precipitate many plaque erosion cases (Virmani et al. 2000) mainly because of the high proteoglycan and GAG content of the matrix where SMCs reside. The pathology is poorly understood and may shed light to mechanisms leading to plaque erosion and subsequent thrombosis.

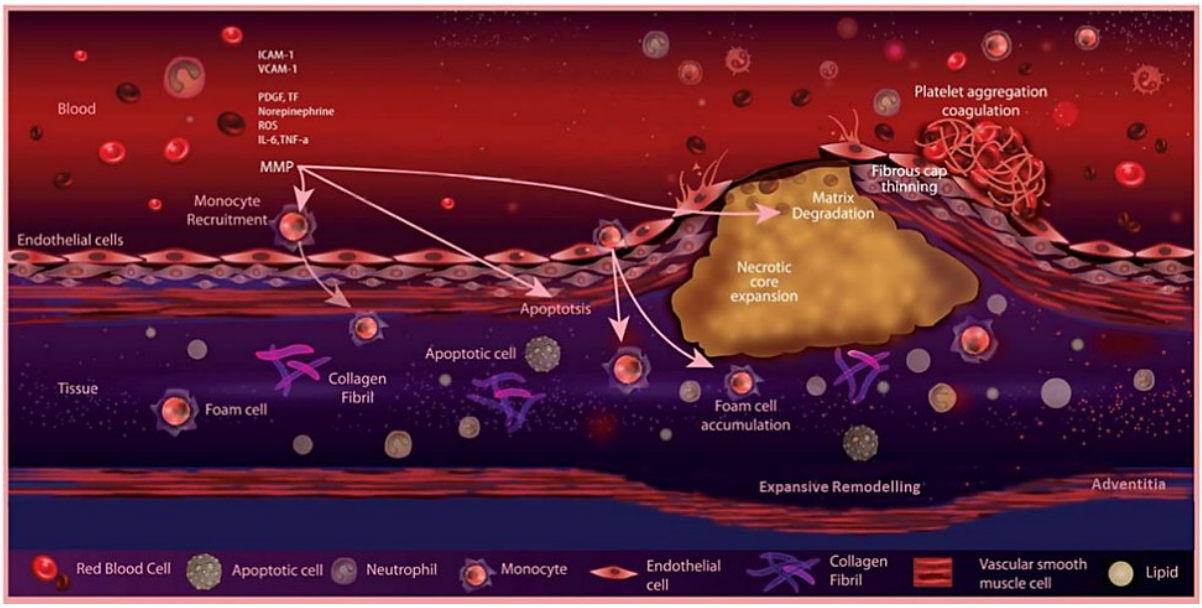

Figure 6 A schematic illustration of some of the processes that are involved in plaque development and rupture. Image reproduced from Gijsen et al. (2019).

In fibrous cap atheroma (**Figure 6**), all dispersed lipid accumulations often merge to one confluent necrotic core (NC) which is very soft (Loree et al. 1992; Loree et al. 1994) and rich in cholesterol and its esters, specifically cholesteryl esters, phospholipids (predominantly cholesterol linoleate), and triglycerides (Bentzon et al. 2014), and dead cells close to the luminal side borders of necrotic core and fibrous tissue, without any underlying supporting matrix. Cholesterol clefts are thought as an advanced characteristic. It is noteworthy that the extracellular lipids aggregates differ chemically from intracellular ones within macrophage foam cells. Ineffective removal of dead immune cells (efferocytosis) within the plaque can contribute to further expansion of the necrotic core (Finn et al. 2010). Fibrillar collagen types I, III and IV (Shekhonin et al. 1987; Ooshima and Muragaki 1990; Murata, Motayama, and Kotake 1986) and proteoglycans main constituents of fibrous cap, whereas the number of SMCs is small. Although the cap is inflamed with macrophages, the total inflammatory burden of the lesion is very low (Virmani et al. 2006). A major determinant of lesion stability is the thickness of the overlying cap (**Figure 7**). Macrophages can secrete proteolytic enzymes, such as MMPs that degrade local fibrous matrix leading to progressive thinning of the fibrous cap (Libby 2012). Intraplaque haemorrhage is a common feature of advanced plaques occurs when neo-vessels originating from the adventitia insudate red blood cells, immune cells and platelets in the plaque increasing its thrombogenicity (Falk et

al. 2013a). Collagen consists of 60% of all plaque protein determining plaque's structural stability. Human atherosclerotic plaques contain collagen types I and III, with III being 2/3 of total collagen. Type IV collagen has been observed in fibrous caps (Shekhonin et al. 1987). Apart from the obvious role in separating thrombogenic necrotic core from circulating blood flow, it is associated with many other biological processes as well (Rekhter 1999).

Fibrocalcific plaques are another advanced plaque phenotype which can be identified with intravascular imaging. Spotty calcifications can be seen in the fibrous cap with OCT or deeper inside the plaque at the interface of NC and fibrous intima with IVUS. Because of the disparate mechanical properties of calcium clusters and necrotic core or fibrous neo-intima they lead to local stress concentrations and increase the vulnerability to rupture, according to mechanical analyses (Maldonado et al. 2012). While nodular calcifications protruding into the lumen are relatively rare, they sometimes precipitate thrombosis (Virmani et al. 2006; Tomaniak et al. 2020). Thrombus formation in the absence of fibrous cap disruption falls into the category of plaque erosion.

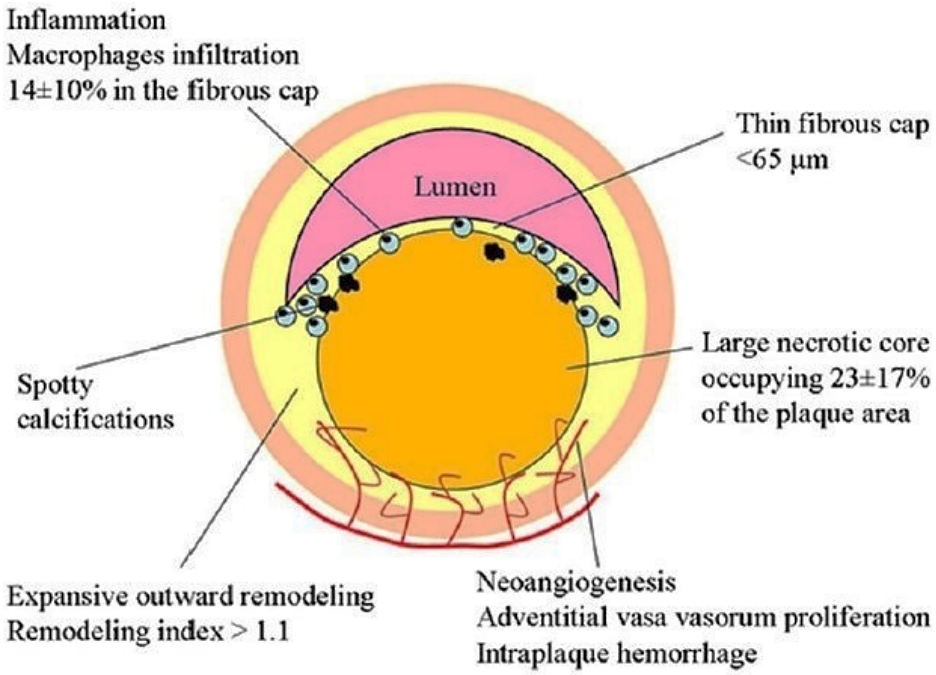

Figure 7 Morphological features of rupture-prone plaques based on histological examination. Figure reproduced from Vancraeynest et al. (2011).

2.4. Animal models of atherosclerosis by surgical flow manipulation

Spontaneous atherosclerotic plaque formation in humans takes many years and is a result of a complex interaction of the environmental risk factors for each individual. Clinical tracking of the disease is difficult due to lack of premonitory symptoms. Tissue from humans is difficult to harvest for studying the mechanisms involved in advanced plaque formation. All the above reasons provided a basis for the development of animal models.

The persistence of the disease to manifest focally at specific arterial sites associated with disturbed laminar flow inspired an emulation of this flow profile as in healthy arteries as an atherogenic stimulus. Imposing persistent flow disturbances in animals has proven adequate to impair the endothelial physiology by "activating" it towards a pro-inflammatory and pro-atherogenic phenotype as outlined in previous sections. Mice, rabbit, pigs, swine, primates have been used. In those models flow manipulation is done either surgically (e.g. arteriovenous fistula, arterial ligation) or by using flow-modifying devices, such as vascular grafts, peri or intravascular devices (Winkel et al. 2015).

Mouse models are convenient to use due to their low cost of purchase, breeding and maintenance and their amenability to genetic modifications. While they have provided immense insight on molecular mechanisms of atherosclerosis, there are clear limited when used for studying inflammatory processes of the disease (Seok et al. 2013) therefore highlighting the necessity for new large animal models that better emulate human pathology. Larger animal models have been regarded as more representative of the human disease (Getz and Reardon 2012; Rezvan, Sur, and Jo 2015).

Porcine models

The anatomy and physiology of the porcine cardiovascular system bears great resemblance to that of humans (Hearse & Sutherland 2000) which enables percutaneous coronary interventions and use of intracoronary imaging modalities which can be readily translated to patients. An important advantage of porcine models is that plaques have more human-like characteristics (**Figure 8**, second column). However, it is a much slower model which needs higher husbandry costs. The recent discovery of new

cholesterol-lowering drugs for patients - of the class of proprotein convertase subtilisin kexin type 9 (PCSK9) - paved the way for further reduction of the time for advanced plaques to develop in porcine models (Getz and Reardon 2012).

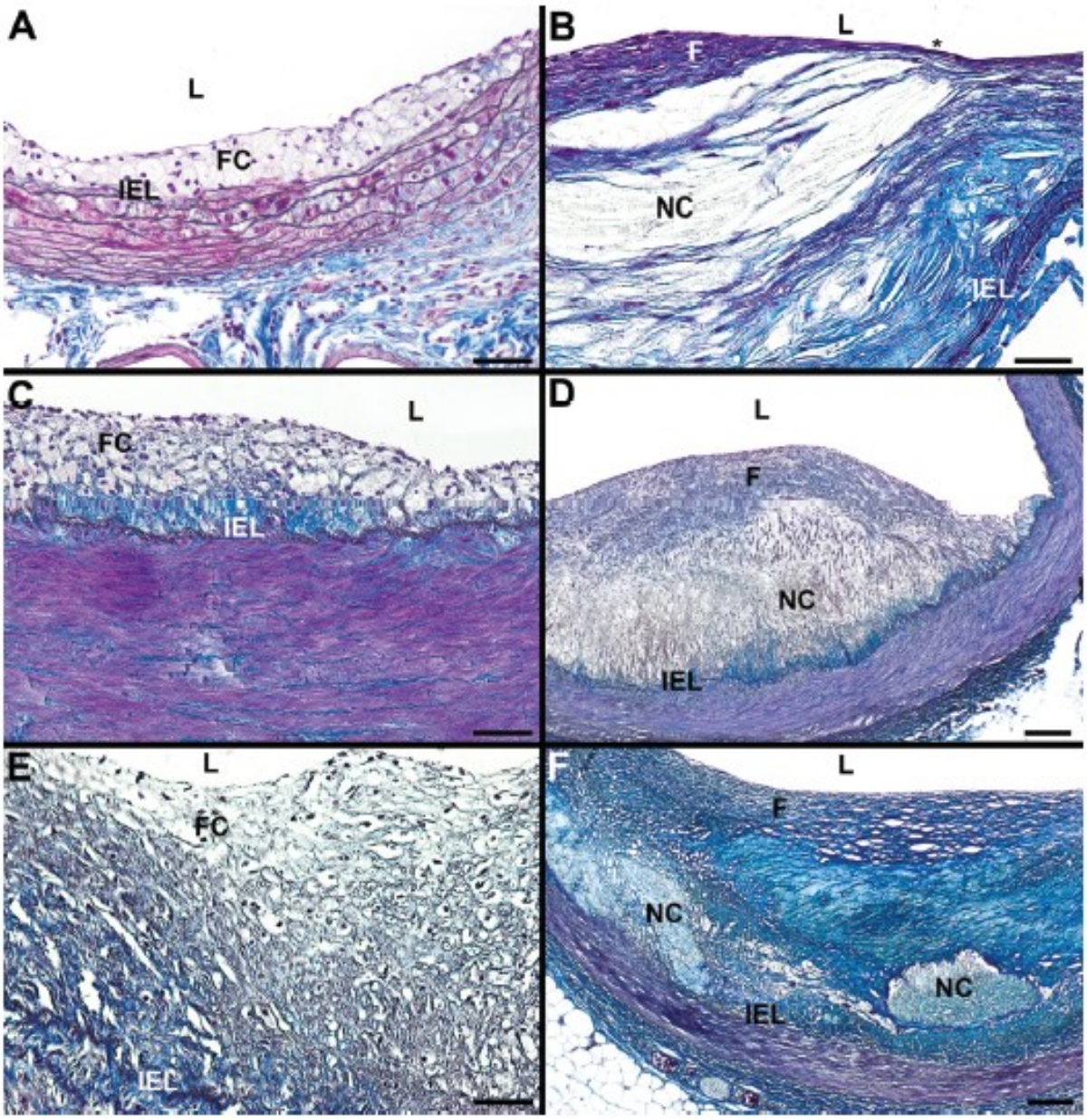

Figure 8 Comparative histology of murine (first column; A, C, E) and porcine (second column; B, D,F) atherosclerotic plaques. Advanced porcine lesions include necrotic core (NC) formation, overlying of necrotic core with fibrous cap (FC), deposition of abundant fibrous tissue (F). L: lumen, IEL:internal elastic lamina. Scale bars: 50 μm for A–C, E, 200 μm for D & F. Elastin–trichrome stain (nuclei, dark purple; cytoplasm, purple; collagen-rich matrix, blue; elastin, black). Reproduced from Shim et al. (2016).

By combining a mutation of the PCSK9 gene (attenuating cholesterol metabolism), flow disturbances by implantation of a shear modifying, stenotic stent and

a high calorie high cholesterol diet, formation of advanced plaques was accelerated in Yucatan minipigs (Pedrigi et al. 2014). The shear modifying (or stenotic) stent was designed to impose a complex disturbed flow profile within coronary arteries. OCT was used to assess lesion progression ant regular timepoints until the termination point of the *in vivo* experiment. The flow field in stented and non-stented coronaries was calculated using computational fluid dynamics (CFD) software. Coronary plaques were assessed at 34 weeks post-stent implantation, showing an almost 3-fold increase in plaque burden in the areas exposed to low and multidirectional ESS compared to non-stented control coronary. Plaques with thin cap fibroatheroma characteristics were observed in the region downstream shear modifying stent location (**Figure 9**). Such combination approaches may prove to be useful in other animal models as well and studies using various combination approaches are ongoing.

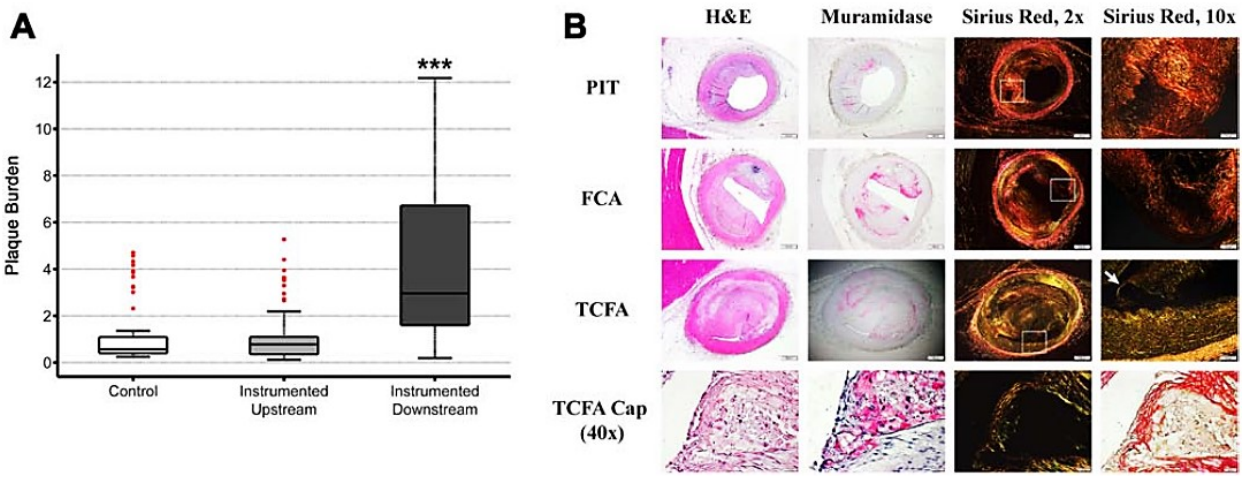

Figure 9 Causal relationship between instrumentation and plaque formation. (A) Plaque burden was approximately three-fold higher downstream of shear modifying stent in comparison with upstream section and unstented control vessel. (***P<0.001). Red dots correspond to outliers. (B) Sample histological sections of advanced plaque types from the vessel segment downstream of the shear modifying stent. Advanced lesions were identified based on the presence of a necrotic core, inflammation burden, and the presence of a fibrous cap. FCA: fibrous cap atheroma; PIT: pathological intimal thickening; TCFA: thin cap fibroatheroma. Image reproduced from Pedrigi et al. (2015).

It is useful to consider that many animal models in different species develop different lesion characteristics and thus each model comes with particular strengths and weaknesses (**Table 2**). It is important to have an understanding of those characteristics in order to be able to interpret the results as accurately as possible. To this date, there is no animal model that can perfectly mimic the pathobiology of the human disease.

Animal models offer a time-effective alternative to the human disease and highlight a particular aspect of the pathophysiology. In other words, validity of use boils down to the specific research hypothesis studied.

Table 2 Features of novel, genetically modified, animal models of atherosclerosis. Reproduced from Rezvan, Sur, and Jo (2015).

Reference	Bjoerklund [25]	Roche-Molina [26]	Pedrigi [47]
Animal(s)	Mouse, C57BL/6NTac Hamster, Golden Syrian	Mouse, C57Bl/6J	Minipig
Diet modification	High Fat Diet	High Fat Diet	High Fat Diet
Surgical intervention	N/A	N/A	Intracoronary shear modifying stent
PCSK9 mutation(s)	D377Y and D374Y	D374Y	D374Y
Dose(vector genomes per animal)	2.0×10^{10}, 1.0×10^{10}, 5.0×10^{11}	3.5×10^{10}	N/A
Age when dosed	8 weeks	30 days	N/A
Lesion development time post dose	12 weeks	84 days	34 weeks

2.5. Imaging of advanced plaques

Plaque imaging is crucial for early detection and assessment of high-risk lesions and culprit plaques, as atherosclerosis progresses silently until the final acute event. There are two modalities which have been most widely tested for their ability to identify high risk lesions and culprit plaques and are used to guide revascularisation procedures: IVUS, and OCT.

IVUS relies on the echogenicity or differences in the acoustic impedance of different parts of tissue. It has been widely used for the clinical assessment of coronary plaques and to guide coronary revascularisations (Maehara et al. 2009). Virtual histology – IVUS (VH-IVUS) is often used in conjunction with IVUS to provide a surrogate of *in vivo* plaque composition based on the echogenicity of different parts of the tissue (Brown et al. 2015). While some claim that IVUS is a reliable tool to provide a reasonable estimate *in vivo* plaque composition (Stone et al. 2011; Brugaletta et al. 2011) others doubt the ability of IVUS to detect even macro-features of plaques. In one example, when compared with histology, VH-IVUS has been found to mis-identify fibrous tissue areas with necrotic core, and in another example a fibroatheroma with large necrotic core was mislabelled as of fibrous tissue in a porcine model of coronary atherosclerosis (Thim et al. 2010). Moreover, IVUS (resolution: 150 μm – 200 μm) deters identification of rupture prone plaques, as defined by a necrotic core underlying a cap

thickness less than 65μm (Virmani et al. 2000). OCT has significantly finer resolution (15-20μm) than IVUS. The higher resolution comes at a cost as OCT cannot visualise plaque features located deep inside plaques due to back-scattering signal attenuation. Lipid-rich lesions have different optical properties than fibrous plaque tissue.

2.6. Conclusions

Despite the coronary vasculature being exposed to systemic risk factors, CAD tends to form at arterial locations associated with disturbed shear. *In vivo* animal models attempting to emulate such haemodynamic conditions naturally (such as in aorta) or with flow-altering devices have shown there is a causal relationship between disturbed flow and plaque formation and development. There is a field of interdisciplinary research in the field of coronary plaque biomechanics. The next section will present a brief review on the effect of biomechanics on vascular cell biology but also the effect of changing biology - in the course of plaque development - on biomechanics that makes biomechanics a promising tool.

3. Role of Biomechanics in the natural history coronary atherosclerosis

3.1. Mechanical forces in the arterial wall

3.1.1. Blood flow haemodynamics

At any time, the arterial wall experiences two external forces: a frictional force due to blood flow exerted on the endothelial layer (ESS) and blood pressure. Internal forces develop within the arterial wall in order to sustain the external loads (Figure 3). The composition and structure of the arterial wall determines the levels of structural stress within the arterial wall. It is known that the arterial wall has a layered structure. ESS is sensed by a lining of ECs which adhere to the internal elastic lamina. The extracellular matrix primarily bears the load from blood pressure. The arterial wall has the ability to adapt to changes in those forces due to external stimuli; this process is called arterial remodelling. Hypertension is a distinctive example where the increased

load results in expansive remodelling and thickening of the vessel wall to reduce circumferential stress.

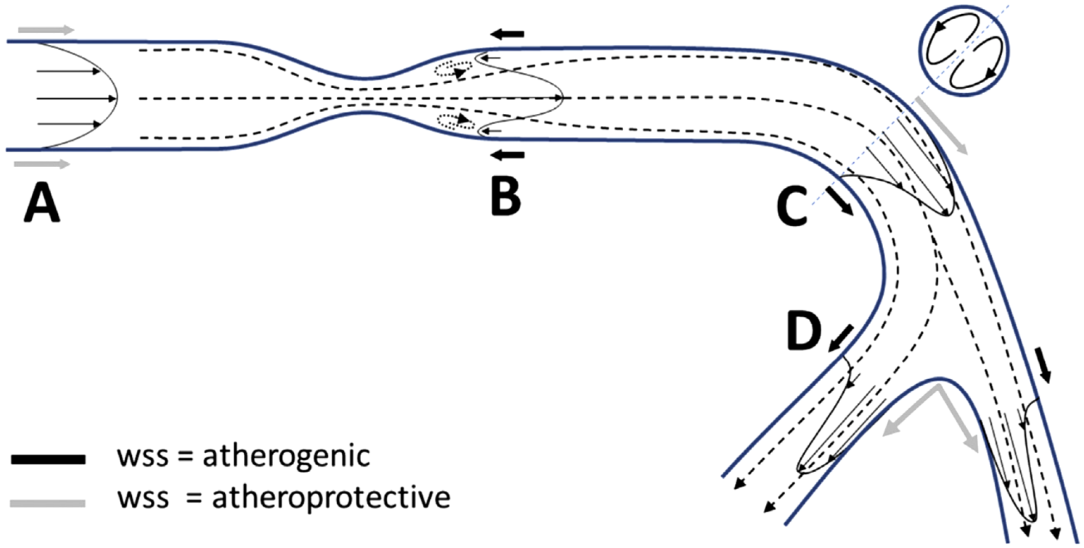

Figure 10 Different laminar flow profiles. (A) Poiseuille parabolic flow in a straight segment, (B) flow separation and recirculation downstream a stenosis, (C) flow along a curved segment. Secondary flow crosswise main direction of flow. Large shear gradients in the outer curvature than inner curvature that is prone to separation. (D) flow profile distal branch ostium and regions of high and low shear. Shear is determined by the local velocity gradient and the local viscosity. There is a temporal aspect to these profiles which here is simplified by taking steady flow. Figure reproduced from Winkel et al. (2015).

Flow inside arteries is typically laminar with Reynolds number below < 200. Secondary flow in curved segments is directed from the centre outward (**Figure 10**). This flow regime is still laminar and turbulent flow is rare. Some cases include severe aortic valve stenosis and the aortic arch. However, some arterial sites flow acceleration close to the aorta and branching points can lead to flow separation, recirculation and re-attachment. In these locations flow is still laminar however there are spatial and temporal gradients in the magnitude and direction of the ESS. Such locations appear in the initial part of the aortic tree; as the diameter tapers and flow rate decreases, proportion of viscosity forces increase to acceleration forces leading to parabolic flow profiles. ESS triggers a range of mechanobiological pathways as outlined in the next section. However, ESS is of insufficient magnitude to alter the integrity of the vascular wall directly.

Flow in the coronary arteries is quite distinct from other locations of the arterial tree. Unlike other conduit arteries, their perfusion takes place in diastole (Marques et

al. 2002) when the heart muscle relaxes (ventricular relaxation). During ventricular ejection (systole) the myocardium contracts causing the perfusing arteries to collapse, thereby increasing dramatically distal coronary flow resistance thereby reducing coronary flow. The flow waveform is out of phase with the pressure waveform (**Figure 11**). The positive pressure gradient and the high tortuosity and branching of the coronary arteries further augments the size of re-circulation zones in the inner side of curvatures and branch ostia. The movement of the heart muscle during ventricular ejection causes the coronary arteries to translate and bend which has the potential to affect the flow field (Ding, Zhu, and Friedman 2002). In clinical practice, the vessel motion is also regarded to be vessel-specific.

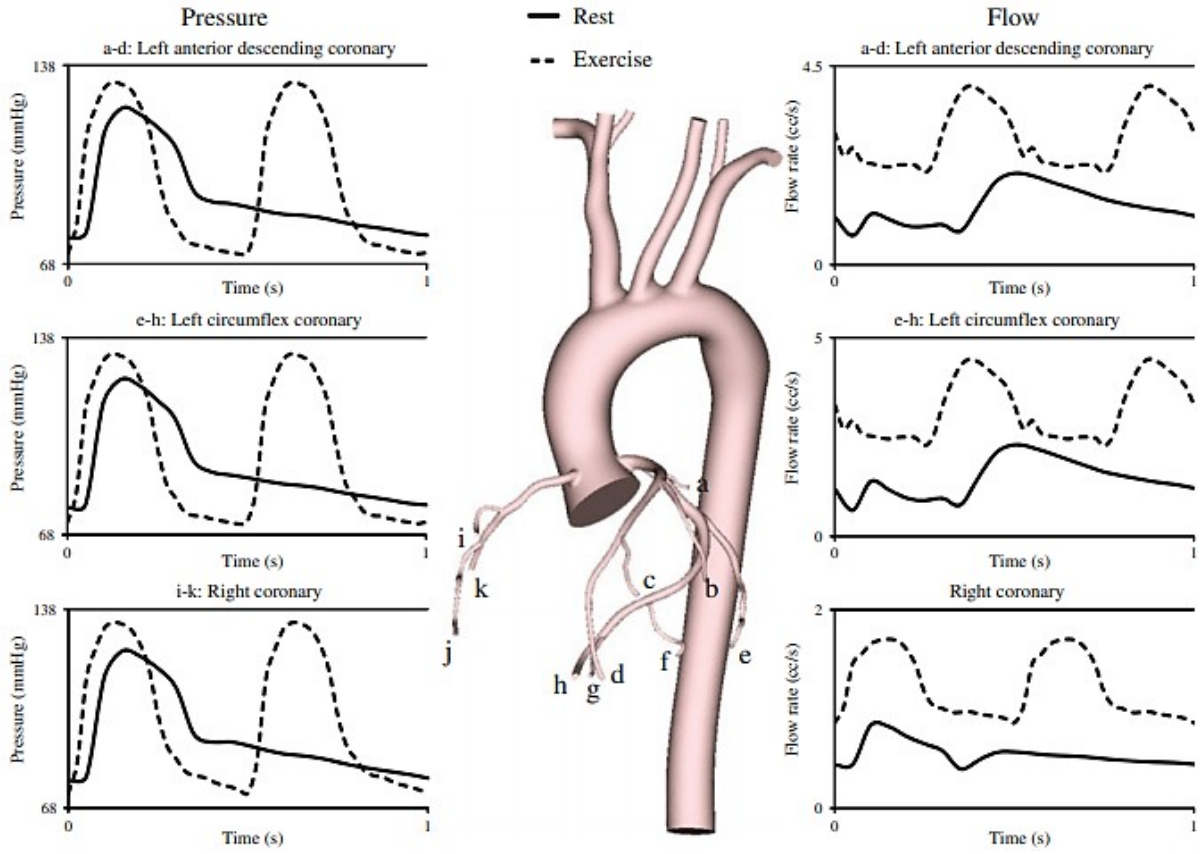

Figure 11 Pressure and flow waveforms of coronary arteries (left anterior descending - LAD, left circumflex – LCx, and right coronary artery - RCA) during rest and light exercise. Figure reproduced from (Kim et al. 2010)

3.1.2. Vessel wall mechanics

Stress and strain in healthy arteries are considered fairly uniform (**Figure 12**). According to Laplace's law, under the approximation of a vessel segment to an

assumption of a thin wall cylinder, the circumferential stress within the arterial wall is proportional to the radius and disproportional to the vessel thickness. In the absence of pressure, the vessel wall is still in a stressed state; tethering of the arteries along their longitudinal direction gives rise to axial stretch while transmural cut relieves residual stresses which are supposed to homogenise the radial distribution of circumferential stress (Chuong and Fung 1986; Cardamone et al. 2009). Residual stresses are internal stresses that exist even when the vessel is unloaded (no blood pressure). One way to obtain an estimate of residual stresses is to make a longitudinal incision along an arterial segment which will make the arterial wall to open up and relieve those stresses. It is now well established that residual stresses put inner wall under compression whereas the external side under tension. It has been demonstrated that the intima, media and adventitia experience different degrees of residual stress (Holzapfel and Ogden 2010). It is believed that residual stresses homogenise the stress distribution across the arterial wall of healthy vessels therefore it is considered an important inclusion for computational models. Residual stress changes with the location along the arterial tree, age and most likely with atherosclerosis progression. It is less clear though whether it retains the same properties with disease and inclusion is more difficult due to the difficulties in estimating the zero-stress state of vessels within plaque.

Computational methods have become increasingly popular in the last 20 years. Currently computation of mechanical forces in blood vessels is conducted by numerical techniques such as CFD, finite element modelling (tissue mechanics) and more recently coupled approaches such as fluid-structure interaction (FSI) modelling are used. Each of those methods are subject to assumptions. For example, CFD analyses assume a rigid vascular wall when solving the Navier-Stokes equations for computation of the flow velocity field along lumen geometries. In contrast, finite element modelling (FEM), does not account for the moving aspect of blood flow and is more suitable for simulating vessel mechanics. Their accuracy depends largely on the accuracy of the vessel geometry reconstruction, application of appropriate boundary conditions and material properties (for stress/strain analysis). Because FSI approaches merge CFD and FEM methodologies they are subject to fewer assumptions rendering them a more physiologically relevant tool to simulate the biomechanical response of arteries to flow and pressure. However,

due to the fact that FSI modelling is still computationally demanding, FE modelling can be a useful segway to FSI.

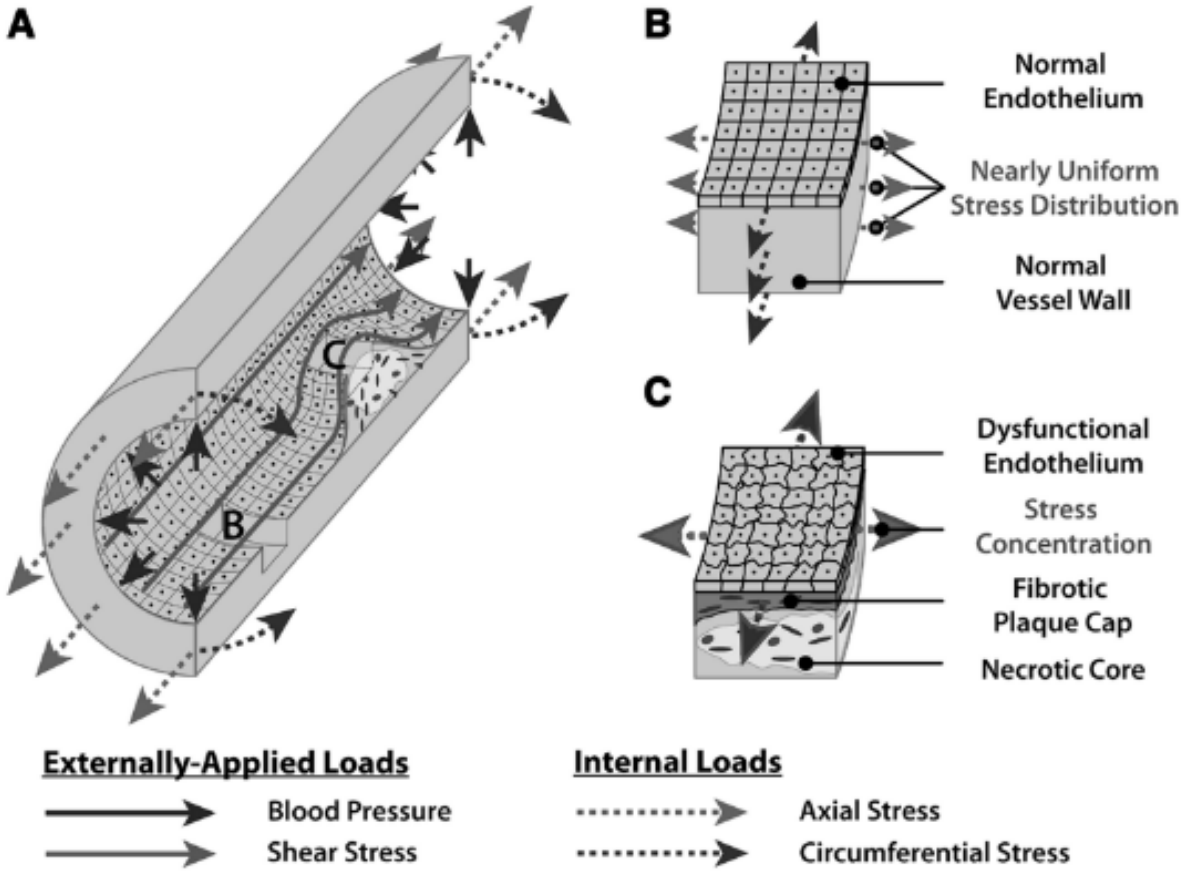

Figure 12 Schematic of the biomechanical forces acting on a blood vessel in normalcy and advanced plaques. (A) Blood pressure and ESS are externally applied (solid lines) and these result in internal loads i.e. axial stress and circumferential stress (dashed lines). (B) Forces on the normal vessel wall. (C) Schematic of a segment of the diseased wall with a fibroatheroma and resulting stress concentration. Figure reproduced from Pedrigi et al. (2014).

In the following chapters a brief review on the pathological effect of disturbed mechanics (shear and stretch) to the physiology of vascular cells (Section 3.2). The second subchapter (Section 3.3) will go through historical evolution of mechanics-mediated theories for atherosclerosis formation development and insight gained from in patient-specific, in vivo studies. We will conclude (Section 3.4) by highlighting limitations and gaps of knowledge.

3.2. Effect of disturbed biomechanics on vascular cells

3.2.1. Shear and stretch-mediated pathobiology of ECs

ECs possess a variety of mechanical receptors such as transmembrane ion channels, proteins and adhesion molecules, intercellular junction proteins, primary cilia, integrins, glycocalyx, as well as the cytoskeleton (Chien 2007). The mechanobiology of ECs in response to disturbed flow has been a subject of extensive *in vitro* investigation and exhaustive reviews (Davies 2009; Chiu and Chien 2011; Chatzizisis et al. 2007). Herein, we will try to summarise the most important pathways leading to dysfunctional vascular cell phenotypes (ECs and SMCs) in the development of coronary atherosclerosis.

Disturbed flow impairs normal vasodilatory function of coronary arteries by downregulating production of nitric oxide (NO) via two known mechanisms. One is by downregulating gene expression of endothelial nitric oxide synthase (eNOS); an enzyme which catalyses production NO by ECs (Balligand, Feron, and Dessy 2009). The other mechanism, which takes place at a pre-transcriptional level, involves reduction of the bioavailability of NO due to intracellular production of oxidative radicals, for example superoxide [O_2^-] or peroxynitrite [$ONOO^-$]) and nicotinamide adenine dinucleotide phosphate (NADPH) which intervene in the biochemical chain of NO production and reduce its resultant concentration (Hwang et al. 2003).

Impaired NO production can also increase stagnant flow in the vicinity of predilection sites by a progressively less dilating vessel wall. The alignment of ECs to shear is one of the most known characteristics of a healthy endothelium (Chien 2007). Disturbed flow can change the tightly packed arrangement of ECs from a fusiform to a polygonal shape increasing cellular gaps through which LDL can permeate because of its prolonged residence time in recirculation sites (Do et al. 2015). In addition, disturbed flow can even stimulate intracellular production of LDL by upregulation of sterol regulatory elements binding proteins (SREBPs) (Chiu and Chien 2011). All the above lead to subendothelial accumulation of LDL and its chemical modification by reacting with reactive oxygen species (ROS) is a powerful stimulant of the central immune response (Harrison et al. 2003).

It is long known that disturbed ESS impairs anti-coagulant processes of the endothelium by reducing the bioavailability of NO or downregulating gene expression of eNOs and prostacyclin (Chiu and Chien 2011; Chatzizisis et al. 2007). While high ESS was long known to be athero-protective (Pan 2009), supra-physiological ESS which can be native to stenotic lesions can damage the endothelium (He et al. 2016). However, it is not yet clear whether the damage of the endothelial layer is caused by high local structural stress (Groen et al. 2007) or the high ESS genuinely damages the endothelial layer. More research is warranted to elucidate the mechanisms leading to plaque erosion and whether local biomechanics could have a mediating role.

Activation of the nuclear factor kappa-light-chain-enhancer of activated B cells (NF-κB) pathway by disturbed flow and oxidised LDL is a key feature of the involvement of the innate immune system (Hishikawa et al. 1997). Several adhesion molecules, such as vascular cell adhesion molecule (VCAM)-1; intercellular adhesion molecule (ICAM)-1 and E-selectin are expressed in the abluminal surface of ECs and facilitate the retention of circulating immune cells (monocytes, T-lymphocytes, mast cells, eosinophils, dendritic cells) (Lehoux, Castier, and Tedgui 2006). Also, a series of other salient inflammatory molecules and chemokines are up-regulated by non-laminar flow such as tumor necrosis factor-α (TNF-α), interleukin-1 (IL-1) and interferon-γ (IFN-γ) and monocyte chemoattractant protein-1 (MCP-1) by monocytes (Libby 2012). In advanced stages of the disease, the immune system can participate actively in the biomechanical stability of plaques as foam cells were found to secrete MMPs which lyse fibrous tissue and promote progressive thinning of fibrous cap and destabilisation (Wang et al. 2003). Effect of mechanical environment on immune cells is not known.

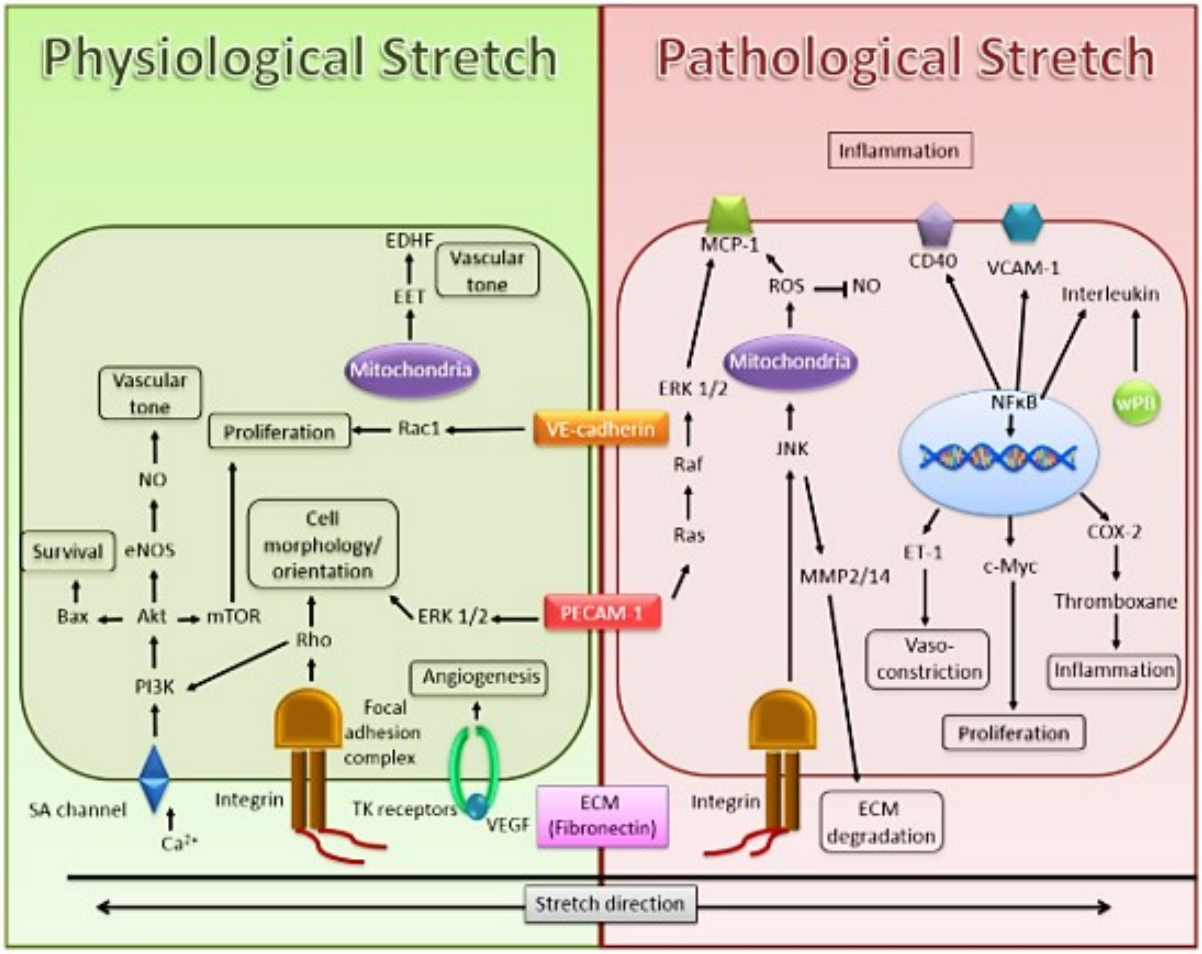

Figure 13 Stretch-activated signalling pathways in ECs contributing to a healthy and dysfunctional endothelium. Image reproduced from Jufri et al. (2015).

Disturbed stretch intensity is equally potent to trigger pro-atherogenic pathways (Jufri et al. 2015), at least shown *in vitro* (**Figure 13**), potentially amplifying the pathological role of disturbed shear. ECs are attached to the internal elastic lamina and the membrane may be stretched to different intensities subject on the instantaneous thickness and composition of the vessel wall. While a normal vessel exposes the ECs to circumferential stretch and axial stretch, the axial variation of mechanical properties in the course of the disease may also give rise to variations in stretch intensities and altered direction of strain. The primary direction of stretch is 90° perpendicular to flow, SMCs are oriented in this direction with a small helical angle (Lehoux, Castier, and Tedgui 2006).

Reviewing the relevant literature, there is considerable dispersion in the stretch intensities ECs are exposed to. To exemplify, Demicheva, Hecker, and Korff (2008) subjected human umbilical vascular endothelial cells (HUVECs) to 15-20% stretch for six

hours and found 200% increase in MCP-1 production. Kobayashi et al. (2003), stretched HUVECs with a magnitude ten times larger than the previous study (125-150%) and found a threefold increase 3-fold in IL-6 at 90 minutes. Zhao et al. (2009) needed only a tiny fraction (0-10%) to trigger almost three-fold production of cyclooxygenase (COX-2) at 3 h. While it is valid that different molecules may need different chemical equilibrium times, it is also true that the stretch intensities used *in vitro* to trigger pathological responses may not represent the *in vivo* environment. The actual stretch magnitude should include the residual stretch, axial stretch due to tethering points and diastolic prestress of the vascular bed of choice. Discovery of the molecular pathways for disturbed stretch is certainly important but in order to reflect patho-physiological conditions they may have to be linked to physiological levels of stretch.

3.2.2 Effect of disturbed stretch on SMCs and interaction with ECs

It is likely that SMCs are also exposed to disturbed stretch in terms of magnitude and direction as the plaque progresses. At least two mechanisms may be responsible for this: One mechanism could be the reduced bioavailability of NO via reduced phosphorylation of eNOs which leads to impaired contractile function and lower magnitude of stretch than physiological (Takeda et al. 2006; Lu and Kassab 2011). Another mechanism may be the progressive axial and circumferential asymmetry of plaque which might lead to alterations in the direction of stretch. During the course of the disease SMCs seem to have a reparative role by transmigrating in the intima and start proliferating and deposition of ECM and collagen culminating in the development of fibrous cap (Schwartz, Virmani, and Rosenfeld 2000).

The majority of findings regarding SMC mechanotransduction come as a result of studying hypertension, where smooth muscle is exposed to elevated levels of stretch. The vascular wall remodels by thickening to accommodate the increased load. Similar to EC alignment to flow, smooth muscle aligns to the direction of stretch (Mantella, Quan, and Verma 2015). There is ample evidence to support a role for disturbed stretch in promoting production of ROS during intracellular oxidative processes (Ali et al. 2004; Goettsch et al. 2009), impaired contractile function by downregulation of focal adhesion kinase (FAK) phosphorylation (Tang and Anfinogenova 2008), phenotypic switching (Schwartz, Virmani, and Rosenfeld 2000), transmigration and proliferation during

expansive remodelling, all features which promote development of advanced atherosclerotic lesions. When the arterial wall is subject to disturbed tissue mechanical and fluid environment, there is significant biochemical crosstalk between ECs and SMCs (**Figure 14**). It would be interesting, yet unaddressed, to investigate whether precise changes in the mechanical environment of SMCs could lead to promotion of different atherosclerotic plaque phenotypes.

In summary, despite the insight gained from *in vitro* studies, the mechanical environment of coronary lesions is under constant change due to changes in vessel wall composition and structure and it is best to put the lessons learned into the context of the evolving disease which may not reflect the conditions studied. For example, while ESS may be more easily measured and imposed on cultured cells, orbital shakers or other custom-made flow units, *in vivo* strain is far more difficult to measure. Either way, assessing shear and stress/strain separately is a challenge and most studies linking biomechanics to EC and SMC biology have considered these separately which is not reflective of the *in vivo* environment. *In vivo* studies need animal models some of which may not be good approximations to human disease, such as mouse models (Seok et al. 2013), besides and studying coronary biomechanics is very challenging. Porcine models of atherosclerosis may be more suitable to study coronary artery biomechanics because they develop human-like plaques. Due to the resemblance of the porcine coronary vasculature to human, they can be a good approximation for computational modelling with FSI approaches before translation into the clinic. In the last 20 years there has been a staggering progress in biomechanical modelling of the arterial wall. The next

subchapter will provide a succinct review of various attempts their limitations and unmet needs.

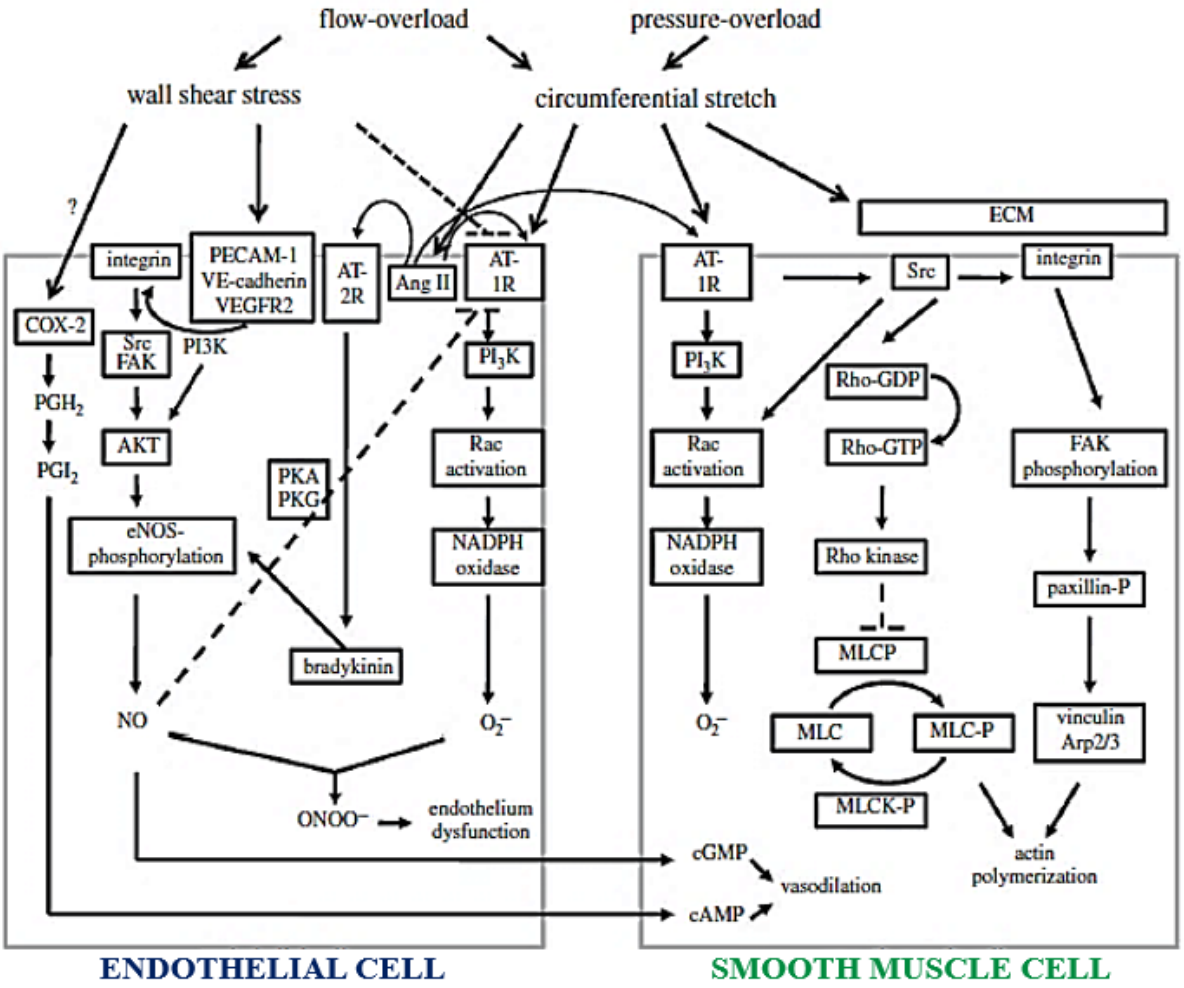

Figure 14 Signalling pathways and biochemical crosstalk between ECs and SMCs when exposed to disturbed flow and stretch. Adapted from Lu and Kassab (2011).

3.3. Role of biomechanics in plaque formation and development in vivo

3.3.1. Role of ESS in the development of atherosclerosis

The major body of evidence concerning the role of ESS in atherosclerosis is derived from *in vitro* and *in vivo* animal studies. In the previous section the in vitro findings were outlined. In this section, some studies will be summarised concerning the role of the biomechanical environment in initiation and progression of coronary atherosclerosis. Although some of these studies imposed flow patterns by the use of intra- or perivascular devices which do not always resemble human blood flow conditions, they nonetheless improved our understanding regarding the role of ESS in atherosclerosis.

Surgical manipulation of flow within animals with a genetic defect in LDL metabolism (hypercholesterolaemia) accelerated formation of advanced plaques which enabled longitudinal investigation of the disease. Winkel et al. (2015) provides a comprehensive review of the various surgical methods used to achieve this in animal models in the past, namely arteriovenous fistula, arterial ligation or by using flow-modifying devices, such as vascular grafts, peri- or intravascular devices. Such methods have minimised the duration for focal manifestation of atherosclerosis in mice (Cheng et al. 2005), rabbits (Kenjeres and de Loor 2013), swines (Himburg et al. 2004) and pigs (Gambillara et al. 2006) and enabled investigation of the longitudinal effect of shear on plaque formation and development, given the limitations in studying the disease longitudinally in humans.

Two studies demonstrated the causal relationship of disturbed flow with plaque formation. The first one, in Cheng et al. (2006), a constrictive perivascular cast was surgically placed around the left carotid artery of Apo-$E^{-/-}$ mice, the right carotid artery was used as control. The cast was designed to create a stenosis creating three distinct shear regions. A low, unidirectional shear region upstream to the cast, a high shear region within the cast (acceleration) and a low (magnitude) and oscillatory (direction) shear downstream of the cast. After 8 weeks post instrumentation advanced plaques with thin fibrous cap plaques formed upstream while plaques with a thick cap formed downstream whereas the mid region remained devoid of disease.

A more recent study have demonstrated that imposing flow disturbances – native to predilection sites – further accelerated the development of advanced atherosclerotic plaques within the coronary arteries of hypercholesterolaemic Yucatan minipigs (Pedrigi et al. 2016; 2015). A shear modifying intravascular stent with a stenotic throat was surgically placed within the right coronary arteries while the other two served as controls. Within 36 weeks of stent placement and administration of high cholesterol high fat diet, advanced plaques were formed proximal and distal to the stent. The lesions downstream of stent displayed characteristics of human histopathology such as high plaque burden, necrotic core formation, fibrous cap inflammation, expansive remodelling rendering them more suitable animal model for emulating human pathology. Advanced plaques were observed in locations initially exposed to low and multidirectional ESS as analysed with CFD software.

The study of the effect of flow on the course of atherosclerosis with *in vivo* animal models prompted the formulation of various shear metrics in a quest to identify characteristics of disturbed flows that correlates best with developed plaques. The metrics quantify changes in the direction of shear as well as magnitude. The low, oscillatory ESS theory (Caro, Fitz-Gerald, and Schroeter 1971; Ku et al. 1985) underlies most current investigations of lesion localisation but not all studies have supported it (Peiffer, Sherwin, and Weinberg 2013). Mohamied et al. (2015) showed that the multidirectionality of ESS during the cardiac cycle, characterised by the metrics quantifying components of ESS transverse to main flow direction, may be a more significant factor for plaque initiation.

After the useful findings of animal studies, application of wall shear calculation in human coronaries became more frequent, with a view to improve estimates of plaque vulnerability based on morphological features of plaques as derived by intracoronary imaging alone (Stone et al. 2011). Two non- invasive modalities have seen wide-spread use for morphological evaluation of advanced coronary plaques: IVUS and OCT. While both of them have been used to derive patient-specific 3-D lumen reconstructions to be analysed with CFD software, the former has been also used to derive surrogates of *in vivo* composition by using an enhancement called VH-IVUS; that is based on the ultrasonic properties of different plaque tissue types.

The PROSPECT study (Stone et al. 2011) was first large scale study which evaluated how lesion-specific morphological characteristics can be markers of plaque progression and ultimately leading to future acute cardiac events,. In this study, n=597 patients were enrolled presenting with ACS and underwent intracoronary imaging with virtual histology IVUS. One of the main findings was that culprit lesions and non-culprit lesions were equally probable to cause MACE at follow-up(3.4 years) on the sole basis of morphological criteria for plaque vulnerability such as large plaque burden. Another finding was that non-culprit lesions that advanced to culprit, were mildly stenosed, and had large plaque burden and were classified (on the basis of IVUS) as thin cap fibroatheromas.

The PREDICTION study (Stone et al. 2012) investigated whether knowledge of the local ESS of culprit and non-culprit lesions would improve predictive ability for re-occurrence of MACE in n=507 patients. Similar to the previous trial, all patients were

screened with VH-IVUS at baseline and had a percutaneous coronary intervention. A large proportion of them (74%) were followed up after 6-10 months to assess the natural history of the lesions. Coronary angiography and intravascular ultrasound were used to derive 3-D reconstructions of all three main coronary arteries of each patient. Those reconstructed lumen models were used to estimate the local ESS with CFD software. One of the main findings of this study is that low local ESS when combined with large plaque burden at baseline improved the positive predictive value of the latter to identify lesion progression at follow-up from 22% to 41%.

More recently, the PROSPECT dataset was analysed post-hoc (Stone et al. 2018) in order to investigate whether culprit and non-culprit lesions at baseline which led to MACE at follow up, could be traced back on the local ESS conditions. In total n=147 lesions were analysed in n=97 patients. The outcome of this study was that knowledge of local low shear stress at baseline provided little predictive benefit of the lesions' progression at follow-up.

In another clinical trial, Kok et al. (2019) computed a range of metrics of disturbed flow in IVUS-based, fluid-only numerical models of twenty (20) 3D-reconstructed human coronary arteries. Coronary plaque geometry and composition was estimated with VH–IVUS. Their major conclusion was that multidirectional shear and low time-average shear stress contributed to increase in necrotic core area size ($p>0.05$), dense calcium ($p>0.05$) and but decrease ($p<0.05$) in total plaque area, area of fibrofatty tissue and fibrous tissue after a follow-up period of 6 months, thus promoting destabilisation.

Despite attempts to predict future MACE on the basis of plaque anatomical features and vascular profiling, still the added clinical value of the above studies is little. The reason why this is the case may be two-fold: One reason may be the poor resolution of VH-IVUS poor resolution and incapability to structurally segment plaque in a reliable way and detect thin cap fibroatheromas (fibrous cap < 65μm). It is still uncertain exactly what VH actually measures giving rise to questions about its scientific validity and clinical value (Nissen 2016). The first study which attempted to validate the measurements of VH-IVUS with known histological data from an *in vivo* porcine model found no correlation between the former and examination of atherosclerotic porcine coronary artery tissue (Thim et al. 2010).

On a second note, computational efforts to understand the *in vivo* haemodynamics of diseased coronary arteries with OCT-based 3D reconstructions are certainly more accurate than IVUS-based reconstructions (Papafaklis et al. 2015; Guo et al. 2019). However, even though the usage of a higher resolution modality results in more accurate computational models, the high sensitivity of advanced plaques to locations of disturbed shear proves to be a double-edge sword due to the low specificity of low ESS to identify locations at a high risk for rupture.

Evidence about high shear is controversial; some argue that endothelial denudation can lead to thrombosis by damaging the endothelium (Eshtehardi et al. 2017), while others say it is protective (Malek, Alper, and Izumo 1999), there is an increasing body of evidence supporting that supra-physiological values can be detrimental to endothelial health (Wentzel et al. 2012). Given that ESS is three orders of magnitude smaller than plaque structural stress, it is now believed that it may be insufficient for plaque rupture by thrusting the plaque in the direction of flow– a claim which was popular in the 1970s (Caro 2009).

While vascular profiling of coronary arteries on the basis of ESS has been added in the arsenal of clinicians, the added predictive value has been incremental. These observations and findings from ESS evaluation of human coronary arteries have encouraged the development of structural biomechanical models to evaluate stress concentrations within plaques dependent on their composition.

3.3.2. Role of plaque structural stress in the progression of atherosclerosis

Plaque biomechanical environment consists of ESS (as reviewed in previous section) and plaque structural stress (PSS). Histopathological studies underline that plaque composition and structure are primary determinants of an acute coronary event (Falk 1992; Falk, Shah, and Fuster 1995; Virmani et al. 2000; 2003; Bentzon et al. 2014). These findings have encouraged the development of structural biomechanical models to evaluate stress concentrations within plaques dependent on their composition. Most biomechanical studies focus on deriving estimation of plaque rupture risk, whereas prospective studies that use PSS as a prognostic tool are comparatively fewer (**Table 3**).

Table 3 List of FEM/FSI studies evaluating biomechanical stresses in human atherosclerotic coronary arteries and linking them to plaque progression with details regarding the imaging modality used for vessel reconstruction, structural segmentation, the material model used for each histological/structural group, source of material properties, and FE modelling approach. HYP: hyperelastic, ISO: isotropic, INC: incompressible, LIN-EL: linearly elastic, INF: incompressible fluid.

Study	Imaging modality	Structural segmentation	Material model	Source of material properties	FE model
Brown et al. (2016)	VH-IVUS	Vessel wall (VW), Fibrous tissue (FT) Necrotic core (NC), Dense calcification (DC)	HYP, ISO, INC HYP, ISO, INC HYP, ISO, INC LIN-EL	VW, FT, NC: uniaxial extension of human carotid plaques from Teng et al. (2014) DC: nanomechanical properties from Ebenstein et al. (2009)	3-D FE
Costopoulos et al. (2019)	VH-IVUS	Vessel wall Fibrous tissue, Necrotic core, Dense calcification Blood	HYP, ISO, INC HYP, ISO, INC HYP, ISO, INC LIN-EL INF	VW, FT, NC: uniaxial extension of human carotid plaques from Teng et al. (2014) DC: nanomechanical properties from Ebenstein et al. (2009)	Uncoupled 3-D FE and CFD
Costopoulos et al. (2020)	VH-IVUS	Vessel wall Fibrous tissue Necrotic core Dense calcification	HYP, ISO, INC HYP, ISO, INC HYP, ISO, INC LIN-EL	VW, FT, NC: uniaxial extension of human carotid plaques from Teng et al. (2014) DC: nanomechanical properties from Ebenstein et al. (2009)	3-D FE

Based on **Table 3**, four main conclusions can be drawn.

- **First,** all studies were done in human coronaries. The close resemblance of porcine coronary vasculature to human can serve as a good candidate for building up structural complexity of FSI approaches before application to humans.
- **Second**, all studies used IVUS for vessel wall reconstruction, and Virtual Histology for segmenting areas within the diseased intima. The issues with validity of the IVUS have been discussed in the previous section. The clear advantages of an in vivo measurement (as in VH-IVUS) comes at the expense of resolution (resolution 150-200μm) and accuracy as other studies have highlighted. It should be noted that advanced plaques with fibrous caps is expected to be thinner when tissue is stretched under luminal pressure *in vivo*.
- **Third**, all studies used properties from other studies and from different vascular beds. According to Akyildiz et al.(Akyildiz, Speelman, and Gijsen 2014), these properties this can vary by several orders of magnitude even for the same vascular bed.
- **Fourth**, main mechanical testing modality is compression/tensile tests. Plaque rupture occurs at a much finer scale (at least microscale) according to

histopathological reports and more detailed techniques are needed to address local tissue mechanics.

3.4. Conclusions

The low positive predictive value of current plaque characterization methods with angiography and intracoronary imaging (IVUS and OCT) indicates that additional information is needed to identify vulnerable plaques in a way that has clinical utility. It is likely that plaque biomechanical (fluid and tissue mechanical) forces within the arterial wall act in a synergistic manner with anatomic and biochemical vulnerable plaque features to increase plaque vulnerability, promote destabilization, and produce clinical events. The most extensively studied biomechanical forces are ESS and PSS. Although the complex nature of disturbed flows is better understood, this has not been translated in clinical benefit for prospective patient specific studies due to the high sensitivity and low specificity of metrics quantifying disturbed shear. It is accepted that structural forces can undermine the structural integrity of advanced plaques by instigating local rupture where local material stress is greater than material strength. The understanding of change of PSS from health to disease is much less understood. It is yet unclear how precise changes in the biomechanical environment could trigger specific alterations in plaque composition as well as influence a mechanism in acute events such as plaque rupture. Coupled approaches may provide a much more comprehensible toolset to describe coronary plaque biomechanics than one-sided approaches, given the biomechanical complexity of the coronary vasculature. In an attempt to understand *in vivo* plaque composition affects plaque biomechanics, FSI approaches are based on VH-IVUS is which is a tool whose accuracy is debated while there are imaging modalities with finer resolution such as OCT. Moreover, material properties for FSI models in the literature are sourced from macro-mechanical tests which may not be suitable to derive predictions about plaque rupture risk given the plaque rupture occurs at a local scale and it is dependent on local composition and microstructure according to histopathological reports. Porcine models of atherosclerosis can be a valuable source of samples for mechanical testing and a basis for refinement of FSI approaches before translation to the clinic.

4. Mechanical characterisation of coronary plaques for biomechanical modelling – Emergence of Atomic Force Microscopy for extracting local plaque mechanics

4.1. The anisotropic biomechanical properties of atherosclerotic plaques

Biomechanical stress analyses with numerical models are contingent on mechanical properties of atherosclerotic plaques. Along with an accurate representation of the geometrical plaque features and physiologically relevant loading and boundary conditions, selection of appropriate plaque properties for coronary biomechanical modelling is the third pillar upon which reliable stress estimation are based. Since the atherosclerotic intima comprises the largest volume of an advanced atherosclerotic plaques (Virmani et al. 2000; Falk et al. 2013a), appropriate mechanical characterisation of this region is critical.

The diseased arterial wall is heterogenous in composition that confers plaques with anisotropic (i.e. direction-dependent) strength. The anisotropy stems primarily from the co-existence of stiff, such as collagen-rich fibrous intima, or rigid elements such as, calcium deposits, along with soft elements with no support matrix, such as lipid-rich areas. Recent biomechanical studies support the view, that local variations in plaque stiffness are primary determinants of stress concentrations within plaques (Holzapfel et al. 2014; Brown et al. 2016). However, relatively few studies have examined the local tissue stiffness, despite the need for rigorous quantification of both metrics to accurately determine plaque rupture risk.

Several studies have attempted to associate plaque stiffness to composition. Ebenstein et al. (2009) conducted nano-indentation experiments in calcified carotid human plaques and reported a considerable variation in plaque stiffness for the following tissue categories: hematoma (mean ± standard deviation, 0.23 ± 0.21 MPa, CV=0.91, CV: coefficient of variation, n=34 sites), fibrous tissue (0.27 ± 0.15 MPa, CV=0.55, n=172 sites), partially calcified fibrous tissue (2.1 ± 5.4 MPa, CV=2.57, n=72 sites), calcification (690 ± 2300 MPa, CV=3.65, n=99 sites). In another study, Tracqui et al. (2011) performed micro-indentation measurements in aortic plaques and reported different plaque stiffness from Apo-E knockout mice for different plaque types, qualitatively classified as lipid-rich (mean ± standard deviation, 5.5 ± 3.5 kPa, CV=0.64, n=18 sites), hypocellular fibrotic (59.4 ± 49.7 kPa, CV=0.80, n=97 sites), or cellular

fibrotic (10.4 ± 5.7 kPa, CV=0.55, n=74 sites). More recently, Chai et al. (2013) findings further highlight the heterogeneity of plaque mechanical properties using micro-indentation testing across 8 cross sections (median=30 kPa, range=885 kPa) taken from a single carotid plaque specimen. Taken together, the above studies demonstrate that plaque stiffness shows a large dispersion which can be contingent on local composition. Despite the importance of collagen for biomechanical stability, there is a paucity of data relating collagen content and microstructure on local plaque stiffness. Quantitative descriptions of tissue composition in terms of amount of tissue constituent present may be more valuable when co-registering them with mechanical properties.

In addition, plaque stiffness depends also on microstructure as different components organise themselves differently. To give an example, in advanced plaques necrotic cores have no underlying matrix structure which binds the cholesterol and dead cells together; it has been characterised as "gruel" matrix (Falk 2006; Thim et al. 2008), similar to "toothpaste" at room temperature (Falk 1992; Falk, Shah, and Fuster 1995); it consists predominantly of cholesterol esters, and cellular debris. On the other side of the stiffness spectrum, collagen is much stronger at an individual-fibril level and besides, it has a directional fibrillar structure (Fratzl 2008). Alongside current morphological markers of fibrous cap thickness and size of necrotic core, the structural footprint of variations in collagen microstructure within advanced plaques could be another metric of biomechanical vulnerability.

Collagen is considered a key constituent of atherosclerotic plaques because it confers plaques with structural integrity. It is deposited by synthetic SMCs migrated from the intima during the initial stages of the disease. There is a heterogeneous collagen distribution within plaques and the net collagen content is a result of a dynamic biochemical equilibrium: production vs degradation. Disturbed ESS can instigate extracellular matrix degradation by enzymes secreted by macrophages (Shah et al. 1995; Chatzizisis et al. 2011). Plaque rupture has been observed in caps were thin and poor in collagen content. Plaque rupture has been observed in plaque shoulders where collagen alignment is omnidirectional (Richardson, Davies, and Born 1989; Cheng et al. 1993a; Thondapu et al. 2017). The stiffness of individual collagen fibres has been initially measured as 1GPa (Fung, 1993) but no differentiation has been made across different types. In the last 20 years, more detailed and high-resolution mechanical

characterisation techniques by indentation have been employed to measure the stiffness of individual collagen fibrils with better accuracy. However, there is still considerable dispersion between studies (**Table 4**).

Table 1 Young's Modulus of type-I collagen fibrils as reported by indentation studies. Table reproduced from Stylianou et al. (2019).

References	Young's modulus on collagen		
	Collagen source	Contact model used	Young's modulus values (GPa)
Kontomaris et al. (2015)	Type I collagen from bovine Achilles tendon	Oliver & Pharr model	0.74 - 1.43
Yadavalli et al. (2010)	Type I atelocollagen from calf skin	Hertz model	1.03 ± 0.31
Minary-Jolandan et al. (2009)	Type I collagen from bovine Achilles tendon	Hertzian model, modified for cylindrical sample	1.2 - 2.2
Wegner et al. (2007)	Type I collagen fibrils from rat tail tendons	Oliver & Pharr model	3.75 - 11.5
Strasser et al. (2007)	Type I collagen fibrils from calf skin	Hertz model	1.2 ± 1

In advanced plaques the atheromatous core consists 95 percent of cholesterol, cholesterol esters and phospholipids (Small 1988). Over time cholesterol esters can transform to crystalline form which contribute to the stiffening of plaque. The softness of the lipid pool renders mechanical testing with common methods (tensile testing) particularly challenging. It should be noted that such methods might be only restricted to specimens of sufficient size. Few studies have attempted to map elastic properties of lipid-rich plaques. As discussed above, Tracqui et al. (2011) reported a stiffness of 5.5 ± 3.3 kPa (n=90 curves) for lipid-rich aortic plaques from Apo-$E^{-/-}$ mice. More recently, Rezvani-Sharif, Tafazzoli-Shadpour, and Avolio (2019b) reported a stiffness of 2.7 ± 1.8 kPa (8 sections, 160 curves) using nanoindentation testing on sections of human coronary plaques has been reported.

Calcifications are more prevalent during the advanced stages of the disease - in clinical practice the calcification score is used as a sign of plaque vulnerability - and their contribution to the biomechanical heterogeneity is important. They can be spotty (micron level) or nodular (Barrett et al. 2019). Kelly-Arnold et al. (2013) has demonstrated that micro-calcifications (in the order of 10μm) within an otherwise homogenous fibrous cap, they can double the stress concentration within the cap. Ebenstein et al. (2009) performed nanoindentation measurements in calcified human coronary plaques and reported an average stiffness for calcification 0.8 ± 2.2 GPa. Indentation tests have prevailed over traditional extension tests due to challenges of subjecting such rigid constituents to tension.

Apart from the aforementioned constituents, plaques consist of cellular components as well. The cellular components of plaques consist of SMCs, foam cells, immune cells, red blood cells (in case of an intraplaque haemorrhage). In general, the mechanical properties of SMCs depend on many factors including their phenotype and their activation state. SMCs in atherosclerotic plaques are different phenotypically from their medial counterparts (Schwartz, Virmani, and Rosenfeld 2000); their central function of the former is to synthesise ECM rather than contribute to vascular smooth muscle tone by contraction. It has been shown experimentally that the mechanical properties of SMCs are non-linear and anisotropic (Chen et al. 2013; Chen and Kassab 2017) with a Young's Modulus of 2.6 kPa (Matsumoto et al. 2004). Overall, the relative contribution of the cellular content of plaques to the overall biomechanical integrity of the plaques is considered minimal compared to that of collagen and therefore their contribution is usually omitted. However, the water content of the arterial wall both in intracellular and extracellular form is important for incompressibility, this is factored in by the majority of the models.

4.2. Methods to extract properties for computational models

There have been efforts to measure plaque stiffness with *in vivo* techniques such as intravascular palpography and magnetic resonance imaging. With intravascular palpography (Schaar et al. 2006; Gijsen et al. 2008) ultrasound waves are emitted towards the arterial wall and a stiffness map is extracted based on the displacement of each constituent. Strain mapping of the coronary wall with magnetic resonance imaging/elastography (MRI/MRE, **Figure 15**) relies on a similar principle although the source of excitation is different (Mariappan, Glaser, and Ehman 2010). Although *in vivo* mechanical properties of atherosclerotic plaques would be theoretically desirable for downstream computational modelling, their resolution (150μm for palpography, and 400μm for MRI) and appropriate validation of the proposed methodologies is a major obstacle (Mahmood et al. 2016). Further technical advancements are warranted for *in vivo* material measurements to have translational benefit for FSI modelling.

Ex vivo extension and inflation testing (macro-mechanical testing, **Figure 15**) of intact arteries or uni- or bi-axial extension of arterial strips has been the conventional method for deriving material properties for computational modelling of atherosclerotic plaques (Akyildiz, Speelman, and Gijsen 2014; Walsh et al. 2014). Experimental data on mechanical properties of coronary plaques are extremely limited due to the low tissue availability. Hence, computational attempts to simulate in vivo coronary plaque biomechanics resort to utilising properties from other vascular beds (Teng et al. 2014; Costopoulos et al. 2020; Guo et al. 2019). A recent systematic literature review (Akyildiz, Speelman, and Gijsen 2014) concluded that material curves from plaques from different vascular beds (aortic, femoral, carotid, iliac, coronary) can demonstrate a great dispersion up to five orders of magnitude (**Figure 16**). It is worth mentioning though that the magnitude of difference may not be attributable to the vascular bed *per se*, due to other disagreements among the testing protocols used.

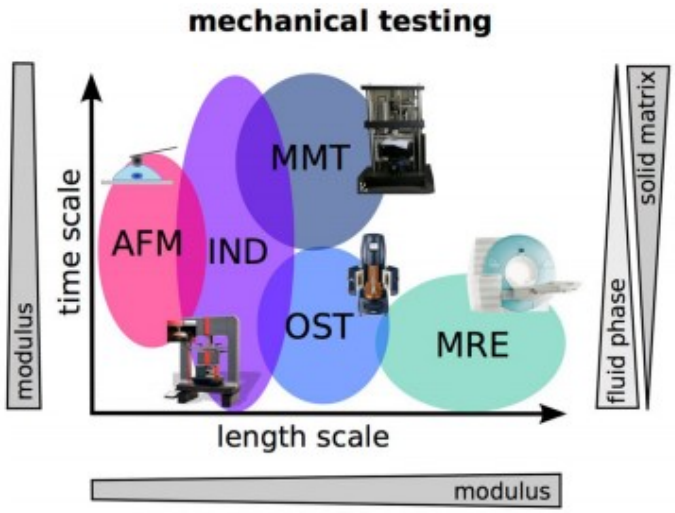

Figure 15 Mechanical characterisation techniques and their area of probation scale. MMT: macro-mechanical (tensile, unconfined compression and inflation) testing, IND: indentation testing, AFM: atomic force microscopy, MRE: magnetic resonance elastography, OST: oscillatory shear testing. Figure adapted from Budday et al. (2019).

It is very common for biomechanical models to combine VH-IVUS for extracting plaque composition and then literature values of the material properties for each plaque component. Mechanical properties from uniaxial extension of human carotid plaques are commonly used (Teng et al. 2014). VH-IVUS may be *in vivo* modality, but it is having serious limitations in addressing longitudinal and in-plane heterogeneity, constituent-

based mechanical properties as well as accurate geometrical reconstruction of advanced plaques. The accuracy of VH-IVUS for classification of plaque constituents is debated in the literature (Nissen 2016). The ability of VH-IVUS to detect rupture prone plaques is questionable not only due to its incapability to detect a TCFAs - a distinctive feature of rupture-prone plaques - but also due to the zero correlation between with VH-identified necrotic cores and ground-truth histology data from a porcine model of atherosclerosis as found in a validation study (Thim et al. 2010). According to histopathological studies, human plaques from different vascular beds could be morphologically and histologically distinct (Dalager et al. 2007). Hence, combination of the errors in geometry, in mechanical properties and in segmentation, may be less insightful in providing reliable estimates of PSS and should be dealt with caution.

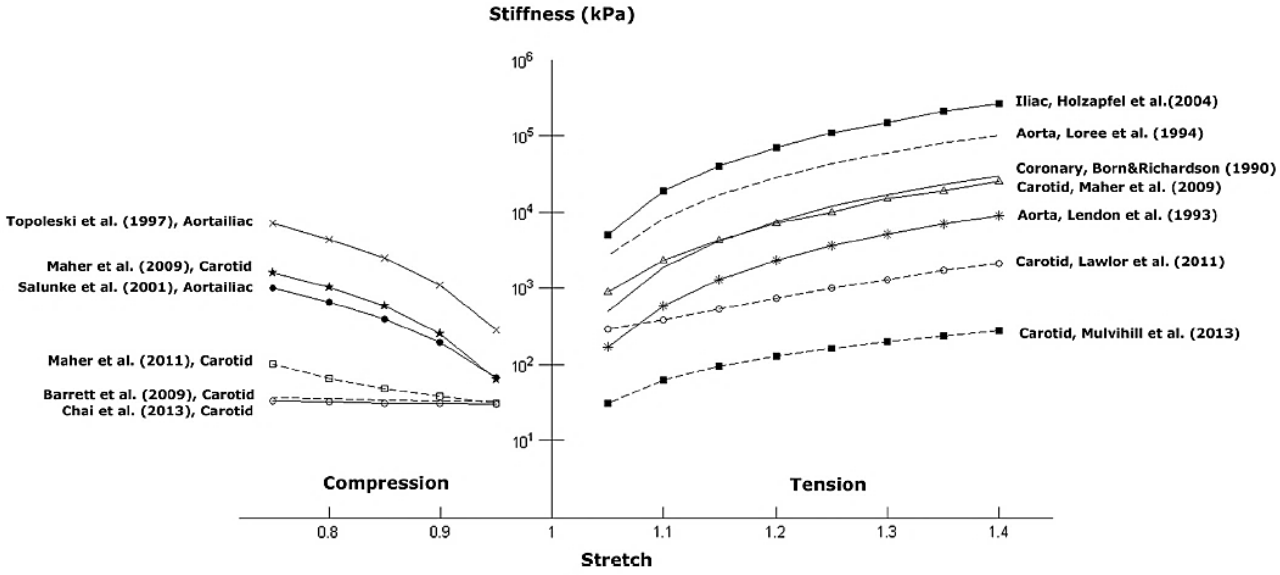

Figure 16 Summary of mechanical properties (circumferential stress – stretch) of human atherosclerotic intima from aortic, carotid, iliac and coronary arteries. Compression is unconfined. Note the much softer properties measured from micro-indentation test in Barrett et al. (2009) and Chai et al. (2013). Plot reproduced from Akyildiz, Speelman, and Gijsen (2014).

Previous histopathological studies highlight that stiff (collagen) and soft (lipid-rich core) areas within plaques may be a few microns apart may suggest that conventional tensile methods may be "out-of-scale" for determining local plaque properties the mechanical characterisation of diseased vessels may be considerably limited. One possible way to refine stress estimates would be to investigate how local

composition and structure influences local plaque mechanics. Despite the known importance of collagen in conferring plaques with strength, there has not been a FE study which incorporates mechanical anisotropy due to regional differences in collagen microstructure. Such an endeavour is currently difficult to achieve given the significantly coarser resolution of tensile testing methods. Indentation-based testing modalities such as Atomic Force Microscopy can achieve this by probing tissue on a much finer scale (from micro down to nanoscale, **Figure 15**).

4.3. Atomic Force Microscopy as a tool to derive stiffness variations within coronary plaques

Experimental set-ups where local variations in plaque stiffness can be measured by indentation can potentially overcome several of the limitations of tensile and unconfined compression testing methods. Mechanical testing by indentation, such as Atomic Force Microscopy (AFM), could be an alternative mechanical testing method which could increase the stiffness resolution in heterogenous plaque specimens. AFM belongs to the family of scanning probe microscopy whereby - in contrast to conventional light microscopy - structural information can be derived with a probe that interacts with the sample in a physical, biological or chemical manner (Krieg et al. 2019).

Over the past two decades, AFM has become one of the key tools to investigate the mechanical properties of biomolecules, biomaterials, cells, and tissues (Krieg et al. 2019). Alterations in tissue stiffness in all levels - from cellular to tissue – across a range of pathologies. Indentation testing has been insightful in fields such as ocular biomechanics (Bongiorno et al. 2016), cancer (Plodinec et al. 2012), articular cartilage biomechanics (Darling, Zauscher, and Guilak 2006), Alzheimer's disease (Zhang et al. 2013), infectivity of viruses (Kol et al. 2007), and food technology (Cárdenas-Pérez et al. 2019). Application in arterial tissue is still at infant stage. In stark contrast with tensile testing (Walsh et al. 2014; Akyildiz, Speelman, and Gijsen 2014), standardised protocols and guidelines for probing arterial tissue with indentation techniques are not widely available (Chai et al. 2014). Detailed knowledge of the mechanics of different arterial layers at a micrometric scale could be valuable in improving our understanding of the

mechanical anisotropy of arterial tissue and contribute to the development of bio-inspired structural modelling of coronary plaques.

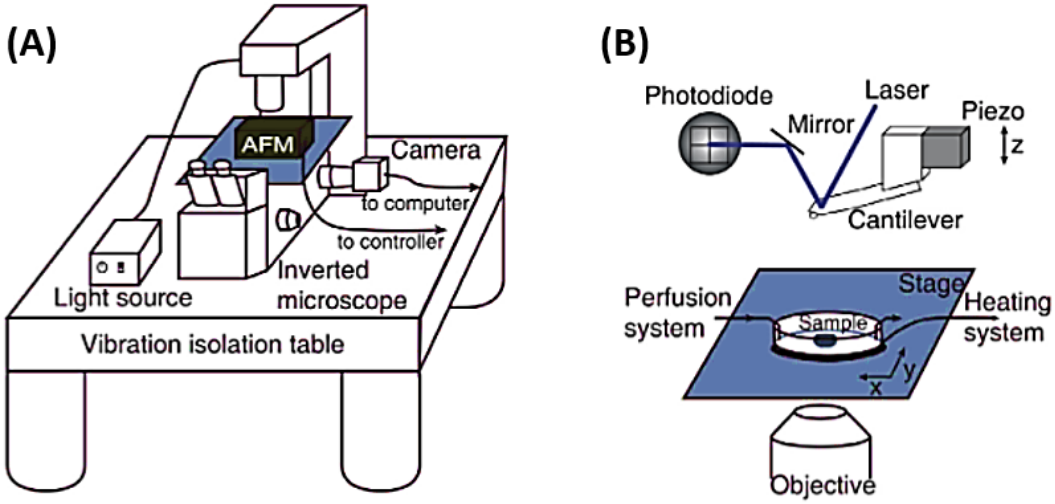

Figure 17 Overview of an atomic force microscope. (A) Experimental set-up: An inverted (epifluorescence or standard light) microscope sits on a vibration isolation table to minimise noise (B - top) Principle of measurement: a laser beam is continually focused on the back side of a cantilever that reflects towards a photodiode that measures voltage. The cantilever's vertical position (z) is measured by a piezoelectric transducer. While the cantilever indents a sample, it bends thereby altering the position of the laser spot on the photodiode which, in turn, generates a voltage proportional to the deflection of the cantilever. (B - bottom) Detail of the sample mounting area. The temperature and hydration of the sample can be regulated with a heating and perfusion systems. Figure adapted from Gautier et al. (2015).

The central element of an Atomic Force Microscope is a cantilever endowed with a tip which resembles a record player needle. The principle of measurement is, quite interestingly, electro-optical (**Figure 17B**). By and large, AFMs operate in three modes. In **contact** mode the tip rests on top of the specimen's surface and is dragged to derive topographical information. Viscoelastic properties can be quantified by switching to **tapping** mode, which is a non-contact measurement. In this mode of operation, the cantilever vibrates at a specified frequency and is brought adjacent to but not in direct contact with the specimen's surface. Lastly, in **force spectroscopy** mode the cantilever approaches the sample, indents until a certain force threshold is reached and then retracts to the initial position. The outcome of the indentation cycle is a recording of the force (F) the cantilever senses as a function of the vertical position (z) of the cantilever (**Figure 18**). By specifying a scanning path for the cantilever, multiple scans can be

serially performed over an area of interest, for instance at the intersections of a predefined grid.

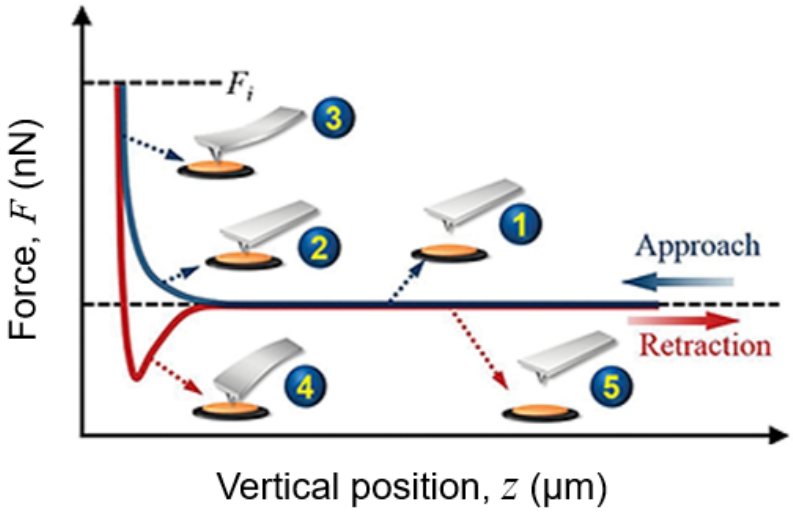

Figure 18 A typical example of a force-curve with different stages of contact noted (1-5). Blue and red curves correspond to approach and retraction stages respectively. (1) approaching, (2) initial contact, and (3) repulsive contact until threshold F_i. (4) adhesion and (5) noncontact regimes recorded upon retracting the cantilever and sample. Reproduced from Wonseok et al. (2016).

To be able to extract a measure of tissue stiffness, it is necessary that experimental force curve data be fitted to an appropriate contact model (Gavara 2017). Hertzian contact models have been applied in extracting measures of low-strain elasticity such as Young's Modulus from indentation data. The geometry of the tip determines the selection of the contact model (**Figure 19**). All contact models assume that the indentation depth does not exceed 10% of sample height. The proposed contact models rely on the following assumptions: (i) the contact geometry is axisymmetric and continuous (ii) sample is infinite half space (iii) material properties of tip and sample are isotropic and homogenous, (iv) no adhesion or friction are present between the tip and the sample.

Despite the assumptions involved in the derivation of local plaque properties indentation methods can be advantageous against tensile testing for various reasons. Firstly, derivation of micro-nano scale material properties of plaques can be valuable in understanding variation of plaque stiffness at a scale where plaque rupture occurs according to histopathological reports. Secondly, with indentation techniques there is no requirement for arterial fixation, allowing fragile plaques to be measured alongside

stiffer plaques. Thirdly, by working on tissue sections plaque stiffness data can be related to variations in local composition and microstructure which can be quantified by routine histological quantification. Similar to macro-mechanical testing methods, indentation tests take place *ex vivo* which renders plaque tissue from animal models, particularly porcine models, a great candidate for the development of new methods for mechanical characterisation of atherosclerotic coronary arteries.

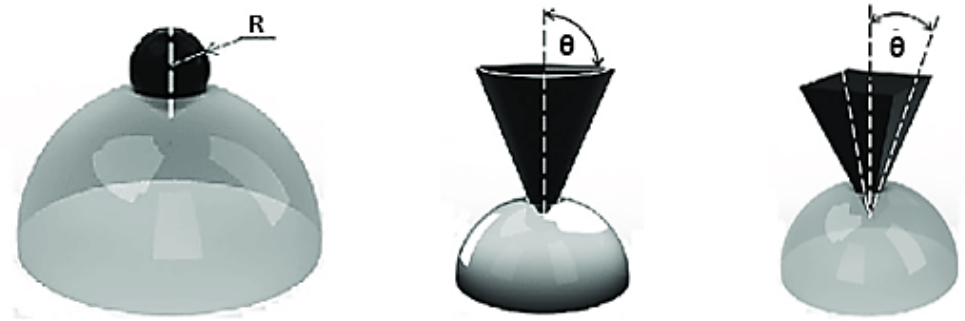

Tip geometry	Force-indentation relationship, $F(\delta)$
Sphere of radius R	$F = \frac{4E}{3(1-\nu^2)} R^{1/2}\delta^{3/2}$ (Hertz, 1881)
Cone of semi-included angle θ	$F = \frac{2E\tan\theta}{\pi(1-\nu^2)}\delta^2$ (Sneddon, 1965)
Four-sided regular pyramid of semi-included angle θ	$F = \frac{0.7453E\tan\theta}{(1-\nu^2)}\delta^2$ (Bilodeau, 1992)

Figure 19 Contact models for most common tip geometries used for probing biological tissue. F: Force, E: Young's Modulus, v: Poisson's ratio, δ: indentation depth. Schematics adapted from Cárdenas-Pérez et al. (2019).

While in the literature attempts to model the layer-wise anisotropic properties of conduit arteries to obtain a more accurate macroscopic response of arterial wall in health (Holzapfel, Gasser, and Ogden 2000) and disease (Holzapfel, Stadler, and Gasser 2005), the effect of local characteristics (amount and structure) of collagen on local coronary plaque properties is much less understood and investigated. Constituent-based material modelling for coronary plaques has been challenging in human models due to the limitations of low tissue availability. Besides, the low resolution of imaging modalities (VH-IVUS, MRI) frequently used to construct structural models poses a hindrance to constituent-based material modelling.

Because we are interested in collagen, two features of collagen microstructure which can influence local mechanical properties are collagen fibre density and orientation. To the best of our knowledge, there is no FE model of diseased coronary

arteries which includes microstructural properties of collagen in such a local scale. We believe that this addition will be add new insight on plaque biomechanics and refinement of stress estimates from coronary artery -specific data. Combined with other microscopy techniques, AFM can be a powerful tool to reveal novel information about plaque tissue mechanics that could refine structural modelling of the coronary plaques.

4.4. Conclusions

Determination of mechanical properties of human coronary atherosclerotic plaques is essential in order to obtain a more accurate estimation of the *in vivo* plaque biomechanical stress with numerical models. *Ex vivo* methods dominate over *in vivo* methods which suffer from validation issues. Until now, macro-mechanical testing (uni and bi-axial extension tests, unconfined compression, and inflation) has been the predominant method to extract material behaviour of atherosclerotic plaques. Such properties are then inputted into computational models of atherosclerotic plaques to obtain an understanding of the plaque biomechanical environment from an acute or an evolutionary perspective.

Although such modalities can capture the hyperelastic behaviour of healthy and diseased vessel wall, they may pose a hindrance to a better understanding of *in vivo* biomechanics of plaques for a number of reasons**:**

- **First**, plaques are very heterogenous in structure and composition down to the microscale. Previous biomechanical and histopathological studies suggest that regional variations in plaque stiffness is the driving mechanism for local tissue disruption. In order to obtain a more accurate understanding of tissue rupture, mechanical testing down to the microscale will need to come to the forefront.
- **Second**, the capability of macroscopic testing to relate material stiffness with local plaque composition and microstructure is limited; both of which are considered determinants of local mechanical properties. In the majority of experimental studies, co-registration of material properties to plaque characteristics has been conducted in a qualitatively and not quantitative manner.

- **Third**, tensile (uni- and bi-axial) and inflation experiments may require tissue to have certain size requirements and integrity to be suitable for testing. Therefore, properties may be biased towards stiffer plaque specimens.
- **Fourth**, it is common for coronary plaques to be modelled using material properties from other arterial beds. Although this might be understandable due to limited tissue availability, the results of such studies should be interpreted with caution. It has been reviewed that plaque from different vascular beds display great dispersion up to several orders of magnitude. The source of the variation can be traced back to differences in their tissue preparation protocol preconditioning, but it may be due to the inherent heterogeneity of plaque tissue itself.

Indentation methods such as Atomic Force Microscopy can be a useful, *ex vivo* alternative for extraction of plaque properties that could circumvent the above limitations of macro-mechanical testing. Among the many advantages of the technique are the superior resolution which enables the probation of plaques from micro to nanoscale. It can be applied in on tissue sections, providing with a unique ability to co-register local plaque stiffness with histological metrics of composition and microstructure. By combining mechanical testing and histology in the same scale it can be one step closer to the real biomechanics when applied in FE models of coronary arteries. AFM presents with great capabilities in terms of fine-tuning hyperelastic material modelling according to local composition and structure. Lastly, coronary plaques from a porcine model of atherosclerosis can be a valuable source for testing and development of such novel mechanical characterisation methods, given that standardised protocols and guidelines for probing arterial tissue with indentation techniques are generally not available.

Thesis Hypothesis and Aims

We hypothesise that the local mechanical properties of healthy and atherosclerotic coronary arteries are contingent on the local collagen microstructure.

Therefore, we intend to:

- Develop a nano-indentation protocol (**Chapter 2**) using Atomic Force Microscopy for extracting local biomechanical properties from snap-frozen coronary artery sections and develop a framework to co-register these properties to the local collagen microstructure.
- Investigate the degree to which collagen microstructure affects the biomechanical properties of non-atherosclerotic (**Chapter 3**) coronary arteries with Atomic Force Microscopy.
- Investigate how collagen microstructure affects the biomechanical properties of atherosclerotic (**Chapter 4**) coronary arteries with Atomic Force Microscopy.

Chapter 2: General Methods

1. Porcine model of accelerated coronary atherosclerosis in D374Y-PCSK9 hypercholesterolemic minipigs by imposed flow perturbation

A genetically engineered porcine model of atherosclerosis with familial hypercholesterolaemia (Al-Mashhadi et al. 2013) was used as the basis of developing novel, AFM-based material characterisation methods for coronary arteries. All animal experiments were performed in accordance with the ethical and welfare regulations of the Northwick Park Institute of Medical Research (ethical approval number: RDS.IC/02/18). Advanced lesion formation was further accelerated in those animals by surgical implantation of a stenotic stent/shear modifying stent (**Figure 20**) according to previous work (Pedrigi et al. 2015). All catheterisation procedures were performed by an experienced cardiologist (Dr. Ranil de Silva). In fact, five female Yucatan minipigs were placed in cholate-free, high-fat, high-cholesterol diet. The left anterior descending coronary arteries (n=5) were left unstented and served as control. A stenotic stent was placed in four (n=4) right coronary arteries. Due to small size of the RCA of one of the pigs, the stenotic stent was alternatively placed in the left circumflex artery (LCx, n=1)

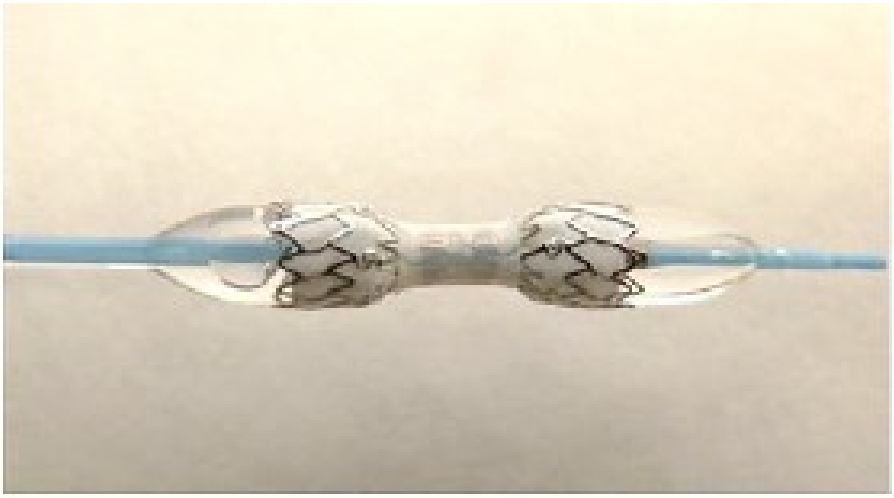

Figure 20 Stenotic stent used for perturbing flow in hypercholesterolaemic D374Y-PCSK9 minipigs. Figure reproduced from Foin et al. (2013).

X-Ray angiography, intracoronary fourier domain OCT (FD-OCT), near-infrared spectroscopy IVUS (NIRS-IVUS) and single catheter Doppler measurement of flow and pressure (Combowire) were performed in all minipigs at baseline (0), right after SMS placement (0+) and followed up for all animals at 4 weeks and at 18 weeks post stent

implantation (**Figure 21**). At the end of each follow-up catheterisation procedure the animals were returned back to the stable for continual care, administration of a cholate-free high-fat, high-cholesterol diet and study medications.

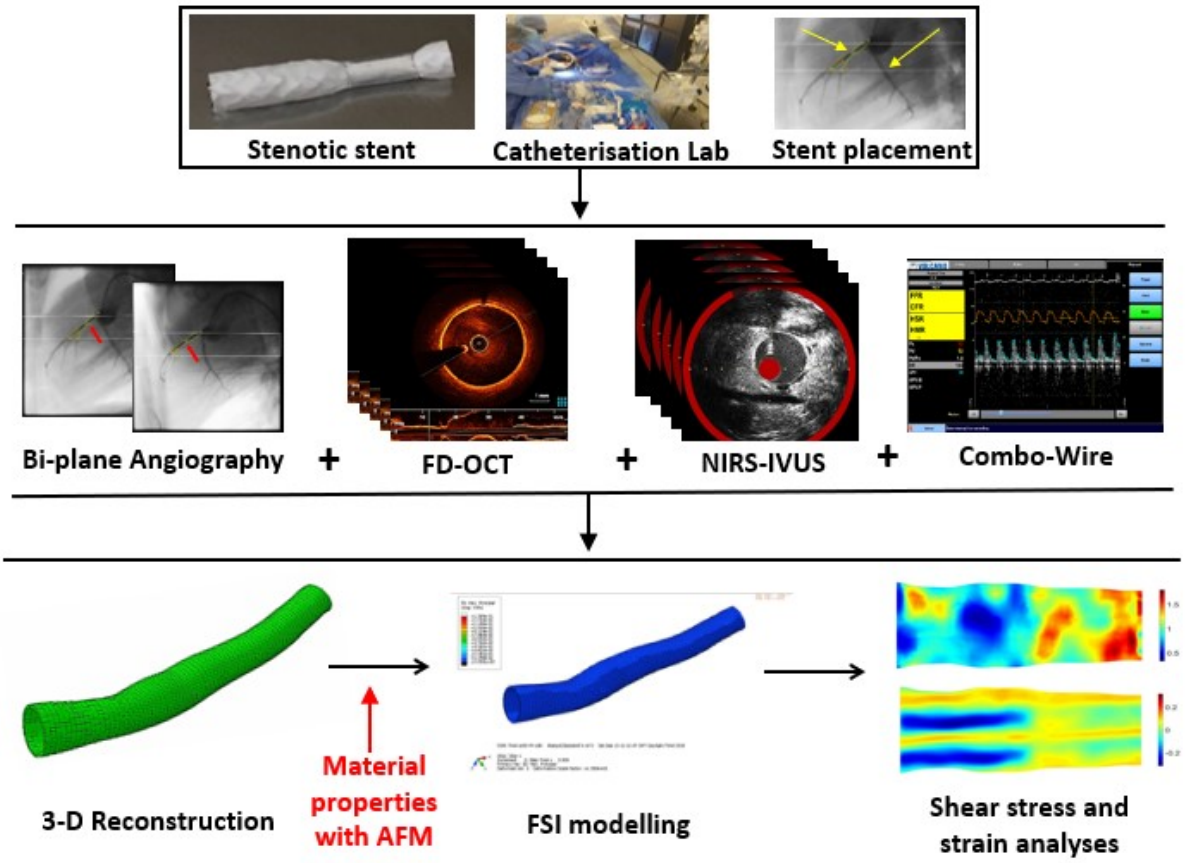

Figure 21 Overview of the experimental and computational pipeline used to study the colocalization of disturbed biomechanics and advanced plaques. Material properties of coronary arteries are a necessary requirement for downstream computational modelling. In this work we used Atomic Force Microscopy as a high-resolution alternative to macroscale testing methods.

In vivo Imaging

All animal experiments were performed in accordance with the ethical and welfare regulations of the Northwick Park Institute of Medical Research.

X-Ray Angiography

A 6-8F coronary guiding catheter was advanced into the left coronary ostium under X-ray fluoroscopic guidance. X-ray coronary angiograms be identified after hand injection of iodinated contrast agent (Visipaque 320, GE Healthcare, Oslo, Norway).

Catheters were flushed regularly with heparinised saline and coronary engagement pressures measured from the guiding catheter through a standard coronary pressure manifold. After identifying the isocentre, intracoronary isosorbide dinitrate (0.1-1 mg) was administered into each coronary artery before acquisition of angiograms. Selective angiography of the left and right coronary arteries were acquired in multiple projections, during which ventilation was briefly suspended (<15 sec) on expiration during each cine acquisition. Unfractionated heparin (50-80 u/kg) was administered after acquisition of baseline coronary angiograms.

Intracoronary ComboWire assessment

Coronary flow velocity and pressure were measured in the LAD and LCx and RCA using a ComboWire (Volcano Corporation, USA). Through the guiding catheter, a 0.014" ComboWire was placed in each of the proximal and distal portions of the LAD, LCx and RCA arteries. Doppler velocity and pressure measurements were made at multiple locations in the above vessels. Prior to measurement the ComboWire was advanced to the tip of the guide catheter, where aortic pressure and ComboWire pressures were equalised. It was then advanced into a proximal vessel segment at least 5 mm away from any major angiographic side branch (>2 mm diameter) to measure the inlet velocity over 10 – 20 stable cardiac cycles. Physiological parameters, oxygen saturations, end tidal CO_2 and ECG were continuously monitored throughout the duration of the experiment.

Fourier Domain Optical Coherence Tomography (FD-OCT)

An OCT catheter (sheathed C7 Dragonfly, St. Jude Medical, USA) was passed over an 0.014" intracoronary guidewire into each of the main epicardial coronary arteries and selected side branches. Once each imaging location has been identified, the position of the catheter was imaged fluoroscopically in orthogonal views, during which ventilation were briefly suspended (<15 sec) on expiration during each cine acquisition. Pullbacks were performed during injection of iodinated contrast agent either by hand injection or using a pump injector.

Near Infrared Spectroscopy Intravascular Ultrasound (NIRS-IVUS)

A NIRS-IVUS catheter (InfraredX, USA) was passed over the 0.014" intracoronary guidewire into each of the main epicardial coronary arteries and selected side branches. Once each imaging location had been identified, the position of the catheter was imaged fluoroscopically in orthogonal views, during which ventilation was briefly suspended (<15 sec) during each cine acquisition. Pullbacks were performed at 0.5-1.0 mm/s.

2. Development of a mechanical testing protocol with Atomic Force Microscopy protocol for frozen coronary arteries and co-registration local tissue properties with local collagen microstructure

2.1. Introduction

Indentation techniques have been long been employed to study the mechanical properties of cells, which has resulted in abundant documentation (Gavara 2017; Gavara and Chadwick 2013). On the contrary, guidelines regarding application in arterial tissue is rather limited compared with the ample resources that can be found for tensile testing (Walsh et al. 2014). Among the studies which investigated arterial mechanics with indentation techniques (**Table 5**) the vast majority focused on large elastic arteries such as the aorta; while application in coronary arteries is scarce due to the limited tissue availability. Porcine models of coronary atherosclerosis can be valuable in trying new material testing techniques, such as indentation testing, as the coronary vasculature bears great resemblance to human.

Therefore, this chapter discusses the development of an indentation testing protocol to extract mechanical properties of porcine coronary artery sections and co-registration of them with metrics of local collagen microstructure. The protocol will be presented in the following order: first, the preparation of tissue sections and essential materials & reagents will be presented. Secondly, the process of the development of the indentation protocol and the method to extract material properties from indentation data will be discussed. Thirdly, the derivation of metrics to quantify collagen microstructure and how they were co-registered with the aforementioned material properties will be discussed. Fourthly, the error in estimation of material properties from indentation is calculated.

Table 5 List of micro- and nano- indentation studies on arterial tissue which has been thawed from snap-freezing with special focus on tissue preparation practice, probe and tip characteristics and indentation conditions.

Study	Tissue type and preparation	Probe & tip characteristics	Indentation conditions
Sicard, Fredenburgh, and Tschumperlin (2017)	Species: human Artery: pulmonary Thickness: 10,20, 50 µm Adhesive: poly-L-lysine	Stiffness: 0.4-1.32 N/m Tips: pyramidal and spherical Diameter: 2 & 5 µm	Indentation speed: 20.6 µm/sec Force threshold: 25 nN Hydration: PBS Temperature: ambient
Hemmasizadeh et al. (2015)	Species: porcine Artery: aorta Thickness: 8-10 mm	Stiffness: not reported Tip: conical, 55 degrees Diameter: 20 µm	Indentation depth: 40 µm, Hydration: none Temperature: not reported
Hemmasizadeh, Darvish, and Autieri (2012)	Species: porcine Artery: aorta Thickness: 8-10 mm	Stiffness: not reported Tip: conical, 55 degrees Diameter: 20 µm	Indentation depth: 40 µm, Hydration: none Temperature: not reported
Grant and Twigg (2013)	Species: porcine Artery: aorta & pulmonary Thickness: 12 µm Adhesive: poly-L-lysine	Stiffness: 0.32 N/m Tip: spherical Diameter: 10 µm	Indentation speed: 4 µm/sec Force threshold: 20 nN Hydration: ultrapure water Temperature: 37°C
Beenakker et al. (2012)	Species: porcine, Artery: aorta Thickness: 8 µm	Stiffness: not reported Tip: spherical Diameter: 20 nm & 10 µm	Force threshold: 20 nN Hydration: PBS Temperature: 37°C
Akhtar et al. (2009)	Species: ferret, aorta & vena cava Thickness: 5 µm	Stiffness: not reported Tip: cono-spherical Diameter: 10 µm	Loading rate: 200 µN/sec Force threshold: 10 mN Hydration: none Temperature: not reported
Matsumoto et al. (2004)	Species: porcine, Artery: pulmonary Thickness: 0.15 mm	Stiffness: 0.3 N/m Tip: conical Diameter:3-5 µm	Hydration: PBS Temperature: ambient
Rezvani-Sharif, Tafazzoli-Shadpour, and Avolio (2019a)	Species: human Artery: aorta Thickness: 20 µm Adhesive: yes, but not specified	Stiffness: 0.15 N/m Tip: conical	Loading rate: not reported Force threshold: not reported Hydration: PBS Temperature: ambient
Rezvani-Sharif, Tafazzoli-Shadpour, and Avolio (2019b)	Species: human Artery: coronary Thickness: 20 µm Adhesive: poly-L-lysine	Stiffness: 0.15 N/m Tip: conical Diameter: Nanoscale, not specified	Loading rate: not reported Force threshold: not reported Hydration: PBS Temperature: ambient
Chai et al. (2013)	Species: human Artery: carotid Thickness: 200 µm	Stiffness: not reported Tip: spherical Diameter: 2 mm	Indentation speed: 1.5 mm/s, Indentation depth: 60 µm (30%) Hydration: none Temperature: not reported
Tracqui et al. (2011)	Species: murine Artery: aorta Thickness: 16 µm Adhesive: poly-L-lysine	Stiffness: 0.1-0.3 N/m Tip: spherical Diameter: 5 µm & 12 µm	Indentation speed: ~0.6 µm/s Indentation depth: 0.5-1 µm Temperature: ambient Hydration: KH buffer
Barrett et al. (2009)	Species: human Artery: carotid Thickness: 0.5 mm	Stiffness: not reported Tip: spherical Diameter: 1 mm	Ind. speed: 20 mm/min Force threshold: 200 mN Indentation depth: 5-20% of thickness
Ebenstein et al. (2009)	Species: human Artery: carotid Thickness: not reported	Stiffness: not reported Tip: cono-spherical, Diameter: 200 µm	Force threshold: 600 µN Indentation depth: 5 µm Temperature: ambient
Chang et al. (2018a)	Species: human Artery: internal mammary Thickness: 5µm	Stiffness: 5 N/m Tip: cono-spherical Diameter: 16 nm	Force threshold: not reported Indentation depth: not reported Temperature: 21°C
Chang et al. (2018b)	Species: human Artery: internal mammary Thickness: 5µm	Stiffness: 0.7 N/m Tip: cono-spherical Diameter: 40 nm	Hydration: yes, but no referral to hydration agent Temperature: 21°C
Akhtar et al. (2016)	Species: sheep Artery: aorta Thickness: 5 µm	Stiffness: 0.2 N/m Tip: spherical Diameter: 10 µm	Force threshold: not reported Hydration: PBS Temperature: ambient

2.2. Materials

2.2.1. Tissue harvesting, cryopreservation & cryo-sectioning

For the purposes of developing the AFM protocol and to minimise the number of animals used, coronary tissue from healthy animals (not from cardiovascular research) were used. All procedures were approved by the Northwick Park Institute of Medical Research (NPIMR) ethical committee.

Epicardial coronary arteries were carefully excised from the heart muscle and were cut in 5mm long segments. Each segment was embedded in Optimal Cutting Temperature compound, Thermo Fisher Scientific GmbH, Germany) where it had its longitudinal axis manually aligned in parallel with and was snap frozen in iso-pentane (2-methylbunane, 99+%, Thermo Fisher Scientific GmbH, Germany) which resulted in a solid rectangular, ice block. The rapid freezing prevents the formation of ice crystal dendrites, which can damage the tissue as previous literature has shown (Bakhach 2009; Venkatasubramanian et al. 2006). Once solidified, the vessel orientation was marked and was wrapped with aluminium foil, labelled, and stored at -80°C until further use. It is believed that cryopreservation at -80°C has no significant effects on tissue mechanical properties (Hemmasizadeh, Darvish, and Autieri 2012; Devireddy et al. 2003; Masson et al. 2009). All blocks of each of the animals were prepared within 2 h post-mortem. This procedure was done by an experienced histologist (Dr. Daniele Carassiti).

The cryo-sectioning of the frozen tissue blocks was also conducted by Dr. Daniele Carassiti at the Blizard Institute of Molecular Science at the Queen Mary University of London (QMUL). Frozen tissue blocks were taken out of the -80°C freezer and placed within the cryostat chamber (-30°C) so that they reach the cryostat's ambient temperature. After fixating the blocks onto the cryostat chuck, its orientation was manually adjusted to ensure the sectioning plane was perpendicular to the longitudinal axis of the arterial segment. The orientation of sectioning was opposite to blood flow direction (distal to proximal). A sterilised blade was used each time. Sections of 20µm thickness were obtained. Immediately after cutting, the sections were carefully picked up with a poly-L-lysine coated coverslip (Section 2.2.2). The coverslip was then placed inside a 35mm, sterile plastic petri dish (Sigma Aldrich, St. Louis, MO, USA) in the cryostat chamber to let the tissue fully adhere. To prevent the formation of any

condensation, the petri dish was tightly sealed with laboratory film (Parafilm, Sigma Aldrich, St. Louis, MO, USA).

The samples were preserved in dry ice and transported to the Atomic Force Microscopy (bioAFM) workspace at the School of Engineering and Materials Science of QMUL. Measurements were performed using a JPK NanoWizard 4 AFM instrument (Bruker, Billerica, MA, USA) mounted on the stage of an Axiovert 200 inverted microscope (Carl Zeiss, Göttingen, Germany) placed on a vibration-isolation table (Newport Isostation, Irvine, CA, USA). Nano-indentation measurements were carried out using the "Force Mapping" of the "Force Spectroscopy" mode. Using the optical microscope integrated with the AFM setup, the media was identified and the probe was placed over it prior to any testing. All testing was conducted with a scan rate of 1 Hz. Along with elastic modulus maps, the force mapping method produced topographical maps. The topographical maps were used to optimise the Z-length (Section 2.3.3). In principle, due to the high number of optimisation parameters, a literature review (Table 5) helped to identify the key parameters (probe selection, presence of hydration, duration of the scans, Z-length, force threshold, indentation speed, probe decontamination) that modulate the force mapping process and therefore attention was drawn to those only (Section 2.3).

2.2.2. Optimisation rounds of the tissue substrate

In the first round, each tissue section was laid inside plastic petri-dishes where they underwent mechanical testing. Later, it was found that the material of the petri dish was eroded by the downstream histochemical process. In the second round, petri dishes with a circular hole were custom fabricated and a plain glass coverslip was glued to the bottom side of the petri dish with instant adhesive. While this modification rendered both the mechanical testing and histochemical staining almost seamless, the lack of a common frame of reference impaired the co-registration process that was not mitigated with fiducial markers. The limited field of view of the AFM microscope (lowest magnification 10x) further complicated the macro-imaging of the entire cross section and co-registration with the stained tissue image even with an ink fiducial marker.

We concluded on using glass coverslips with an imprinted 50μm grid (Ibidi GmbH, Martinsried, Germany) as a substrate (**Figure 22**). The cryosectioned tissue was picked up by a coverslip and, in turn, the coverslip was placed in a plastic petri dish to

proceed with the AFM testing in a liquid environment (**Figure 22A**). The coverslip would be then removed from the petri dish and be stained for collagen according to the developed protocol (described in Section 3, Chapter 2).

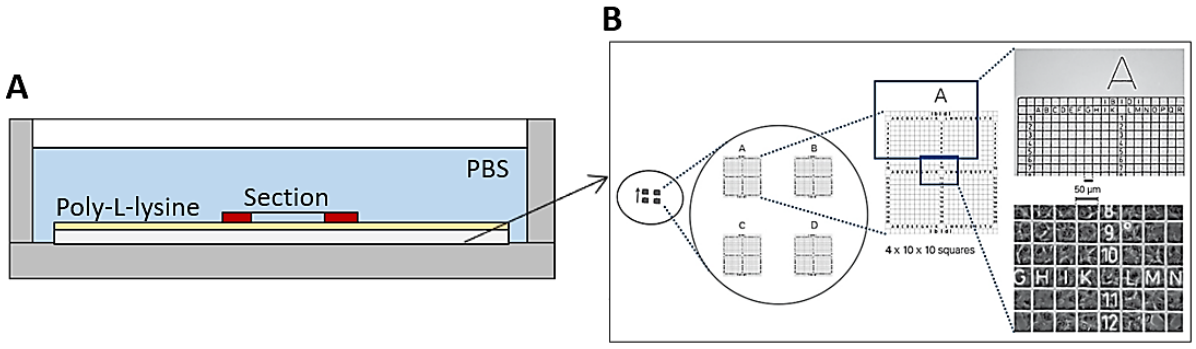

Figure 22 Details of the tissue substrate to enable mechanical testing and co-registration with collagen microstructure. (A) Sectional view of the testing substrate; grey: plastic petri dish, light grey: gridded coverslip, yellow: poly-L-lysine coating, red: tissue section, blue: PBS. (B) Detailed view of coverslip with 50µm imprinted grid.

Poly-L-lysine (PLL) is commonly used (**Table 5**) to fixate the tissue on a substrate and to prevent it from detaching while the indentation takes place in a liquid environment (Tracqui et al. 2011; Grant and Twigg 2013; Sicard, Fredenburgh, and Tschumperlin 2017). A thin coating of PLL charges positively the substrate which can help the negative charged extracellular fibrous proteins to adhere. The coating procedure was done according to routine methods. In brief, sterile coverslips were submerged in 0.1%w/v PLL solution (Sigma Aldrich, St. Louis, MO, USA), kept for 10 minutes and left to dry in a dust-free environment (culture hood) at room temperature. Once the coating had dried by visual inspection, they were stored in individual petri dishes with parafilm to protect from dust and particle contamination.

2.3. AFM protocol and optimisation

2.3.1. Probe selection

When selecting a probe, the stiffness of cantilever an important feature to optimise. For an optimal measurement, the cantilever should display a large amount of deflection, but at the same time a similar degree of sample indentation. This is achieved

by using cantilevers whose stiffness matches that of the probed sample as it is well-known in cell biomechanical studies (Gavara 2017). It was found (**Table 5**) that cantilever stiffness ranged from 0.15 to 0.6 N/m in previous studies on arterial tissue. Therefore, a probe with multiple cantilevers with stiffness ranging from 0.01 to 0.6N/m (MSNL-10, Bruker GmbH, Germany, **Figure 23)** was selected in order to facilitate the cantilever optimisation process. It was assumed that packaged probes were devoid of any contamination.

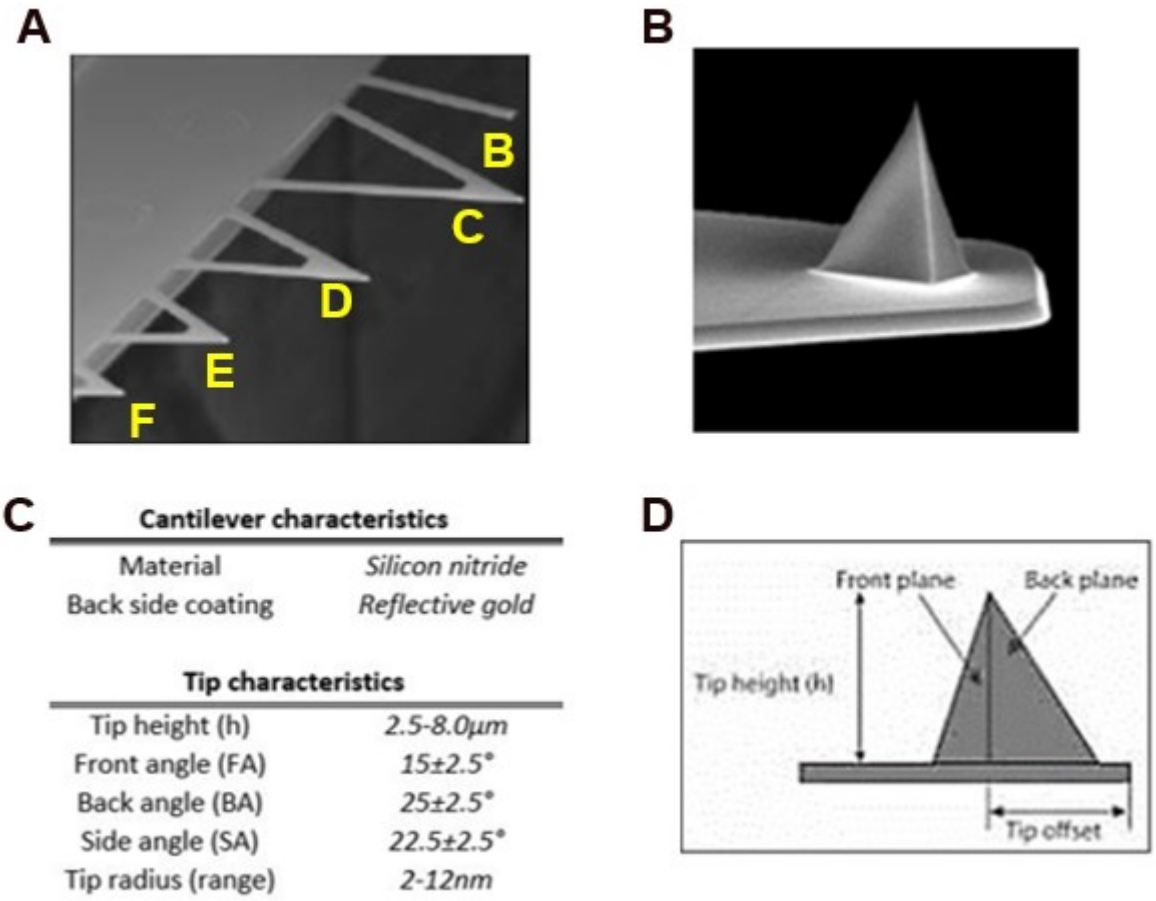

Figure 23 The Bruker MNSL-10 probe. (A) The cantilevers of the chip B(0.02N/m), C (0.01N/m), D(0.03N/m), E(0.1N/m), F(0.6N/m) (source: https://www.brukerafmprobes.com/p-3710-msnl-10.aspx). Cantilevers E and F were used in the optimisation process, (B) Scanning electron microscope picture of tip of each of the cantilevers (source: https://www.brukerafmprobes.com/p-3710-msnl-10.aspx), (C) Technical specifications of the cantilever E, (D) Diagram of the geometry of the tip with important dimensions noted.

2.3.2. Indentation conditions

Mechanical properties of fibrous proteins, and particularly collagen, are dependent on hydration conditions; dehydration increases the stiffness of extracellular matrix fibrous proteins as shown by many studies (Grant et al. 2008; Svensson et al. 2010; Segura et al. 2005). Throughout the experiments, the tissue sections were adequately hydrated with a physiological solution (Phosphate Buffered Saline, Sigma Aldrich, St. Louis, MO, USA), similar to the vast majority of studies listed in **Table 5**.

The temperature at which previous studies have probed their samples is varied among studies. In this work, the measurements were performed at room temperature assuming a uniform effect of temperature in the measured mechanical properties. A detailed investigation of the effect of temperature on the mechanical properties was out of the scope during the development of this protocol.

2.3.3. Determination of optimal Z-length

Z-length is a parameter that needs to be tuned according to the surface topography of the sample (Gavara 2017). Although the tissue is sectioned at 20μm thickness, the tissue surface presents with peaks and valleys, as elegantly demonstrated in a previous study of the aortic lamellar unit of media in pigs (Matsumoto et al. 2004). To optimise this parameter, height variations (difference of uppermost and lowermost point of contact) were derived from ten (10) indentation locations randomly spread around the media (**Figure 24**). In each location, 25 force curves were measured following a predefined square grid. Height differences had an average of $\bar{x}$=6.10μm and standard deviation of s=2.28μm. Therefore, assuming the variable follows a normal distribution, to capture 99.73% of height differences we would need a Z-length >= $\bar{x}$+3s = 12.96μm. An additional benefit of a high value of Z-length is that the tip is retracted so it is more likely to snap off contact in the retraction part.

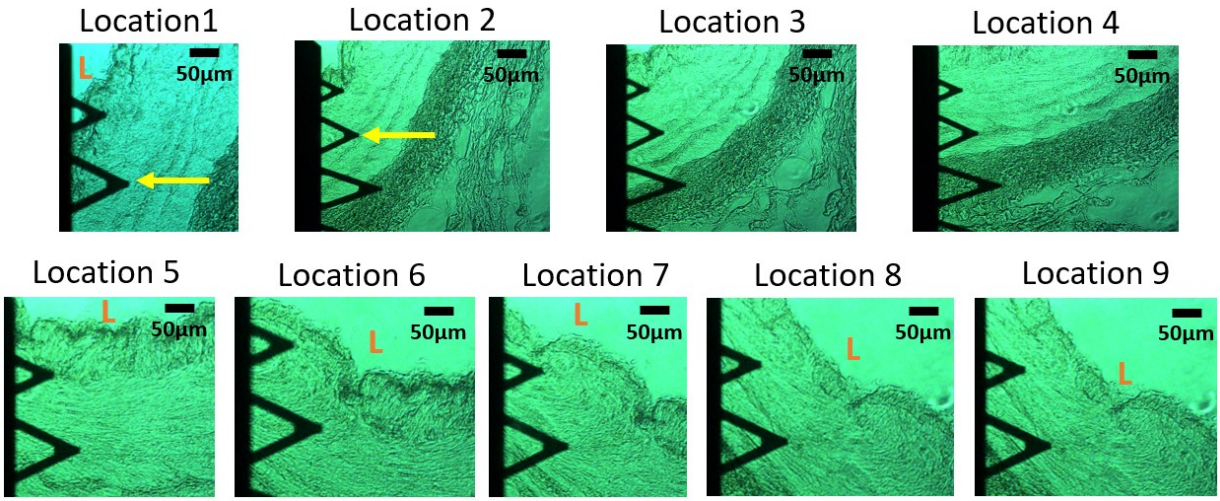

Figure 24 Topography experiment to determine optimal Z-length. Brightfield images of the selected indentation locations are shown. The cantilever in use is pointed with the yellow arrow. (L): lumen

2.3.4. Effect of time on structural integrity of tissue

Estimation of the minimum duration that the tissue can probed without loss of its structural integrity was important parameter. To achieve this, an experiment was designed according to which both the measurement area and the measurement settings (force threshold, indentation speed, Z-length, retract delay, approach threshold), remained constant so that biological and methodological variability were minimised. The tissue was probed six times within 90 minutes. Young's modulus and indentation depth were used to assess structural integrity. The Young's modulus was extracted by fitting a Hertzian contact model to the force curves using the JPK post processing software. After 60 minutes of the tissue probed with the same settings, a considerable increase in the indentation depth (**Figure 25**, top right) and a decrease in the Young's Modulus was noted (**Figure 25**, top left). The large variation of Young's Modulus values was a common encounter and they reflect biological variability given that the indentation location (25µm x 25µm, 25 indentation curves) was unchanged in between the six timepoints. Moreover, after 60 minutes the tissue might have started to degrade (as it was not fixed) which resulted in an increase of adhesive forces (**Figure 25**, bottom left) which complicated the measurement.

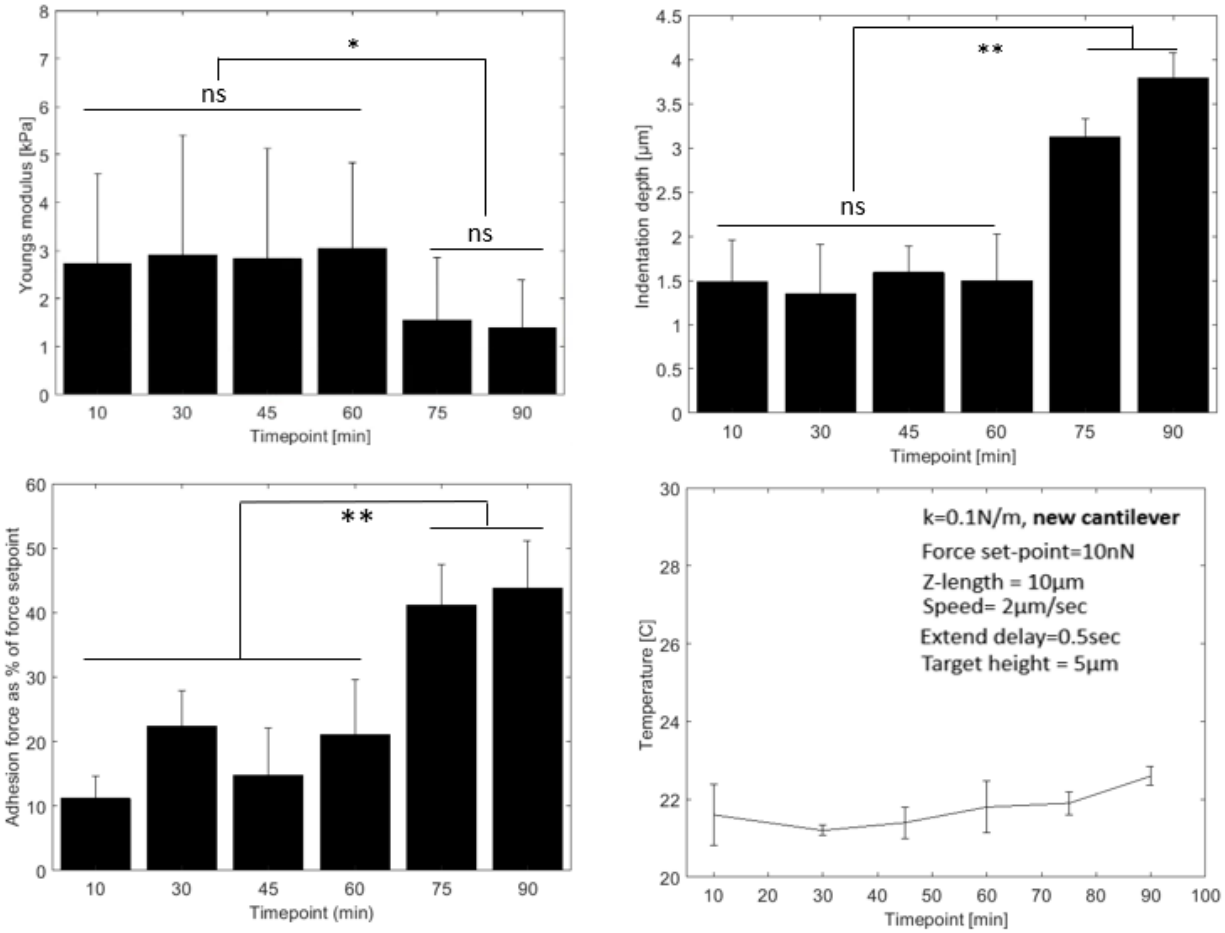

Figure 25 Effect of time on structural integrity of tissue assessed by Young's Modulus (top, left), indentation depth (top, right) and adhesion forces (bottom, left). The same indentation location consisting of a 50µmx50µm grid (25 force curves) was measured at 6 timepoints. Temperature (~ 22°C), scanning parameters and probe (legend) remained constant during the measurements. Bar heights and error bars represent average and standard deviation, respectively. Statistical comparisons were conducted with paired t-tests (*= p< 0.05, **: p<0.01, ***=p<0.001, n.s.: not significant)

2.3.5. Effect of indentation speed on adhesion force

As mentioned above the high adhesiveness of frozen unfixed tissue complicated the measurements. Another experiment was designed to investigate whether increasing the indentation speed would reduce the adhesion forces which in many cases degraded the entire force signal. **Figure 26** shows a surge of adhesion force by increasing the speed from 2 to 4µm/sec followed by a drop in the adhesion force at 6µm/sec. Increasing the indentation speed might introduce viscoelastic response of the tissue resulting in higher apparent stiffness. Being cautious about viscoelasticity we limited the indentation speed to 1-3µm/s (**Table 5**). The ramping of the speed was held constant among all experiments.

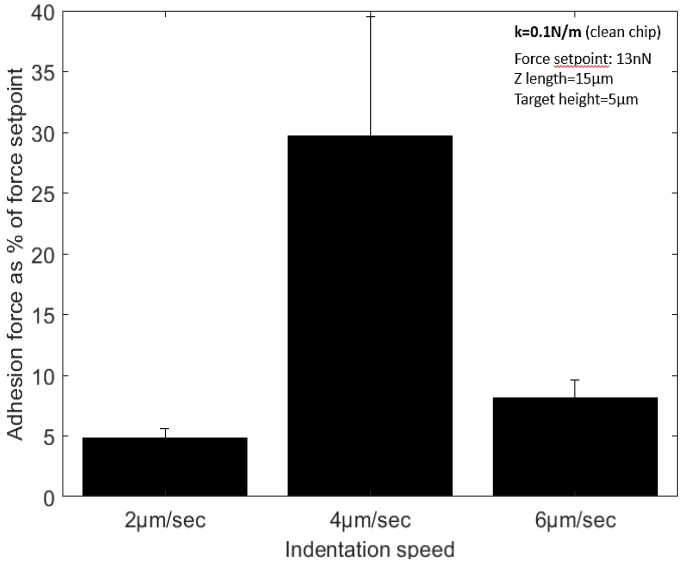

Figure 26 Effect of the indentation speed on adhesion force. For each case multiple locations were measured, and the results were pooled together: 2µm/sec - n=93 curves, 4µm/sec - n=137 curves, 6µm/sec n=98 curves. Bar heights and error bars represent average and standard deviation, respectively. All locations resided in the media layer.

2.3.6. Effect of the force threshold on the indentation depth

The relation between the force setpoint and indentation depth was experimentally investigated, although a linear relationship was expected to be observed. Initially, the rationale for this investigation was to record hyperelastic responses of the tissue which would be utilised for downstream material modelling. **Figure 27** shows that for the k=0.1N/m cantilever doubling the force threshold led to a marginal increase in the indentation depth. In fact, it was observed that the force indentation response reached a plateau. It was later found that the spring constant of this cantilever was too low that made it deform considerably up to the point where laser spot reflection on the photodiode detector was positioned outside the finite size, hence saturating the recording. It was therefore concluded that this cantilever was too soft to probe the tissue in the hyperelastic range (4-6µm). Switching to a stiffer cantilever (k=0.6N/m) overcame this issue (**Figure 27**).

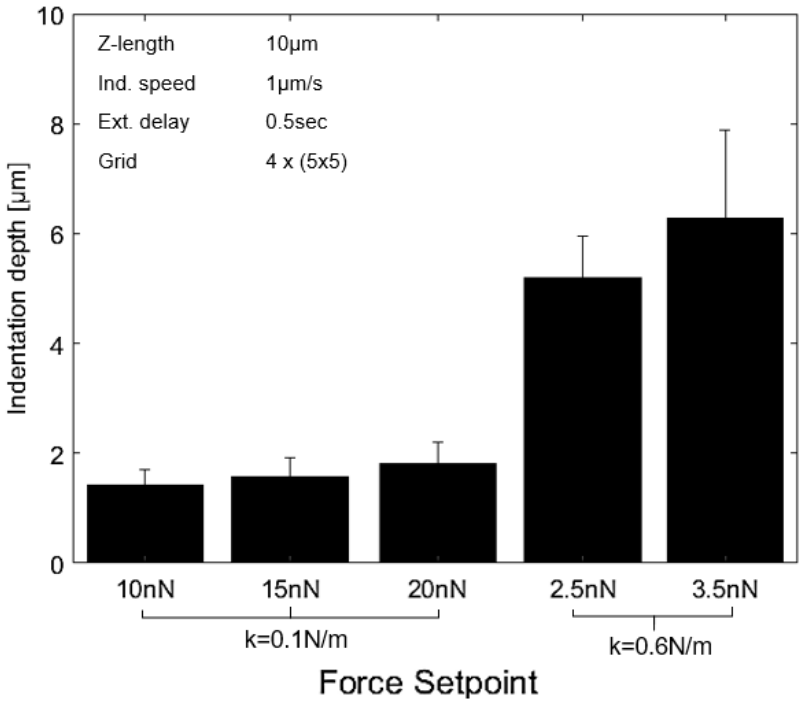

Figure 27 Effect of force setpoint/threshold on indentation depth. Bar heights and error bars represent average and standard deviation, respectively. All locations resided in the media layer.

2.3.7. Effect of optimal cutting temperature compound rinsing and tip contamination on adhesion forces

The presence of optimal cutting temperature compound around the cross section was found to dramatically increase the adhesion force and in turn the quality of the force displacement curves. Optimal cutting temperature compound is water-soluble; it is likely that it increased the viscosity of the immersion liquid (PBS). A small amount of PBS was used to dilute the optimal cutting temperature compound but care was taken not to shake the petri dish which could detach the tissue from the surface. The results of this experiment are summarised in **Figure 28** (cases A and B).

Indentation techniques require de-contamination of the probe after each indentation session. Working on tissue is more prone to adhesion from extracellular matrix build up on the tip; measurements in cells are advantageous in this regard due to a well-defined cellular membrane. After reviewing the relevant literature, it is noteworthy that almost all studies in **Table 5** avoid reporting adhesion forces and decontamination strategies. In this work, a contaminated probe resulted in significant increase of the adhesion between the tissue and the probe up to the point of complete disruption of the measurement (**Figure 28,** cases B and C).

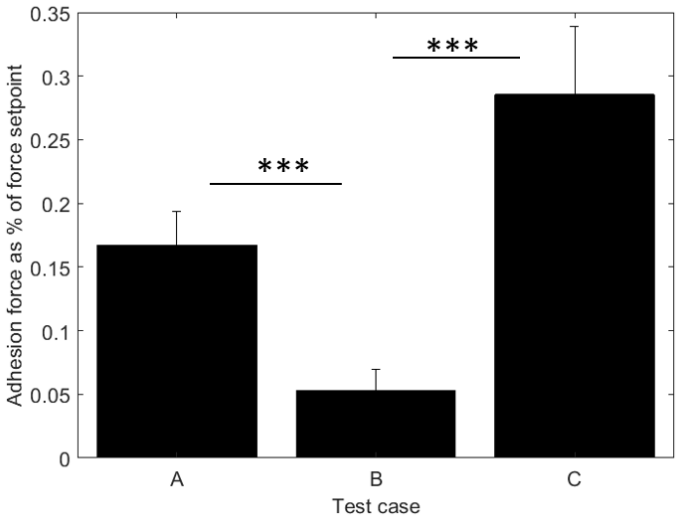

Figure 28 Effect of optimal cutting temperature compound rinsing and tip contamination on adhesion forces. All measurements took place in the medial layer with measurement parameters as shown (right). (A) Clean cantilever (from package) and no rinsing step (n=144 curves), (B) Clean cantilever (from package) with rinsing step (n=255 curves), (C) second scan with cantilever from (B) with optimal cutting temperature compound rinsed but not cleaned. The probe was not previously de-contaminated (n=245 curves) Bar heights and error bars represent average and standard deviation, respectively. All locations resided in the media layer. Comparisons with paired t-test (*= p< 0.05, **: p<0.01, n.s.: not significant.

2.3.8. Probe decontamination

Mechanical testing by indentation is a very delicate technique and probes can be easily contaminated by extracellular matrix residue. Probe contamination can influence the quality of the mechanical measurements in both direct and indirect ways. For example, residue can sit on the tip and if left uncleaned it can harden and form a tip on the tip.

There are many methods to decontaminate indentation probes; some are very harsh (such as plasma treatment) others are very mild, such as cleansing with absolute ethanol. Herein, extracellular matrix residue was enzymatically digested by submerging the probes in 3mg/ml collagenase type I solution that was prepared according to manufacturer's information data sheet. In brief, lyophilised collagenase powder type I (Clostridium Histolyticum, Sigma-Aldrich, St. Louis, MO, USA) was reconstituted in Hank's Balanced Salt solution (Sigma Aldrich, St. Louis, MO, USA) at 4°C and individually stored in aliquots at -2°C to prevent repetitive freeze-thaw cycles which are known to decrease enzyme effectiveness. Upon submersion of probes in collagenase solution they were kept at a temperature of 37.2 C for optimal enzymatic activity.

2.3.9. Extraction of mechanical properties from force curves

Material testing by indentation testing is a more delicate technique than tensile testing. The force signal can easily be distorted by many factors. For example, debris can disrupt the laser signal by passing behind the cantilever, the tip can be contaminated quite easily increasing adherence to sample and obstructing smooth disengagement of the tip during retraction. Potential detachment of tissue section and spontaneous air nucleation in the vicinity of the measurement can introduce considerable noise to the measurement or completely disrupt the measurement.

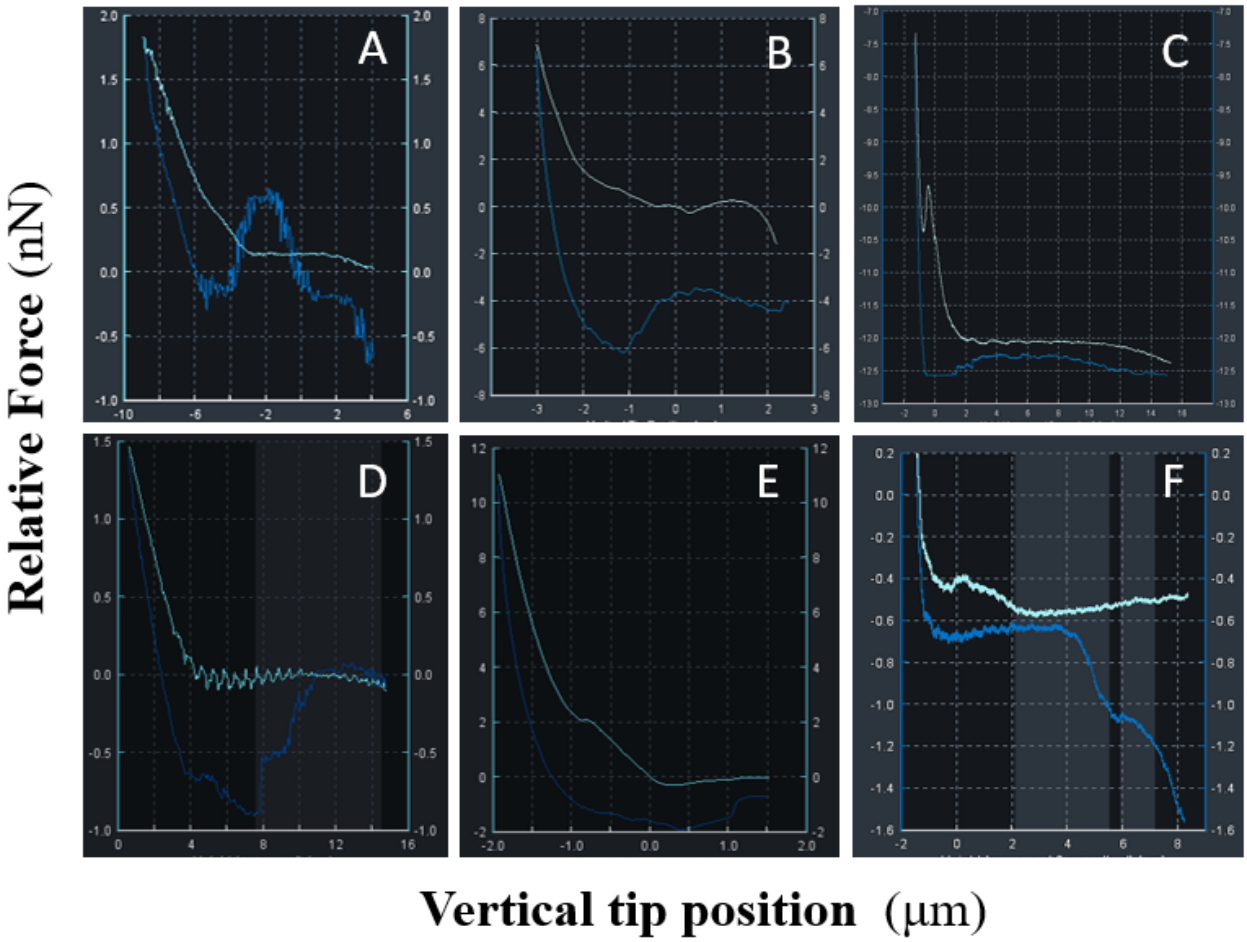

Figure 29 (A-F) Examples of force curves which were excluded from downstream analyses. For all graphs, X axis: Vertical tip position, Y axis: Relative Force, Light blue: extension curve, Dark blue: retraction curve.

Therefore, prior to using the force curves for downstream extraction of mechanical properties a list of criteria had to be decided to ensure reliable results. **Figure 29** shows some characteristic examples of force curves which were excluded from downstream

analysis after applying the following criteria. First, force curves should have clearly defined extension and retraction parts. Second, start of extension part should be flat (after baseline correction). Third, to ensure the tip has disengaged in successive measurements, the start of extension and end of adhesion curves should coincide. Fourth, the tip should snap off contact around the region of the contact point (**Figure 29A, E**). Fifth, force curves should have a clearly defined contact point signifying smooth engagement of the tip (**Figure 29 D, F**). Sixth, the force signal should be concave and non- decreasing (**Figure 29B**). Seventh, the force signal should not have abrupt, step changes (drops or surges) at the region of contact point. Finally, there should be no sign of material yield (abrupt drop and subsequent increase of signal, **Figure 29C**) during the indentation.

The curves that passed the quality control criteria were imported to JPKSPM Data Processing (v6.1) software (**Figure 30**), where a custom-made subroutine had been built from a list of standard curve processing operations. The parameters of the subroutine were kept consistent for all curves. Each force curve was smoothed with gaussian filter (**Figure 31**), corrected for baseline tilt (**Figure 32**), and other indentation quantities were retrieved such as location of contact point (**Figure 33**), indentation depth (**Figure 34**).

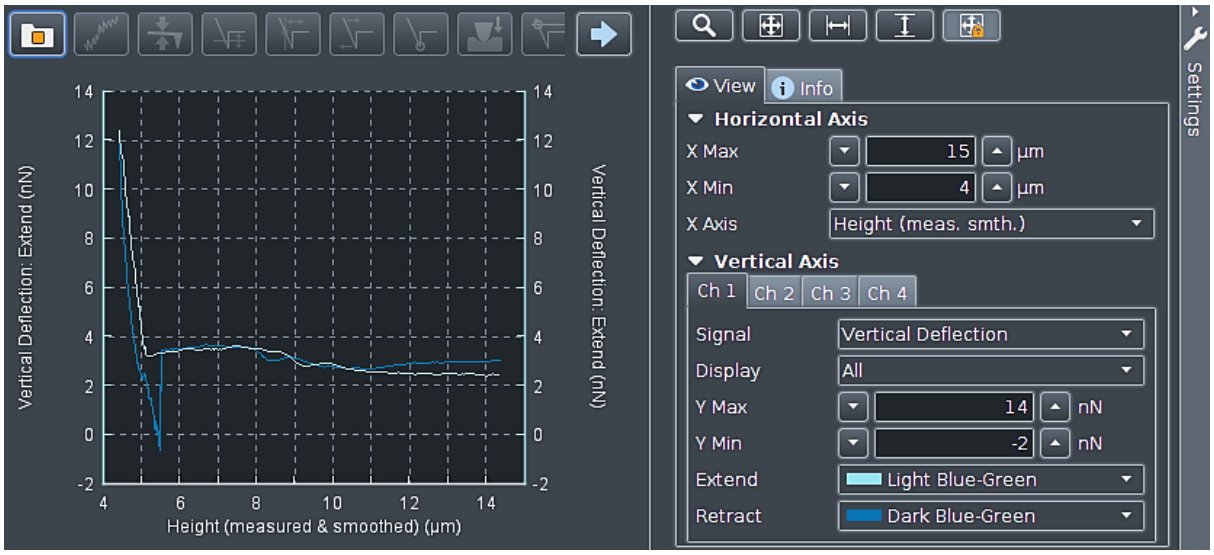

Figure 30 (left) Raw force-displacement curve (or force curve) imported to JPKSPM Data Processing software. Y axis: Vertical deflection/ Force (nN), X axis: Height (µm). Light blue: extension, Dark blue: retraction. (top left) List of standard operations each denoted by a square. (right) Viewing parameters.

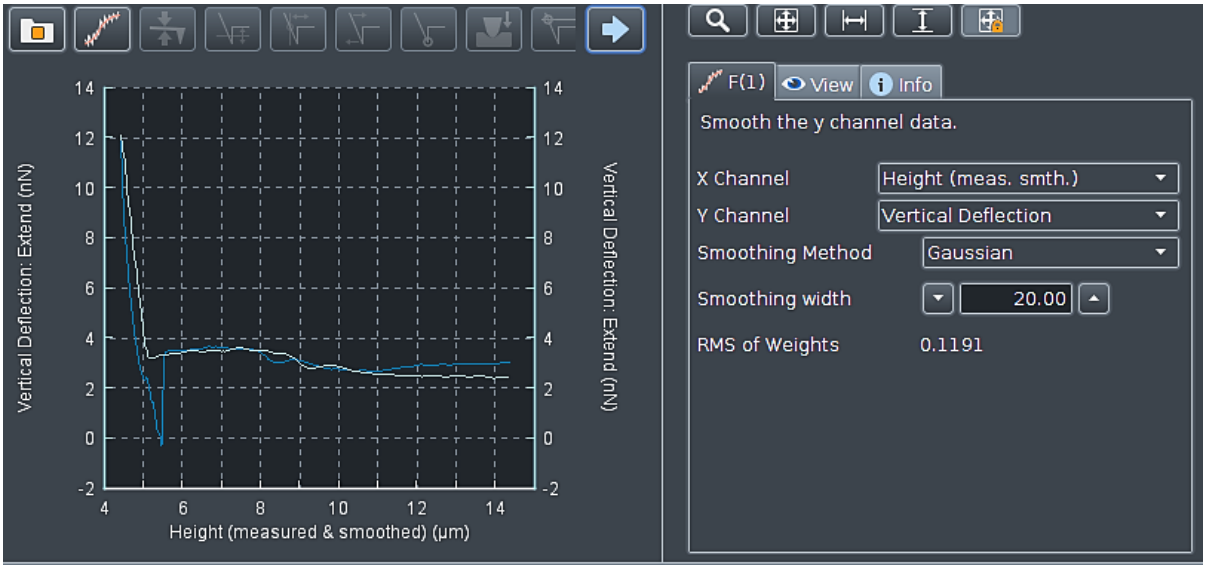

Figure 31 (left) Operation 1: Smoothing of raw curve. Y axis: Vertical deflection/ Force (nN), X axis: Height (µm). Light blue: extension, Dark blue: retraction. (right) The smoothing parameters remained constant across all force curves.

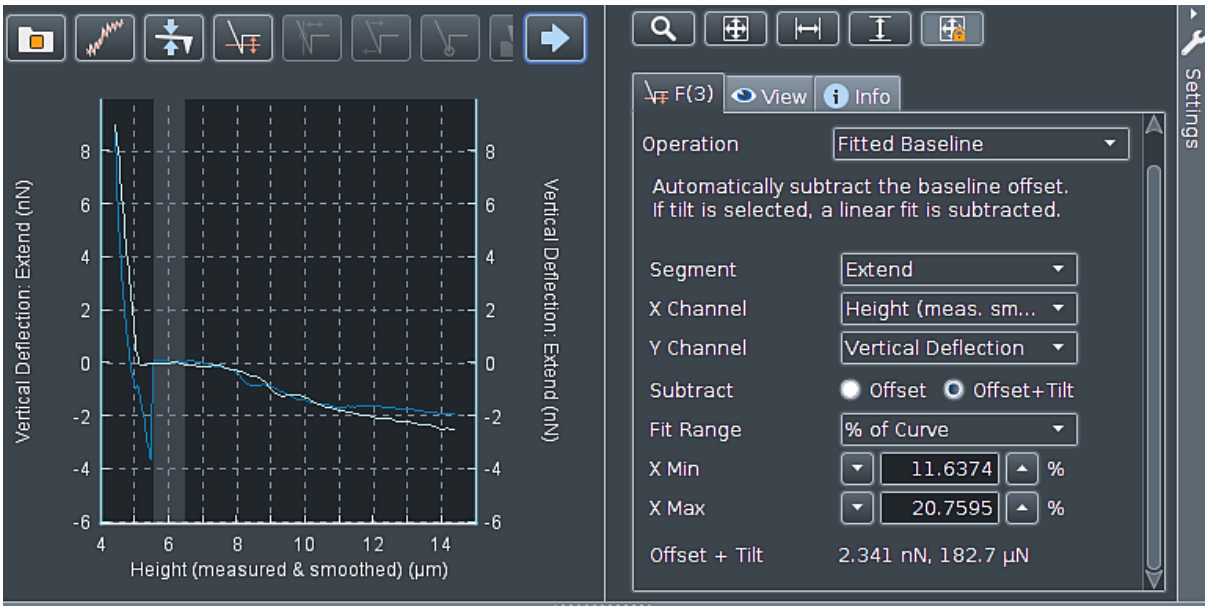

Figure 32 Operation 3: Correction of offset and tilt of baseline part of extension curve. As the force is always relative to a baseline, this baseline is subtracted from the entire curve. Please notice the difference in the numbering of the Y axis. Light blue curve: extension, dark blue curve: retraction. **(right)** Correction parameters.

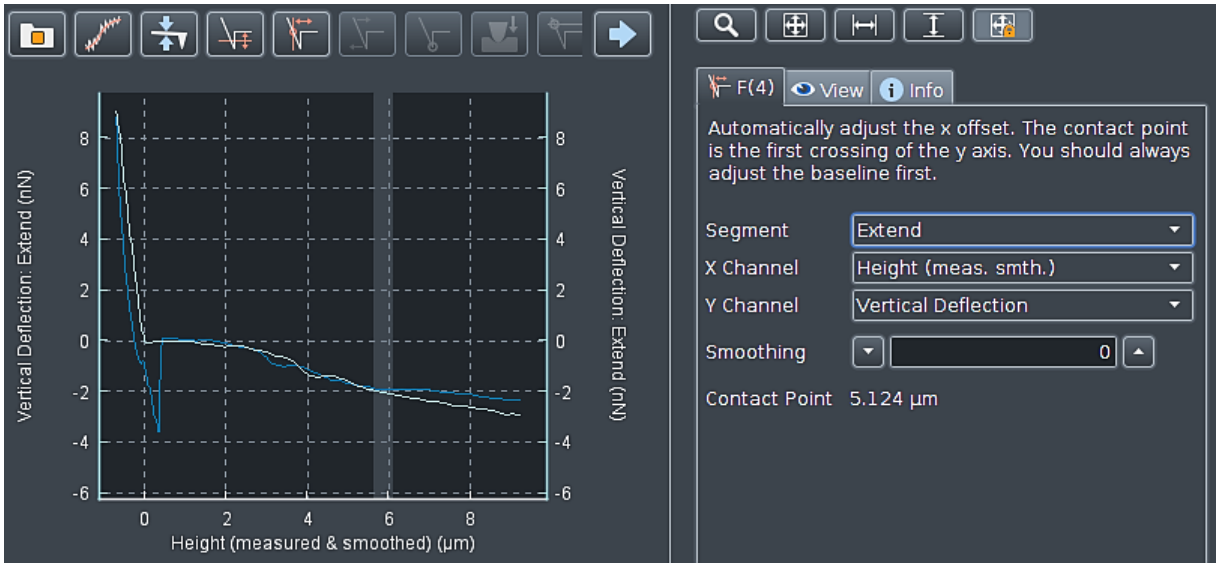

Figure 33 Operation 4: Location of contact point. Please notice the change of X axis numbering. The zero point is where the contact point is estimated to be. Light blue curve: extension, dark blue curve: retraction.

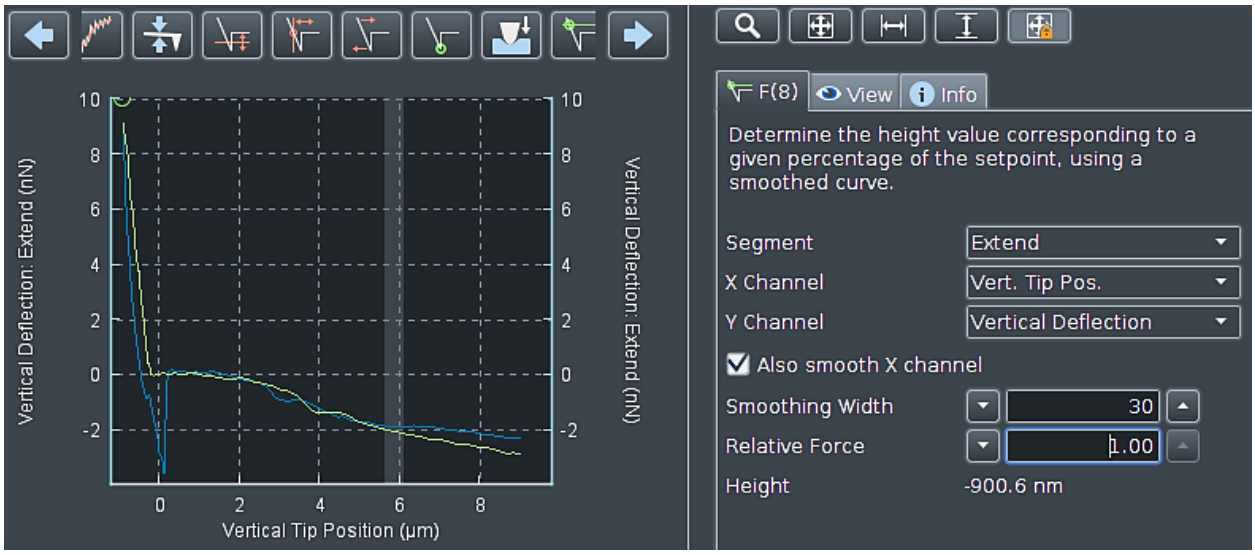

Figure 34 Operation 8: Extraction of indentation depth (denoted as *Height* at 100% *Relative Force,* **down right**). Light blue curve: extension, dark blue curve: retraction.

Young's Modulus (E) was extracted by fitting a contact model to the force curves (**Figure 35**) taking into account geometrical and mechanical constants (half opening angle of pyramidal tip α=28 degrees, Poisson's ratio v=0.5). Assuming no adhesion and friction forces, when a sample is probed with a pyramidal tip the force increases parabolically with respect to the indentation depth (δ) (Bilodeau 1992).

$$F = \frac{2}{\pi}\frac{E}{1-\nu^2}\tan(a)\,\delta^2 \qquad \text{(Eq. 1)}$$

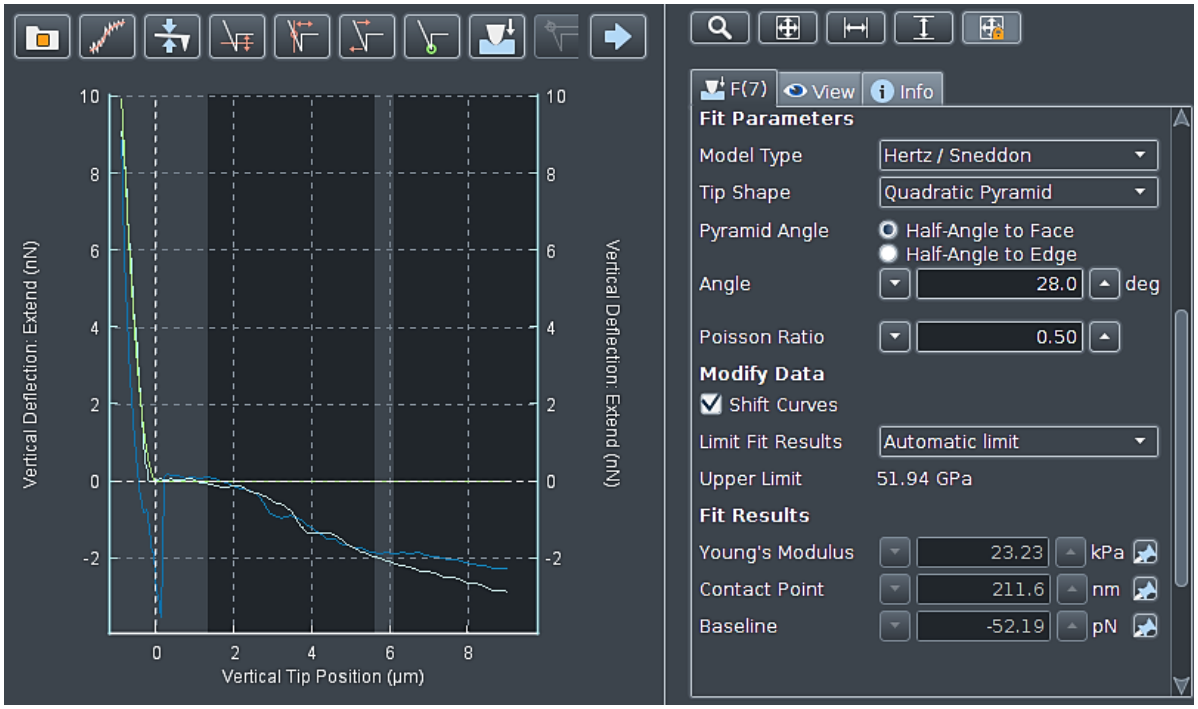

Figure 35 Fitting of Hertzian contact model (light green curve) to the extension part of the force curve. Light blue curve: extension, dark blue curve: retraction

The first 10% of the indentation depth was fitted with the contact model. For the purpose of extracting local material stiffness with contact model the tissue was assumed to be isotropic and homogeneous in the vicinity of the indentation (5µm x µm). The extraction of Young's Modulus was done without reference to the outputs of the postprocessing software. The root mean square (RMS) of the force residuals was used to assess the goodness of fit (**Figure 35**).

2.4. Error in estimation of Young's Modulus from indentation experiments

If small deformations/strains (≤ 10%) are applied to the sample and the cantilever, then the cantilever is in the linear regime i.e. the voltage difference on the photodiode (ΔV) is proportional to the vertical deflection (Δz) of the cantilever. The cantilever deflects when it indents the sample therefore the voltage difference will be proportional to the indentation depth (δ)

$$F = k_c k_s \, \Delta V \approx k_c \delta \qquad \text{(Eq. 2)}$$

where k_c: spring constant of the cantilever (nN/nm)

k_s: deflection sensitivity of the cantilever(nm/Volts)

For Hertzian contact, the indentation depth (d) is related to the force on the cantilever (F) with the equation:

$$F = \frac{2}{\pi}\frac{E}{1-\nu^2}\tan(a)\,\delta^2 \qquad \text{(Eq. 3)}$$

where, F: force on cantilever (N),

E: Young's Modulus (Pa),

v: Poisson's ratio=0.5 for incompressible tissue,

δ: indentation depth (m),

α: half side angle of the tip: 28 degrees

Substituting F from (eq.2) to (eq.1) and rearranging the equation in terms of Young's Modulus, yields:

$$E(k_c, \delta) = \frac{\pi}{2}\frac{1-\nu^2}{\tan(a)}k_c\delta^{-1} \qquad \text{(Eq. 4)}$$

According to the error propagation theory, the error, $\boldsymbol{\delta E_{YM}}$, in the estimation of Young's Modulus will be:

$$\delta E_{YM} = \sqrt{\left(\frac{\partial E}{\partial k_c}\delta k_c\right)^2 + \left(\frac{\partial E}{\partial d}\delta d\right)^2} \quad \text{(Eq. 5)}$$

$$\delta E_{YE} \approx \frac{\pi}{2}\frac{(1-\nu^2)}{\tan(a)}\left[\frac{\delta k_s}{|k_s|} + \frac{\delta d}{|d|}\right] \quad \text{(Eq. 6)}$$

The error can be approximated in the following way:

$$\delta E_{YE} \approx \frac{\pi}{2}\frac{(1-\nu^2)}{\tan(a)}\left[\frac{\delta k_s}{|k_s|}\right] \quad \text{(Eq. 7)}$$

We found fluctuations of 0.02N/m around an average value of 0.54N/m (the nominal stiffness for this cantilever is 0.60N/m) which corresponds to an error of 2.61%.

Collectively, we obtain an error:

$$\delta E_{YE} \approx 2.96\%$$

In this analysis we focused only on the methodological variability of the measurement system, therefore we excluded the indentation depth which contains combined information about the biological and methodological variability. One way to uncouple these would be to perform measurements on a sample of known properties (e.g. a hydrogel) and follow the above methodology.

2.5. Discussion

In this subchapter, the steps taken to develop a protocol to measure nanomechanical properties with Atomic Force Microscopy in frozen coronary artery tissue sections were presented. It became quite clear from the start of the development of this protocol that it would not be possible to derive one set of parameters which would work in any sample. Rather, these experiments gave insight on the effect of several indentation parameters and on the shape and quality of the raw force curves that were used as guidelines for future experiments.

The thickness of sections used in the literature for mechanical testing displayed a large range from 8µm to 200mm. For thin sections (<10µm) and cell applications, it is advisable that elastic properties should be corrected when samples are probed more than 10% of their thickness to avoid substrate effects (Dimitriadis et al. 2002; Gavara and Chadwick 2013). None of the reviewed studies (**Table 5**) has done this correction - except for Sicard, Fredenburgh, and Tschumperlin (2017) - perhaps because this correction may be more suited to cell applications since the combination of a well-defined border with incompressible cellular contents may lead to an apparent increase of stiffness. Interestingly, Sicard, Fredenburgh, and Tschumperlin (2017) reported the elastic modulus of human pulmonary arteries measured from 10, 20 and 50 µm thick sections. They found that the difference between the Young's Modulus for the 50 µm thick sections and for 20 µm thick sections was statistically insignificant. By contrast, the Young's Modulus values from 10 µm thick sections were the significantly greater than the 50 and 20µm thick sections. Therefore, it was deemed adequate that a tissue thickness of 20 µm would be thick enough to avoid substrate effects in this study. It should be noted, however, that one can get substrate effects when probing less than 10% for certain types of biological tissue, such as contact lenses (Selby, Maldonado-Codina, and Derby 2014). It is probable that this thickness is tissue-specific and an investigation to determine the optimal thickness that does not compromise the stiffness measurements was out of scope of this protocol.

One of the most challenging aspects in the process of refinement of the indentation protocol was to reduce the magnitude of the adhesion forces which in many cases completely disrupted the signal. Tip contamination was conducive to increased adhesion levels which deteriorated the signal to noise ratio by unsuccessful and rough

engagement and disengagement of the tip. Although the adhesion curves are not usually utilized for mechanical studies their utility was paramount to verify the location of the contact point of the force curve. It was surprising that there was no mention of adhesion forces in all previous studies (**Table 5**). Moreover, in previous studies there was no particular mention on probe decontamination strategies which can deteriorate force recordings.

In this work, a Hertzian contact model was used to estimate Young's Modulus from force curves. However, there are other contact models which could have been implemented instead, given the considerable magnitude of the adhesion forces witnessed during the indentation experiments. To incorporate the effect of adhesion in Hertzian contact Johnson, Kendall, and Roberts (1971) formulated the JKR theory of adhesive contact using a balance between the stored elastic energy and the loss in surface energy. The JKR model considers the effect of contact pressure and adhesion only inside the area of contact. The Derjaguin-Muller-Toporov (DMT) model (Derjaguin, Muller, and Toporov 1975) is an alternative model for adhesive contact which assumes that the contact profile remains the same as in Hertzian contact but with additional attractive interactions outside the area of contact. Ultimately, the Hertzian contact model was selected in order to accelerate the optimisation process of the nano-indentation protocol because of its simplicity. However, there are certainly limitations to that approach and due to high adhesion, the JKR model would have been more suitable to extract Young's Modulus from the force curves.

3. Visualisation and quantification of collagen microstructure in frozen tissue sections

3.1. Picrosirius red staining

This stain is particularly specific to collagen when combined with polarised light illumination (Junqueira, Bignolas, and Brentani 1979). In preparation for the staining, the tissue was left to air dry for 45 minutes to 1 hour under the hood right after mechanical testing. The tissue was first fixed in a paraformaldehyde solution (4%,

diluted in Phosphate Buffered Saline) for 10 minutes to preserve structural integrity and then washed gently three times in PBS. A 0.2mg/ml phosphomolybdic acid solution was prepared from powder (Thermo Fisher Scientific GmbH, Germany) and used to incubate the tissue for 5 minutes. Before rinsing the phosphomolybdic acid in distilled water, the tissue was visually inspected under a microscope to verify the coloration of smooth muscle with yellow colour.

After the first incubation in PMA, the tissue was submerged in picrosirius red solution (Abcam, Cambridge, MA, USA) for 60 minutes. Following the incubation, the tissue was rinsed with 2 changes of acetic acid solution (0.5%) made by diluting glacial acetic acid (Sigma Aldrich, St. Louis, MO, USA) in distilled water. This step was very important to remove excess colour from the tissue. The duration ranged from 3 to 6 minutes. The process was closely monitored by looking the tissue through the microscope. At the end of the washing step the tissue was rinsed in three changes of 100% ethanol (ethanol absolute 99.8%, Sigma Aldrich, St. Louis, MO, USA) to remove water followed by a final rinse in xylene (Xylene 100% histological grade, Sigma Aldrich, St. Louis, MO, USA) before was mounted (DPX mountant, Sigma Aldrich, St. Louis, MO, USA) on a glass slide and left to solidify overnight.

3.2.Imaging, Acquisition and Digitisation

Stained cross sections were imaged in an automated manner (Zeiss AxioObserver Z1, TissueFAX Slide Scanner) with brightfield and polarised light (dark field) at 10X and 20X magnification. The microscope supported raster scanning of the slides and subsequent focal volume tiling post-acquisition. White balance was applied before brightfield image acquisition. For polarised light imaging, a polarising filter was used (quarter wavelength plate, ZEISS, Germany) and the orientation of the filter was "crossed" to achieve a dark background. The filter rejects most incident light; therefore, exposure time and lamp intensity were optimised at 750ms and lamp intensity at 7V. Identical illumination, acquisition settings were applied to all stained sections.

3.3. Metrics of Collagen Microstructure and co-registration

It is believed that stain colour do not relate specifically to collagen type, rather to fibre thickness as discussed extensively in the relevant literature (Dayan et al. 1989;

Montes and Junqueira 1991; Drifka et al. 2016, Rittie 2017). A measure of the total (all types) collagen density was extracted by converting the polarised light image (RGB image) to grayscale.

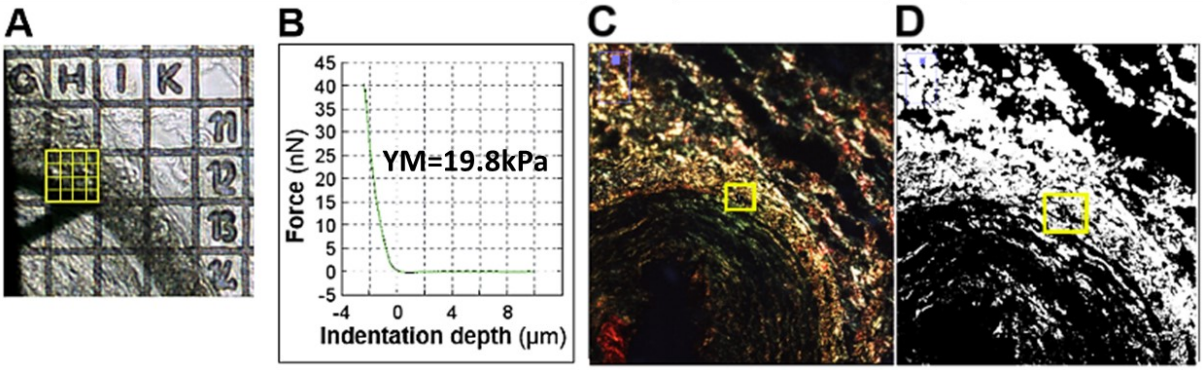

Figure 36 Co-registration pipeline of AFM-derived mechanical properties with local collagen microstructure. The tissue section was laid on a coverslip with an imprinted square grid (size=50µm) that facilitated the co-registration process. The indentation locations (e.g. square H12, image A) were selected on the basis of presumed collagen fibre density (dark bands) from bright-field images. (A) Brightfield image of the cantilever (triangular shape) with the measurement grid (yellow) before an indentation on square H12. (B) Force curve (black line) in 1 of the 25 locations of the measurement grid and contact model fit (YM=19.8kPa, RMS=26nN) is shown in green. The median value from 25 force curves was assigned as the representative stiffness of the square H12. (C) Stained tissue Picrosirius Red under polarised light. (D) Binary image after thresholding the grey scale equivalent image of (C) and derivation of collagen area density (=62%). The median value of Young's Modulus (H12) was co-registered with one value of collagen area density.

Darkfield polarised light images were subjected to an identical threshold level (level:75/255). The threshold level was selected by validating the collagen content of the adventitial layer (a layer known for being rich in collagen) against measurements of collagen content from porcine coronary arteries derived with second harmonic generation microscopy (Chen and Kassab 2016). The collagen content of porcine coronaries was reported to be 28-33% for the adventitia. Multiple square ROIs (50µm x 50µm) residing within the adventitial layer were selected and the collagen area density was derived for multiple threshold levels (50, 75, 100, 125). The average collagen area density was then derived from ten (10) regions for those four threshold levels. The threshold level which resulted in an average collagen area density in the region of 28-33% was selected.

The brightfield image with the grid in focus was stacked with the polarised light image (identical pixel size) so that a square area of interest within the brightfield image can be transferred across to the polarised light image (**Figure 36**). By this technique it

was possible to locate the grid location in the polarised image. Collagen fibre density was calculated as the percentage of white pixels within a ROI.

3.4.Co-registration error analysis

The co-registration error has three components:

- Tissue shrinkage error: This error was assumed to be zero by coating the coverslip with an adhesive solution (poly-L-lysine).
- One component comes from the error to optically match the measurement grid (50x50) with the real square dimensions imprinted on the coverslip (50μm x 50μm) due to the finite resolution of the microscope objective. One can obtain an estimate of this error (E1) by dividing the resolution (Δr) of the objective used (10x/0.25, λ=0.55μm for brightfield settings) with a characteristic dimension of the square size (in this case the square size will be used).

  The planar resolution of a microscope objective can be calculated with the following formula,

$$\Delta r = 0.61 * \frac{\lambda}{NA} \quad \text{(Eq. 8)}$$

  where, NA, is the numerical aperture of the objective lens and, λ, is the wavelength.

  Which leads us to the estimation of E1:

$$E_1 = \frac{\Delta r_{AFM}}{ROI\ dimension} = \frac{1.34\mu m}{50\mu m} = 2.68\%$$

- A second component comes from the error to optically match the local collagen microstructure to the real square dimensions imprinted on the coverslip (50x50). One can obtain an estimate of this error (E2) in the same way for an 20x/0.5 microscope objective.

$$E_2 = \frac{0.67\ \mu m}{50\ \mu m} = 1.34\%$$

The total co-registration error is:

$$E_{CR} = E1 + E2 = 4.02\%$$

4. Statistical methods

A Young's Modulus value was extracted from each force curve. For the purposes of the optimisation of the AFM protocol, indentation output quantities (Young's Modulus, indentation depth, adhesion force) were reported as mean and standard deviations. Comparisons between groups were conducted with paired t-tests and a p-value of less than 0.05 was considered statistically significant. Matlab 2020b (Natick, Massachusetts) was used for statistical analyses.

Chapter 3: Effect of collagen microstructure on the local mechanical properties of healthy coronary arteries measured with Atomic Force Microscopy

1. Introduction

The composition and structure of coronary arteries determines their mechanical properties which are necessary for physiological function. Fibrillar collagen is primary biomechanical constituent of blood vessels which endows them with anisotropic (direction-dependent) strength (Rhodin 1980). At least nineteen different types of collagen comprise the collagen family (Fratzl 2008; Ricard-Blum 2011) but only types fibrillar types-I, III, IV and V are mostly found in blood vessels (Shekhonin et al. 1987; Rekhter 1999). There is a non-uniform distribution of collagen across the three layers of the arterial wall in terms of density as well as orientation/alignment. Collagen types I and III are present in the intima (Von Der Mark 1981). In the media collagen is intertwined around elastin sheets (Dingemans et al. 2000; Connell et al. 2008). The adventitia is rich in collagen types I and III (Holzapfel and Ogden 2010). Proteoglycans are thought to play a dissipative role in viscoelastic response of blood vessels (Fomovsky, Thomopoulos, and Holmes 2010). Mechanical properties of collagen (~1 GPa) are 1000 times stronger than elastin (~1 MPa) (Gosline et al. 2002; Wenger et al. 2007).

At any time, the net collagen content is the result of production and degradation. Particularly in coronary artery disease this biochemical equilibrium is usually disturbed towards both ways. The first occurs in the early stages of advanced atherosclerotic plaque formation when SMCs migrate into the intima and synthesise collagen to prevent the lipid core of the plaque – a mixture of oxidised cholesterol esters, lipid-laden immune cells and cellular debris - from getting in contact with the bloodstream (Falk 2006). In another case, in acute coronary syndromes, collagen equilibrium is shifted towards degradation due to macrophages secretion of matrix degrading enzymes by macrophages the within the fibrous cap thereby increasing the plaques vulnerability to rupture leading to myocardial infarction (Lee et al. 1996; Libby 2012). As a result, collagen is believed to plays a central role to atherosclerotic plaque stability.

Biomechanical modelling of coronary arteries with advanced computational methods, such as Finite Element Analysis (FEA), can be a useful tool towards understanding the biomechanical environment of coronary arteries in health and disease (Saez, Pena, and Martinez 2014; Delfino et al. 1997; Ohayon et al. 2005). Selection of appropriate material properties is a cornerstone of such approaches. Currently, there is a lack of data regarding material properties of coronary arteries due to limited tissue availability. Macroscopic testing (tensile/compressive) dominate the entire landscape of material characterisation methods for coronary arteries. Although they capture quite well the strain-stiffening (hyperelastic) aspect of arterial tissue, they may be too coarse to enable tissue mechanics to be traced back to local composition and structure. They also require the tissue specimen to be of sufficient size as well as rigid enough to undergo arterial clamping. Alternative characterisation techniques for coronary arteries can be tested on porcine models (Al-Mashhadi et al. 2013; Pedrigi et al. 2015) which have been shown to possess many features of human histology.

One of those techniques is Atomic Force Microscopy, an *ex vivo* modality that measures local material properties by indentation. Detailed methods such as this could help to develop biologically inspired constitutive models for biomechanical modelling. So far, this technique has seen widespread use in mechanical characterisation of cells and tissues in normalcy and disease (Stylianou et al. 2019; Krieg et al. 2019), other than arteries where literature is scant (**Table 6**). Indentation offers great advantages compared to macro-mechanical testing as it does not rely on tissue size and properties and, by working on tissue sections, adjacent sections can be stained with routine histology methods enabling co-registration of tissue mechanics to local composition and structure.

So far, only one other study (Rezvani-Sharif, Tafazzoli-Shadpour, and Avolio 2019b) has studied the mechanical properties of healthy coronary arteries at such high-detail level. All previous studies **(Table 6)** have been conducted on aortas and carotid arteries due to the fact that they are more easily obtainable.

In this study it was hypothesised that the mechanical properties of coronary arteries are dependent on local collagen microstructure. To test this hypothesis, we firstly performed indentation measurements from which we extracted the local stiffness. Then we stained the very same tissue with a collagen-specific stain in order to relate the

local material properties to the local collagen content. By using a substrate with an imprinted grid, we managed to improve on the limitations of previous studies in which co-registration was rather coarse (**Table 6**).

Table 6 List of micro- and nano-indentation studies on **non-diseased** frozen arteries with special focus on tissue preparation practice, and co-registration strategy of mechanics to histology.

Study	Tissue type and preparation	Reported stiffness	Co-registration with histology	Limitations
Hemmasizadeh et al. (2015)	Species: porcine Vessel: aorta Thickness: 8-10 μm Hydration: none Temperature: not reported	Inner half (media): 60.21±2.61 kPa Outer half (media): 69.06±1.88 kPa N=611 force curves	Yes - with Fourier Transform Infrared Spectroscopy	Resolution: 25 μm
Grant and Twigg (2013)	Species: porcine Vessel: aorta Thickness: 12 μm Hydration: ultrapure water Temperature: 37°C	Frequency distribution of stiffness from N=9216 force curves, Median:~30 kPa Range: 1-500 kPa	No	-
Beenakker et al. (2012)	Species: porcine Vessel: aorta Thickness: 8 μm Hydration: PBS Temperature: 37°C	Frequency distribution of N=2000 force curves, Median:~10 MPa Range:100 kPa-1 GPa	Coarse co-registration of stiffness histograms with enzyme treatments (collagenase, elastase and hyaluronase)	-
Akhtar et al. (2009)	Species: ferret Vessel: aorta & vena cava Thickness: 5μm Hydration: none Temperature: not reported	Aorta: 5-38 MPa Vena cava: 20 MPa N=120 force curves	Yes – with stained adjacent section for H&E	Visual co-registration
Matsumoto et al. (2004)	Species: porcine Vessel: pulmonary artery Thickness: 150μm Hydration: PBS Temperature: not reported	Media: 50-180 kPa N=2500 force curves	Yes, but not shown	-
Oie et al. (2009)	Species: porcine Vessel: carotid artery Thickness: 1 mm Hydration: gauze patch soaked in normal saline Temperature: 36°C	Media: 29.2 ± 2.8 kPa N=3600 force curves	Yes – with stained adjacent section for collagen (Masson's Trichrome)	Co registration hard to evaluate because of high power image only. Lack of spatial reference and specified area where the co-registration took place for collagen-rich regions
Chang et al. (2018a)	Species: human Vessel: internal mammary artery Thickness: 5 μm Hydration: none Temperature: 21°C	Adventitia: Low PWV group: 2159.3 ± 282.5 MPa High PWV group: 2895 ± 414.4 MPa PWV: pulse wave velocity	Yes, indirectly – with PWV	n/a
Chang et al. (2018b)	Species: human Vessel: internal mammary artery Thickness: 5 μm Hydration: hydrated & dehydrated cases Temperature: 21°C	Hydrated media (n=147,456 force curves): Low PWV group: 250.5 ± 39.1 kPa High PWV group: 721.7 ± 291.9 kPa Dehydrated media (n=65,536 force curves): Low PWV group: 2116.2 ± 523.1 MPa High PWV group: 3163.6 ± 548.7 MPa	Yes, indirectly – with PWV	n/a

2. Methods

2.1. Nano-indentation testing

Non-atherosclerotic coronary artery tissue was taken from a porcine model of coronary atherosclerosis (Chapter 2, Section 1). Porcine left anterior descending (LAD) arteries were cryo-sectioned at 20μm thickness and laid on glass coverslips with an imprinted 50μm spaced grid (Ibidi GmbH, Martinsried, Germany) according to protocol (Chapter 2, Section 2.2.1,). The angle of the blade was adjusted so that sectioning plane is perpendicular to longitudinal axis of native vessel. Tissue sections were preserved in dry ice awaiting reconstitution with physiological saline (Phosphate Buffered Saline, Thermo Fisher Scientific GmbH) and subsequent mechanical testing.

A JPK NanoWizard 4 (JPK instruments, Germany) machine was used for the experiments. Tissue sections were indented with a MNSL-10 probe (Bruker, Germany). Cantilever stiffness (k=0.6N/m, nominal) and deflection sensitivity were calibrated with the thermal noise method (Butt and Jaschke 1995). To minimise laser misalignment, the probe was submerged for 30 minutes in PBS and set to equilibrate to a controlled temperature of 23°C. The indentation was applied in the longitudinal direction of the native vessel. The force setpoint was optimised so that indentation depth does not exceed 10% of the tissue thickness (linear regime). Signal to noise ratio often drops due to probe contamination with extracellular matrix (ECM) residue. Collagenase (type I from Clostridium Histolyticum, Sigma Aldrich, St. Louis, MO, USA) buffered in Hank's Balanced Salt solution (Sigma Aldrich, St. Louis, MO, USA) was used to decontaminate the probes at a concentration of 3mg/ml and at 37.0°C for optimal enzymatic activity (for more details please refer to Chapter 2, Section 2.2.1).

Measurements were performed over 50μm x 50μm square regions of interest (ROIs) in a grid-like fashion. Multiple 50μm x 50μm square ROIs (4 to 5 per section) were probed, all residing within the media and intima layers. The intima and the media are known to be the prime bearers of mechanical loading in physiological vascular tone (Rhodin 1980). Structures that appeared to be circumferentially-orientated, slender and dark-coloured – on the basis of brightfield images - were presumed to be associated with collagen dense regions and therefore were targeted (**Figure 37 A & B**). Within each ROI, the probe executed force indentations with 10μm step size, resulting in 25 indentations

(force curves) per ROI. Before each scan, the measurement grid (**Figure 37 B**, yellow) was optically overlaid on the brightfield (grayscale) image (Olympus PlanFL, 10x, 0.35, air). This built-in feature facilitated the accurate superposition of the measurement grid onto the grid imprinted on the coverslips.

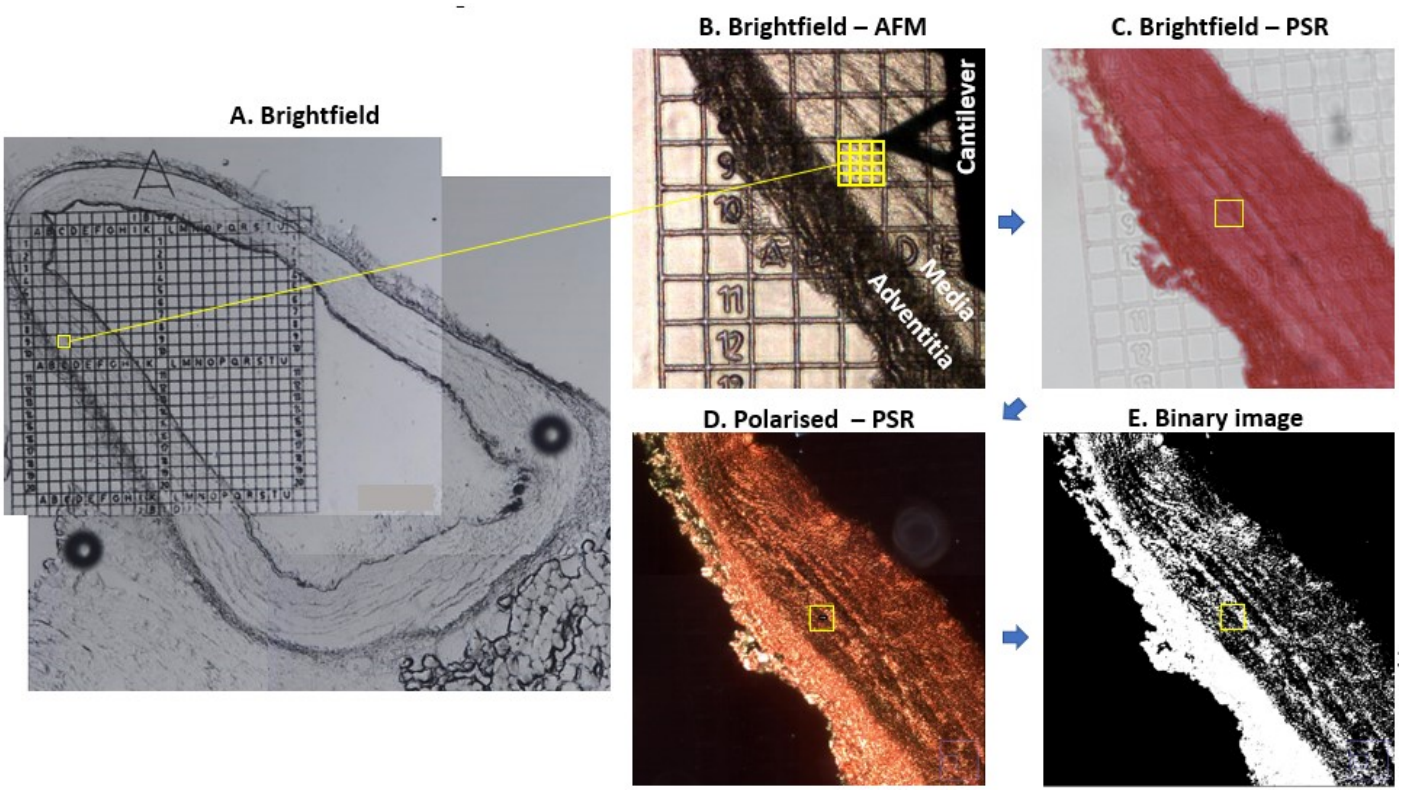

Figure 37 Co-registration approach from tissue mechanics to histology. (A) Brightfield image of a representative section from a healthy coronary artery (higher power images were combined to form a low power image). The square grid (square unit: 50μm x 50μm) imprinted on the coverslip where tissue was laid on enabled co-registration of tissue properties and histological metrics with high accuracy. (B) Brightfield image of the cantilever (triangular shape) and the tissue with the measurement grid. Twenty five (n=25) force curves were acquired within each ROI (e.g. C9). The collagen content of the targeted areas was measured post-hoc by staining with Picrosirius Red. (C, D) Stained tissue with Picrosirius Red under (C) brightfield and (D) polarised light with the ROI shown in yellow. (E) The polarised light colour image was converted to grayscale and it was thresholded to produce a binary image. ROI dimensions: 50μm x 50μm.

2.2. Extraction of Young's Modulus from force curves

In the linear deflection regime (where the indentation depth does not exceed 5-10% of sample thickness) the voltage difference recorded on the photodiode (ΔV, [Volts]) is proportional to the cantilever deflection (Butt, Cappella, and Kappl 2005) (δ,

[m]). The latter is related to the recorded force (F, [N]) by taking into account the cantilever spring constant (k_C, [N/m]) and the deflection sensitivity (k_S, [m/Volts]), as we have seen in equation 2:

$$F = k_c \cdot k_s \cdot \Delta V \approx k_c \cdot \delta \quad \text{(Eq. 2)}$$

The force-displacement maps (consisting of 25 force curves) were imported to JPKSPM Data Processing (v6.1) software, where a custom-made subroutine was created from a deck of standard curve processing operations. The parameters of the subroutine were kept consistent for all curves. Each force curve was corrected for baseline tilt, smoothed with gaussian filter and other indentation quantities were retrieved, such as location of contact point, indentation depth (δ), adhesion force, work of adhesion. The indentation depth (δ) was derived calculating the bending of the cantilever ($z-z_c$) which was then subtracted from the downward movement of the cantilever ($d-d_{eff}$) according to the relation:

$$\delta = z - z_c - (d - d_{eff}) \quad \text{(Eq. 9)}$$

A linear measure of stiffness (Young's Modulus) was also extracted by fitting a Hertzian contact mechanics model to the force curves and taking into account geometrical and mechanical constants (half opening angle of pyramidal tip α=22.5, Poisson's ratio ν=0.5). Assuming no adhesion and friction forces, when a sample is probed with a pyramidal tip the force increases parabolically with respect to the indentation depth (Sneddon 1965; Bilodeau 1992) according to equation 1.

$$F = \frac{2}{\pi} \frac{E}{1-\nu^2} \tan(a)\, \delta^2 \quad \text{(Eq. 1)}$$

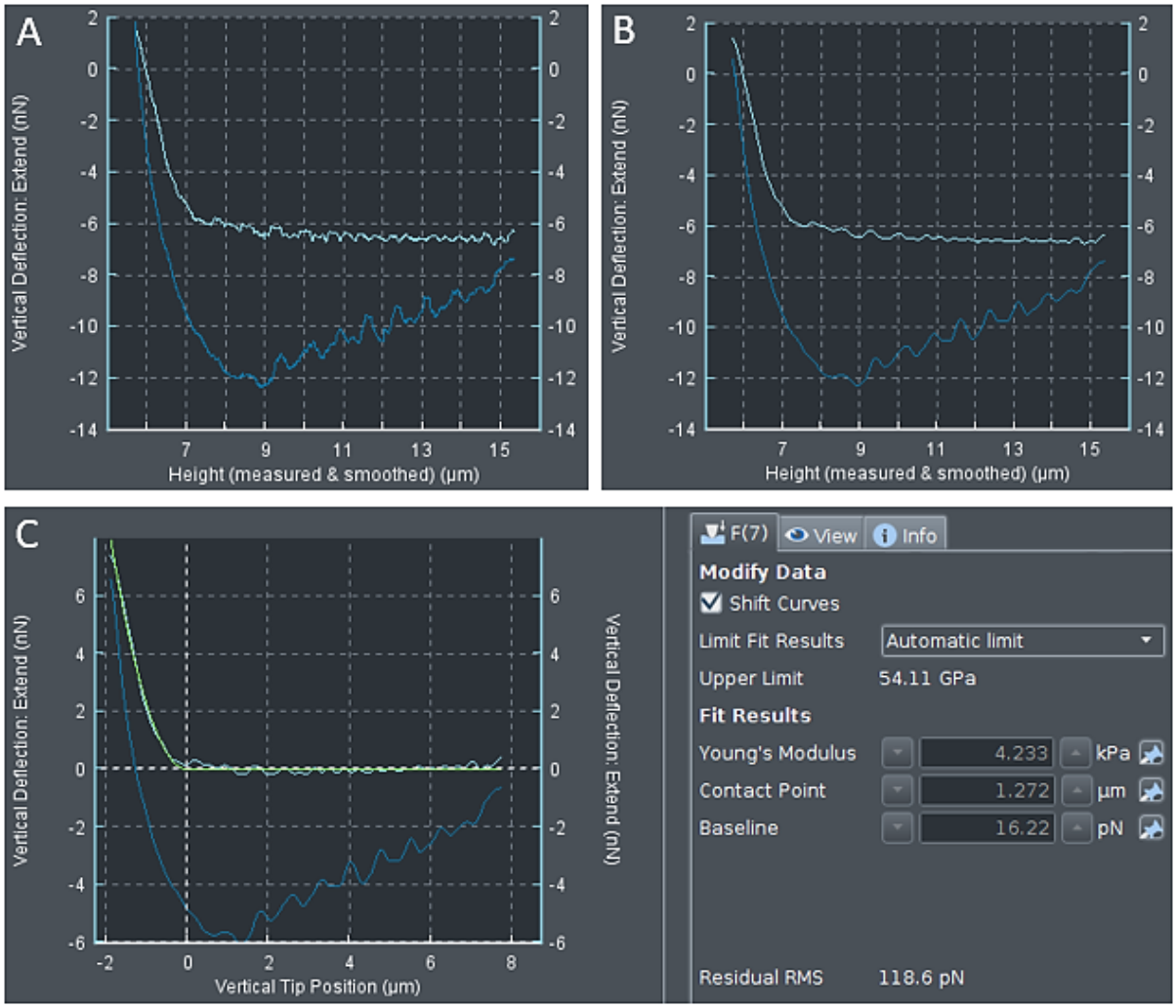

Figure 38 Analysis of raw force curves. (A) Raw force curve signal, dark blue: extension, light blue: retraction, (B) Smoothed force curve, (C) Extraction of Young's Modulus by fitting a Hertzian contact model on the force curve (light green line). The contact point is defined where vertical tip position is zero. This force curve yields a modulus value of 4.2 kPa and root mean square of force residuals (Residual RMS) is 118.6 pN.

The first 10% of the indentation depth was fitted with the contact model. Although for the purpose of estimating stiffness with contact model the tissue was assumed to be isotropic and homogeneous in the vicinity of the indentation (10µm x 10µm). The extraction of Young's Modulus was done without reference to the outputs of the post-processing software. The root mean square (RMS) of the force residuals was used to assess the goodness of fit (**Figure 38**). Raw force curves were rejected from fitting process according to the criteria: contact point not clearly defined, sign of material yield, low signal to noise ratio (RMS>200nN), evident contamination of probe. The probes were regularly decontaminated from extracellular matrix residue by submerging them in a 3 mg/ml collagenase solution at 37.0°C for 1 hour.

2.3. Collagen staining, imaging and digitisation

After mechanical testing, the tissue was stained with picrosirius red according to routine histological protocols. In brief, tissue sections were air dried for 30 minutes at room temperature, then fixed in 4% paraformaldehyde (Thermo Fisher Scientific GmbH) solution buffered in PBS. After three washes in PBS, the tissue was incubated for 5 minutes at room temperature in 0.2% (w/v) solution of phosphomolybdic acid hydrate (Sigma-Aldrich, St. Louis, MO, USA) reconstituted in distilled water. The tissue was then rinsed once with distilled water and submerged in picric acid solution (Abcam, Cambridge, MA, USA) for 1 hour at room temperature. Excess colour was removed by washing them with 0.4% solution of glacial acetic acid (Sigma-Aldrich, St. Louis, MO, USA) in distilled water. The tissue was then dehydrated in three rinses with absolute ethanol (Sigma-Aldrich, St. Louis, MO, USA). After one dip in xylene the tissue was mounted on a standard glass microscope slide with DPX mountant (Sigma-Aldrich, St. Louis, MO, USA) and left overnight under a hood to fully solidify.

The sections were analysed using an inverted light microscope Zeiss AxioObserver (Jena, Germany) equipped with a built-in automated acquisition system (TissueFAX i Plus, TissueGnostics GmbH, Austria). Acquisition was done with a 20x microscope objective (Zeiss EC Plan-Neofluar 20x/0.5). The microscope had built-in capacity for linearly polarised light imaging. Before each acquisition, the polarisers were "crossed" to achieve a black background. Image acquisition took place under identical illumination conditions. The images were stored in a high-resolution format (.tiff) and were imported in Fiji v1.53c (NIH, USA) to extract histological metrics of collagen microstructure, such as collagen fibre density.

2.4. Extraction of metrics of collagen microstructure and co-registration with AFM measurements

A measure of the total (all types) collagen density was extracted by converting the polarised light image (RGB image, **Figure 37D**) to grayscale. Grayscale images were subjected to an identical threshold level (level:75/255) that resulted in binary images (**Figure 37E**) from which collagen density was derived as the percentage of white pixels within a ROI. The threshold level was selected by validating the collagen content of the

adventitial layer against measurements of collagen content from porcine coronary arteries derived with second harmonic generation microscopy(Huan Chen and Kassab 2016). Due to the fact that the grid was not always visible in the dark-field image under polarised light (**Figure 37D**), the brightfield, stained image – where the grid was visible (**Figure 37C**) – was used as an intermediate image between the former and the AFM brightfield image(**Figure 37B**) to enable the accurate co-registration of mechanical properties and histological metrics.

2.5. Statistical analysis

Each indentation location consisted of 25 force curves. A Young's Modulus value was extracted from each force curve. The median of the 25 values was assigned as a representative stiffness value of the indentation location/ROI. The Young's Modulus of each indentation location was paired with one value of collagen fibre density.

A power calculation was done to estimate the number of sections needed to perform measurements in order to observe a statistically significant difference between the healthy and diseased groups. To compute the sample size several quantities need to be derived first. We estimated the Young's Modulus of healthy coronary arteries as μ_1 = 23.60 kPa (**Table 7**, Autumn 2020, arithmetic mean). Based on Rezvan et al. human coronary plaque has a value of μ_2 = 11.47 kPa (arithmetic mean). Therefore, the magnitude difference (μ_1- μ_2) is equal to 12.13 kPa. We also estimated the total variability (σ^2) by adding the measurement variability (n=100 repeated measures in single location; 3.4 kPa^2) and biological variability (inter-ROI variability; 258.6 kPa^2). For power of β=95% and significance level α=1%, we calculated the number of ROIs (N) that need to populate each of the control and diseased groups based on the formula below. We adjusted the result for a discard rate of 5% (**Table 7**, Autumn 2020) to N=68 ROIs. Given that - for each tissue section - five ROIs are measured on average, this resulted in n=14 sections for each group.

$$N = 2 \cdot \sigma^2 \cdot \frac{\left(Z_{\frac{\alpha}{2}} + Z_{\beta}\right)^2}{(\mu_1 - \mu_2)^2} \quad \text{(Eq. 10)}$$

Young's Modulus was found to follow a log-normal distribution (Kolmogorov-Smirnov test, p=0.045). Collagen fibre density was not found to follow a log-normal distribution (Kolmogorov-Smirnov test, p=0.2754). The log-normalised pairs of Young's Modulus and collagen fibre density were categorised into bins according to the following procedure. First, the collagen fibre density data were sorted from lowest to highest re-arranging the Young's Modulus values. A bin size of six data points was defined. Then for every six values of the collagen fibre density or Young's Modulus data, the median value was calculated and replaced the former six values creating new pairs. Comparisons were made using Wilcoxon signed-rank tests and a p-value of less than 0.05 was considered statistically significant. Matlab 2020b (Natick, Massachusetts) was used for statistical analyses.

3. Results

Fourteen (n=14) tissue sections from left anterior descending arteries of three animals were analysed with the above pipeline. Sixty-seven (n=67) indentation locations within the media and intimal layers, such as C9 (**Figure 37B**), were measured resulting in 1379 force curves. There was an average discard rate of 18% on the grounds of low signal to noise ratio, high adhesion which interfered with smooth engagement and disengagement of the tip thus difficulty in determining the contact point; 20-30% discard rate has been reported as acceptable in previous nano-indentation studies (Gavara and Chadwick 2013; Gavara 2017). The Young's Modulus of each ROI was estimated as the median value of the Young's Moduli of the force curves (n=25) that resided in that ROI (**Figure 37B**). The Young's Modulus of each indentation location was paired with one value of collagen fibre density resulting in n=67 co-registered data points (**Figure 39** & **Figure 40**).

Table 7 Protocol optimisation rounds and comparison with literature values. Median value of Young's Modulus at each optimisation round was calculated from all measurements in healthy coronary arteries, IQR: interquartile range, CV: coefficient of variation, N: number of force curves. Literature value corresponds to nano-indentation measurements in healthy human coronary media from Rezvani-Sharif, Tafazzoli-Shadpour, and Avolio (2019b).

	Young's Modulus (kPa)				
	Median	**IQR**	**CV**	**N**	**Discard Rate**
Autumn 2019	28.3	31.7	112%	515	32%
Spring 2020	24.6	16.6	68%	480	23%
Summer 2020	10.8	6.8	63%	549	29%
Autumn 2020	13.5	11.0	81%	1850	5%
Spring 2021	11.0	8.6	78%	1379	18%
	Average	**Standard deviation**			
Literature value	10.7	3.3	31%	600	n/a

In order to investigate potential correlations, the Young's Moduli values were plotted in four quartiles of collagen density (**Figure 39**). Although particular care was taken to reduce sampling bias by targeting regions in a random fashion, some subliminal bias (uneven sampling of groups) remained.

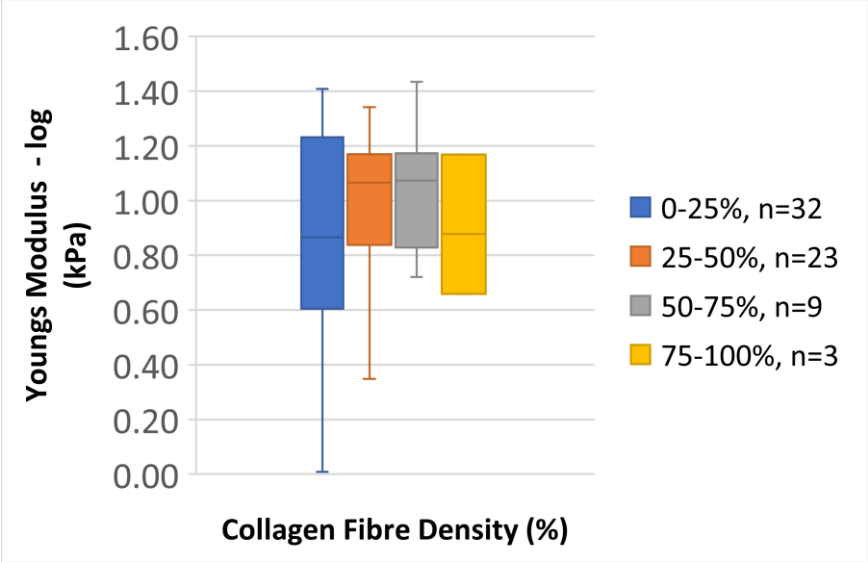

Figure 39 Box and whisker plot of co-registered Young's Modulus values (n=67) stratified in four quartiles of collagen fibre density. Measurements conducted in media-intima layers. Lower whisker: first quartile, middle line: median, upper whisker: third quartile. No statistically significant differences were found between groups.

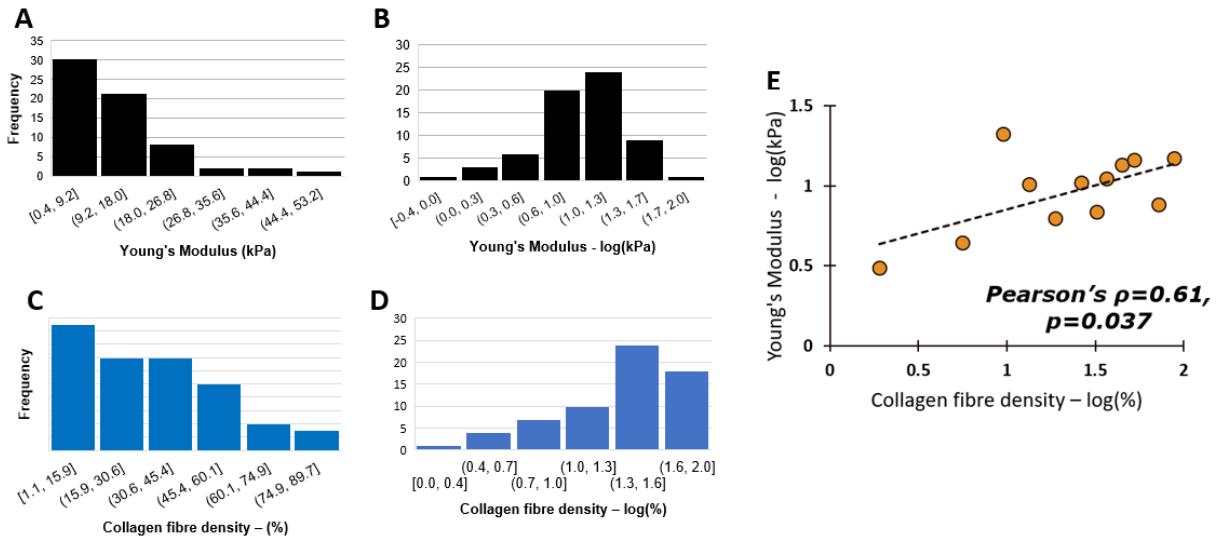

Figure 40 Frequency distribution of Young's modulus (A, B) and collagen fibre density values (C, D). Young's Modulus was found to follow a log-normal distribution, whereas collagen fibre density did not. (E) Scatter plot between log-normilised Young's Modulus and collagen fibre density for healthy group (14 tissue sections, n=67 co-registered data points). The co-registered datapoints were binned to 12 groups of 6 data points each. A significant positive correlation (Pearson's ρ=0.61, p=0.037) was found to relate the variables.

4. Discussion

Collagen is a key biomechanical constituent of coronary arteries conferring them anisotropic strength. Tensile methods have been the conventional modality for capturing the macroscopic hyperelastic behaviour of healthy coronary arteries (Wang et al. 2006; Holzapfel et al. 2005). However such material testing methods are agnostic to microscale variations of tissue stiffness that can be a source of stress concentrations – a proposed mechanism for plaque rupture (Leach et al. 2010; Brown et al. 2016) – particularly when assessing plaque mechanics.

In the current study we have developed, optimised, and implemented Atomic Force Microscopy - a high resolution mechanical testing technique - to measure the mechanical properties of healthy porcine coronary arteries. We first developed a robust method for measuring mechanical properties of coronary artery tissue sections. To demonstrate the robustness of the measurement protocol we did three things. First, we calculated the measurement error (3.35%, more details on Chapter 2, Section 2.5) associated with estimation of Young's Modulus from indentation tests. Secondly, we calculated the methodological variability (repeatability) of our measurement system by conducting repeated measures (n=5 repeats, n=25 force curves per repeat) in the same

location - we found 3.39 kPa[2]. Thirdly, we created a table (**Table 7**) to demonstrate how our initial estimations of coronary media stiffness (**Table 7,** Autumn 2019) gradually decreased from round to round and dropped almost identical to the literature value from Rezvani-Sharif, Tafazzoli-Shadpour, and Avolio (2019b) in the last optimisation round (**Table 7,** Spring 2021). As a result, our measurement protocol is reproducible and repeatable.

Then, we established and proposed a co-registration framework to enable the investigation of the relationship between collagen fibre density and local mechanical properties. By using the same tissue section for mechanical testing and staining as well as by using gridded coverslips, we minimised co-registration errors of tissue mechanics to histology in comparison with similar studies in the literature (**Table 6**). We estimated the total co-registration error as 4.02% (more details on Chapter 2, Section 3.4).

Finally, we investigated the degree to which collagen content affects the mechanical properties of healthy coronary arteries. Indentation measurements were collected from the intima and medial layers due their biomechanical significance at physiological conditions. To quantify local collagen content, we stained the tissue sections with Picrosirius Red – a stain known for its affinity to collagen – and we extracted collagen fibre density for locations where indentations had taken place as an estimate of the local collagen content (**Figure 37**). We observed a moderate correlation (Pearson's ρ=0.61, p=0.037) between collagen density and Young's Modulus (**Figure 40E**).

4.1. Comparison with other indentation studies.

Previous indentation studies on animal arterial tissue (**Table 6**) have attempted to relate local arterial tissue stiffness to underlying composition, primarily fibre content (collagen and elastin). In one study (Oie et al. 2009), force displacement measurements were conducted in two regions within the medial layer of one porcine carotid artery section while adjacent section was stained with Elastica van Gieson (for elastin) and Masson's Trichrome (for collagen). They reported overall average Young's Moduli of 22.8 ± 10.9 kPa (media), 17 ± 9 kPa (collagen-rich area in media) and 50.8 ± 13.8 kPa (internal elastic lamina). Despite the high detail of the measurements, the co-registration strategy is not explicitly outlined, particularly where the co-registrations took place. In addition,

the methodology of deriving the histological metrics is not explicitly outlined. In another study (Beenakker et al. 2012), aortic tissue sections were subjected to tissue-degrading treatments (collagenase, elastase and hyaluronidase) the material properties of the remaining tissue scaffolds were measured. Rather than averaged values of tissue stiffness for each of the three cases, they demonstrated frequency histograms of Young's Modulus from N=2000 measurements for each treatment case. Young's Moduli values displayed a range of four orders of magnitude in logarithmic scale (from 10 kPa to 10 MPa) in all cases. It is noteworthy that the stiffness distributions of tissue sections treated with elastase were shifted towards lower values compared to their collagenase counterparts. A third study (Hemmasizadeh et al. 2015) applied a spectroscopy method (Fourier Transform Imaging Spectroscopy) to quantify layer-wise variations in protein content, structural (collagen and elastin) protein and total protein in aortic cross sections. A positive and statistically significant (R^2=0.58, p=0.0133) relation was found between the total protein count (structural and non-structural) and Young's Modulus. Nevertheless, when structural protein count was correlated to Young's Modulus the correlation was non-significant. Overall, spectroscopy techniques have substantially coarser resolution compared to histological methods due to the fact that they collect data from a large focal volume (Ebenstein et al. 2009; Venkatasubramanian et al. 2010).

Taken together, our stiffness results lie within the range reported in the literature. The range of values reported in the literature is wide and shifted towards higher stiffness values. This may be due to differences in tissue preparation and architecture of the aorta and coronary artery. First and foremost, the media of elastic arteries, such as the aorta, consist of a large number of concentric fenestrated elastic lamellae (Rhodin 1980; Glagov et al. 1992; Connell et al. 2008) which ensure passive recoil. A network of radial elastin fibres connects the elastin lamellae together. Muscular arteries have lower number of elastin sheets (Rhodin 1980) but higher smooth muscle cell content than elastic arteries when examined with multi-photon microscopy (Zoumi et al. 2004). The stiffness of contractile SMCs is 2.6 kPa (Matsumoto et al. 2004). Elastin has a Young's Modulus three orders of magnitude higher than SMCs, approximately 1MPa (Gosline et al. 2002). The extracellular matrix of porcine coronary media has a collagen to elastin ratio of 3.74 and collagen content of approximately 28-34% (Chen et al. 2011) and collagen appears to be

intertwined with elastin (Zoumi et al. 2004). This figure aligns with our findings; the average collagen content of porcine coronary media from our measurements is 27.7%.

Comparison of Young's Modulus from indentation experiments with stiffness derived from tensile testing is challenging for several reasons. First and foremost, one single value of stiffness is insufficient to characterise the material properties of coronary arteries because stress-strain relationship is non-linear and direction-dependent as shown by many studies (van Andel, Pistecky, and Borst 2003; Wang et al. 2006; Lally, Reid, and Prendergast 2004). Indentation tests assume that the tissue is isotropic and homogenous at the vicinity of the indentation region. Secondly, it appears that the stiffness is dependent on the method by which it is obtained. We estimated the average compressive Young's Modulus of healthy coronary arteries as 11 kPa, which lies within the range reported in the literature as discussed above. Studies which subject healthy coronary arteries to uniaxial/biaxial testing derive a stiffness range which range 5-50 MPa (Lally, Reid, and Prendergast 2004), 100-500 kPa (Wang et al. 2006), 100 kPa-2 MPa (van Andel, Pistecky, and Borst 2003). It is believed that the higher stiffness of arterial tissue when measured with macroscopic methods is attributable to the behaviour of constrained water (in intracellular and extracellular form) and its incompressibility which lead to an increased resistance to deformation. Indentation tests, in general, result in lower stiffness values than macroscopic tensile and compression testing, as reviewed here (McKee et al. 2011).

There is a great dispersion in the tissue thickness used by previous AFM studies (**Table 6**); ranging from 5 μm (Akhtar et al. 2009) up to 1 mm (Hemmasizadeh, Darvish, and Autieri 2012). It has been indicated that there might be a systematic bias introduced in the stiffness measurements if the tissue is thinner than 20 μm (Sicard, Fredenburgh, and Tschumperlin 2017). Thin films (<10μm) and cells are particularly prone to this apparent increase in the Young's Modulus due to a stiff substrate. It is customary to calculate a correction factor in order to account for this (Dimitriadis et al. 2002) but such a correction appears to be less relevant when probing tissue of considerable thickness as done in this study. By doing AFM and staining on a single section it might be advantageous in co-registering tissue mechanics to histological features, but there is loss of quality of quantification of collagen density as discussed previously.

4.2. Discussion of variability of results

Atomic Force Microscopy can probe tissue in a range of scales depending on the size of the cantilever's tip, namely from micro- to nanoscale. In this study we used a pyramid-shaped tip with a radius of 8 nm (nominal value). Although we utilised, (a) the same cross section for testing and staining, and (b) a gridded substrate/coverslip to ensure the co-registration errors were minimised, the resultant tissue stiffness appeared to be correlated moderately with collagen content (**Figure 40E**). One possible reason for that could be the lack of precise control over the area where the cantilever tip lands. Cells (primarily SMCs) are the dominant tissue constituent in terms of volume (or area) fraction cells in muscular arteries, therefore it is not unreasonable that the tip of the cantilever may have probed cellular material on occasion. Other studies have selected sphere-shaped tips (Hayenga et al. 2011; Chai et al. 2014) and they argue these are better suited to measure how tissue responds collectively to a global load. A second possible reason for this result is that the relation may not be linear. A recent study (Johnston, Gaul, and Lally 2021) that investigated the effect of collagen content (quantified by Picrosirius Red stain) on the mechanical properties of fibrous caps from carotid plaques measured with uniaxial tensile testing found zero correlation between the variables. This study focused on quantifying collagen content only although collagen orientation may be a more potent factor in driving local tissue stiffness.

The inconsistency of the staining quality with Picrosirius Red introduced a great dispersion to the final co-registration. Other trichrome staining techniques, such as Elastica van Gieson (Douglas et al. 2017), label-free techniques, such as second harmonic generation microscopy (SHG) (Wegner et al. 2017), have been used to quantify collagen content. Staining with Picrosirius red stain is not commonly preferred because it is prone to overstaining artefacts which introduce bias (overestimation) into quantification of collagen content. Besides, paraffin embedding is believed to better preserve morphological details than frozen tissue sections (Tulis 2007). That aside, usually, staining quality for identification of collagen fibres depends mainly on the transparency of the section therefore, thin sections (5-10μm) are preferred, whereas in this study we performed the mechanical testing and staining on 20μm-thick tissue sections. We witnessed regional variations in the staining quality within sections that might have been caused by their non-uniform thickness (**Figure 41**). In addition, the

substantial thickness of the section is a potent source of noise from focal planes spanning through the entire thickness of the section; this artefact is further augmented by the difficulty in effective rinsing of excessive dye after the incubation in the picric acid (red dye) solution. As a result of the above, we observed a considerable amount of noise in the polarised light images (**Figure 41**). Nevertheless, we observed a considerable degree of organisation despite the effect of those artefacts with collagen fibre bundles orientated in the circumferential direction of tissue sections (**Figure 41**).

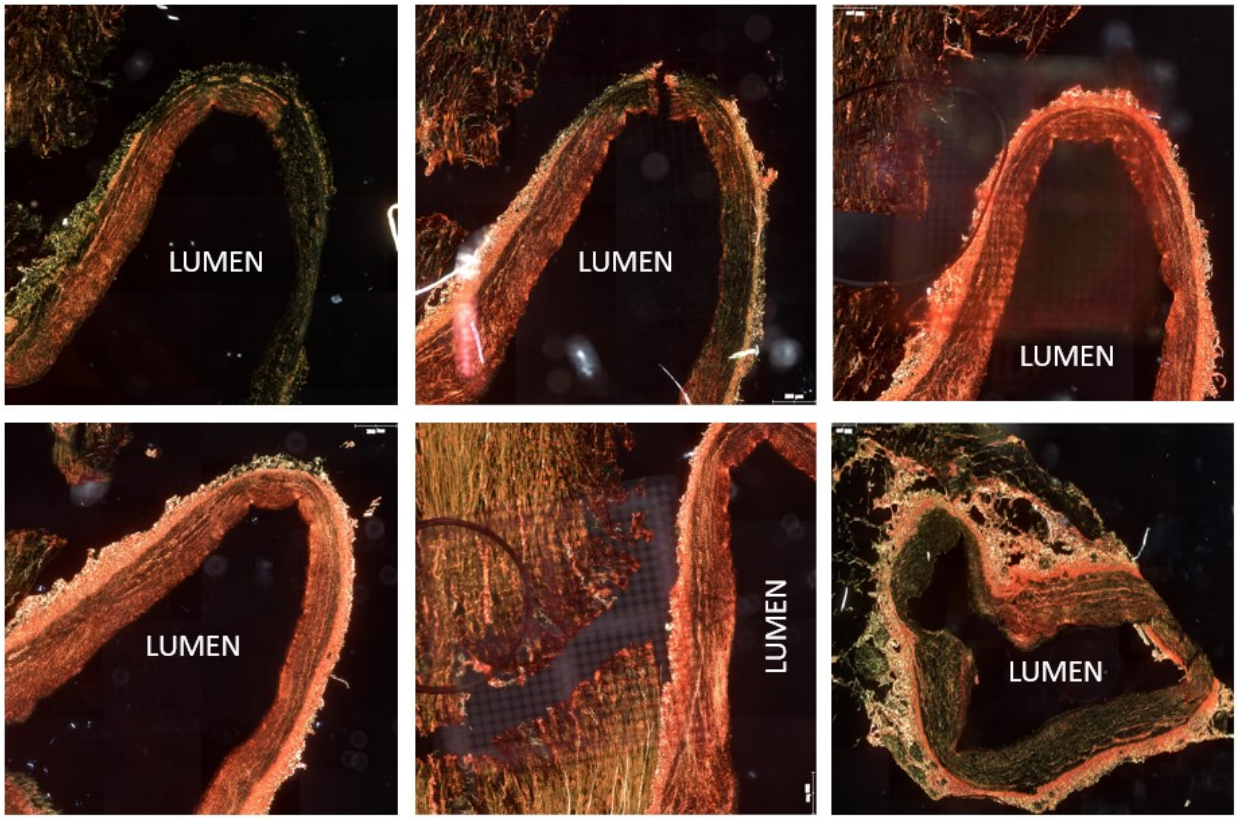

Figure 41 Representative examples of healthy coronary artery tissue sections stained with Picrosirius Red stain and imaged with linearly polarised light (dark-field). Despite presence of red-hued noise, it can be observed that collagen is organised in thick bundles that align with the circumferential direction. Scale bar: 100μm.

From our data, it seemed that freezing, cryo-sectioning and histological staining did not significantly alter the native orientation and general architecture of collagen fibre network (**Figure 41**). There may be a degree of inter-subject biological variation to the overall signal, since it is known that collagen is organised in a mesh, woven-like structure (Beenakker et al. 2012).

Even though it is customary to assume a certain degree of tissue isotropy and homogeneity when deriving material curves from macroscopic tensile tests (Lally, Reid,

and Prendergast 2004), in reality healthy coronary media is a heterogenous mixture of cells (smooth muscle, endothelial, fibroblasts) and extracellular matrix (protein fibres, such as elastin, collagen, fibronectin, fibrin) and ground matrix (proteoglycans) (Rhodin 1980). In this study we hypothesised that differences in Young's Modulus are contingent on collagen content only, however they are most probably contingent on other arterial constituents and their volume ratio within the probed indentation volume. Ideally, to obtain a better understanding of the composition of the probing volume, adjacent staining could be done (for example *Elastica Van Gieson* for elastin). Indentation techniques are better equipped to co-register mechanics to underlying composition and structure offering a competitive advantage over macroscale (tensile and compressive) material testing. Although the sample size met the requirements of our power calculation (Section 2.5), it is still lacking against other studies (Grant and Twigg 2013; Beenakker et al. 2012).

4.3. Limitations

Collagen is a birefringent molecule and Picrosirius red is a stain which binds to collagen but it is not specific unless it is combined with polarised light imaging (Rittie 2017). Most probably the colours(yellow, orange, red, green) represent fibres of different thickness rather than collagen types as reviewed upon extensively in the literature (Dayan et al. 1989; Rich and Whittaker 2005; Rittie 2017). When compared with other methods of visualisation of collagen microstructure such as Masson's trichrome and second harmonic generation microscopy (SHG), the Picrosirius red achieves higher counts (Drifka et al. 2016). Herein, a linearly polarised illumination source was used, which is a limitation. However, the lack of circularly polarised light thought not to affect the quantification of collagen fibre density as much as the visualisation of collagen orientation (Vogel et al. 2015). Due to the birefringence of the collagen molecule, a circularly polarised light it may have resulted in more detailed visualisation of the fibre architecture. We assumed that the orientation of collagen fibrils in the media is uniform, and we observed a lamellar structure which verifies our assumption (**Figure 41**). In this work we focused only on collagen content as a metric of collagen microstructure and did not investigate how local collagen orientation affects the local properties.

Extraction of Young's Modulus by fitting a contact model to the force-curves is valid only when probing at an indentation depth that does not exceed 10% of the tissue section thickness, as reviewed here (Krieg et al. 2019). In our experiments the median and interquartile range of the indentation depth (N=1379 measurements) was 1.25μm and 0.67μm respectively. Since the arterial tissue cross-sections were sufficiently thick (20μm) with regards to the indentation depth, the probed section can be considered as a semi-infinite substrate. In reality, material properties of arterial tissue cannot be fully described by a single value of stiffness (Young's Modulus) as it exhibits a strain-stiffening, direction-dependent and viscoelastic behaviour. Deriving hyperelastic material constants from indentation curves is a non-trivial task that requires experimental-computational approaches (Lin et al. 2009; Pan et al. 2016). In derivation of Young's Modulus, the strain-stiffening effect was minimised by probing the tissue at small indentation depths. Viscoelastic response of arterial tissue due to strain rate/indentation speed were minimised by applying a constant indentation speed throughout the experiments.

4.4. Conclusions

In this study we investigated the degree to which collagen content affects the compressive axial mechanical properties of healthy porcine coronary arteries with a robust nano-indentation and co-registration protocol. We found that Young's Modulus correlated weakly with collagen content. Coronary plaques from porcine models of atherosclerosis can be a valuable source for testing and development of novel mechanical characterisation such as nano-indentation testing, for biomechanical modelling of atherosclerotic plaques.

Chapter 4: Mechanical properties of atherosclerotic coronary arteries measured with Atomic Force Microscopy

1. Introduction

Coronary thrombosis and occlusion incited by plaque rupture is the most common cause of death in patients with acute coronary syndrome (Virmani et al. 2006). According to retrospective histopathological reports, advanced plaques that are rupture-prone display the following characteristics: expansive outward remodelling, a large lipid-rich necrotic core underlying a thin (<65μm, Virmani et al. (2000)) and inflamed fibrous cap with spotty microcalcifications and neo-angiogenesis (Vancraeynest et al. 2011). Imaging-based identification of plaque morphology with intracoronary imaging modalities, such as IVUS or OCT, may be insightful but there is little predictive clinical value of an acute event based on those features alone. Moreover, serial coronary angiography studies and post-mortem histopathological examination studies concur with the fact that thrombotic coronary occlusion frequently occurs in lesions of <50% stenosis severity (Falk et al. 2013a; Ambrose et al. 1988).

Aside plaque morphology, plaque structure and composition are mechanical determinants of plaque rupture. Another finding of the post-mortem examinations in thrombosed segments is that stiff (collagen-rich or calcium-rich) and soft (lipid) areas were found to be juxtaposed a few microns apart. This created a case for local failure of tissue integrity via increased structural stress (stress concentrations) exceeding local tissue strength (Richardson, Davies, and Born 1989; Falk 1992; Brown et al. 2016). Given that fibrous cap rupture is a mechanical phenomenon, biomechanical analyses could be a useful tool for preclinical assessment of rupture potential of coronary plaques. Limited understanding of the *in vivo* structural heterogeneity at a micrometre scale poses a hindrance to accurate predictions of plaque rupture location.

Estimation of plaque rupture risk with computational methods requires information about the mechanical properties of plaques. Ideally, mechanical properties

measured *in vivo* with non-destructive modalities such as ultrasound or magnetic resonance imaging would be desirable but such modalities lack large-scale validation and sufficient resolution commensurate with the spatial heterogeneity of the plaque (Mahmood et al. 2016; Mariappan, Glaser, and Ehman 2010). *Ex vivo* macro-mechanical (uniaxial/biaxial tensile, compression and inflation) testing has been the predominant way of extracting mechanical properties of diseased coronary arteries and atherosclerotic arterial tissue in general (Walsh et al. 2014; Akyildiz, Speelman, and Gijsen 2014). Although such techniques are useful for capturing the hyper-elastic response of plaques, they are agnostic to local variations of plaque stiffness. Another constraint of macro-mechanical testing is the limited ability to relate tissue mechanics to amount of plaque constituents in a quantitative manner. These issues are important when seeking to understand the driving forces underlying plaque rupture.

Collagen is a primary biomechanical constituent of atherosclerotic plaques conferring anisotropic strength. The contribution of collagen to the load bearing capacity of the diseased intima does not only depend on the stiffness of individual collagen fibres but is affected by other parameters such as their distribution and orientation (Liang et al. 2013; Koskinas et al. 2013b). So far, quantitative relationships between collagen microstructure and plaque mechanical properties on a micrometre scale have not been established. Another major source of anisotropy in plaques is the soft, necrotic core which is rich in cholesterol esters, cholesteryl esters, phospholipids and triglycerides (Small 1988; Falk 2006). The softness of the necrotic core renders mechanical testing with tensile testing particularly challenging as they might be restricted to specimens of sufficient size.

An alternative *ex vivo* technique for deriving plaque mechanical properties is nano-indentation testing. As a technique that is known for studying cell mechanics, its scale of operation can range from the microscale down to the nanoscale. By working on tissue sections, it can be combined with routine histological methods to study changes in tissue properties related to composition and microstructure. Applications in arterial tissue and particularly coronary plaques is very limited with only one study having been carried out in human coronary arteries (Rezvani-Sharif, Tafazzoli-Shadpour, and Avolio 2019b) (**Table 8**). The optimal method for studying tissue mechanics of arterial tissue with this method has not been comprehensively established.

In this chapter we hypothesise that mechanical properties of atherosclerotic plaque are softer than those of the healthy coronary wall. We also hypothesised that within plaques material properties are dependent on composition and structure. To test this hypothesis, we developed a method to measure local plaque properties with Atomic Force Microscopy and co-registered them with local metrics of composition and microstructure by histological methods.

Table 8 List of micro- and nano-indentation studies on snap-frozen **atherosclerotic** arterial tissue with special focus on tissue type and preparation practice, measured tissue stiffness and co-registration strategy of mechanics with histological features. Stiffness is reported as mean ± standard deviation, unless otherwise noted.

Study	Tissue type and preparation	Stiffness values and co-registration method with histology	Sample size
Rezvani-Sharif, Tafazzoli-Shadpour, and Avolio (2019a)	Species: human Vessel: **aorta** Thickness: 20 µm Temperature: ambient Hydration: PBS	Visual registration of stiffness to locations within plaques with the help of adjacent stains (H&E and Verhoeff van Gieson) *Fibrous cap: 15.5 ± 2.6 kPa,* *Calcification: 103.7 ± 19.5 kPa* *Lipid pool: 3.5 ± 1.2 kPa* *Healthy aortic media: 17.9 ± 7.2 kPa*	n=430 force curves
Rezvani-Sharif, Tafazzoli-Shadpour, and Avolio (2019b)	Species: human Vessel: **coronary artery** Thickness: 20 µm Temperature: ambient Hydration: PBS	Visual registration with adjacent sections stained with H&E. *Fibrous cap: 14.1 ± 3.8 kPa* *Fibrous intima: 17.6 ± 3.2 kPa* *Calcification: 96.1 ± 18.8 kPa* *Lipid pool: 2.7 ± 1.8 kPa* *Healthy coronary media: 10.7 ± 3.3 kPa*	n=3200 force curves
Chai et al. (2013)	Species: human Vessel: **carotid artery** Thickness: 200 µm Temperature: ambient Hydration: none	Comparison of collagen-rich and collagen poor locations (with fluorescent dye) in advanced plaques. *Range: 6-891 kPa* *Median: 30 kPa.*	n=574 force curves
Tracqui et al. (2011)	Species: mouse Vessel: **aorta** Thickness: 16µm Temperature: ambient Hydration: KH buffer	Visual registration with stained adjacent sections. *Cellular fibrotic: 10.4 ± 5.7 kPa.* *Hypocellular fibrous caps: 59.4 ± 47.4 kPa* *Lipid-rich areas: 5.5 ± 3.5 kPa.*	n=1000 force curves
Barrett et al. (2009)	Species: human Vessel: **carotid artery** Thickness: 500 µm Temperature: ambient Hydration: none	Measurements on fibrous caps *Range: 21-300 kPa* *Median: 33 kPa*	n=50 force curves
Ebenstein et al. (2009)	Species: human Vessel: **carotid artery** Thickness: not reported Temperature: ambient Hydration: none	*Haematoma: 230 ± 210 kPa* *Fibrous: 270 ± 150 kPa* *Calcified/fibrous: 2.1 ± 5.4 MPa* *Calcified: 0.7 ± 2.3 GPa*	n=300-600 force curves

2. Materials and Methods

Tissue preparation

Coronary artery tissue sections were taken from a porcine model of coronary atherosclerosis (Pedrigi et al. 2015; Al-Mashhadi et al. 2013). Transgenic hypercholesterolaemic minipigs of Yucatan background were administered a high-fat, high cholesterol diet. A shear-modifying (stenotic) stent was placed in the RCA while the LAD served as non-stented control. Advanced plaques were witnessed within 18 weeks after stent placement in the areas upstream and downstream (within 2mm) of the stent. Serial monoplane angiography and OCT data were collected at baseline and 18 weeks when the animals were euthanized. After exsanguination, the RCA and LADs were dissected from the myocardium by an experienced histologist (Dr. Daniele Carassiti). The arteries were then divided into 2mm segments, were rapid-frozen in isopentane and stored in -80^{o}C until further use.

Formation of advanced plaques downstream of the distal side of the shear-modifying stent in the RCA arteries was verified by careful inspection of the OCT pullback recording acquired at week 18. Frozen blocks situated downstream of the distal side of the stenotic stent were serially sectioned**.** Seven sections were derived per 100μm of frozen tissue material. One of those sections (20μm) was destined for mechanical testing, another three sections (10μm each) for histological staining to assess general pathology (Hematoxylin and Eosin), lipid content (Oil-Red-O) and macrophage infiltration (CD68) and the remaining two (20μm) were utlilised for analyses not part of the current project.

Sampling strategy

For the sections allocated for mechanical testing, the following regions were tested. The presence of stiff (collagen, calcium) and soft (lipid) components in advanced plaques are source of stress concentrations which are believed to be precursors of plaque rupture (Falk, Shah, and Fuster 1995; Cardoso and Weinbaum 2014). Collagen can be found within fibrous caps that endows them with strength, whereas necrotic core is rich

in cholesterol esters. Within the fibrous cap, there are another two distinct areas that are of additional biomechanical interest, namely the middle of the cap and the fibrous cap shoulder (that is where the fibrous cap meets the diseased intima). In 60% of plaque rupture cases the rupture takes place in the plaque shoulder and 30% takes place along the middle section of the fibrous cap (Virmani et al. 2006; Falk et al. 2013b). Therefore, the above three location areas were targeted in the tissue sections guided by brightfield images (**Figure 42A**) and the location was verified post-measurement by assessing the stained tissue and adjacent stains.

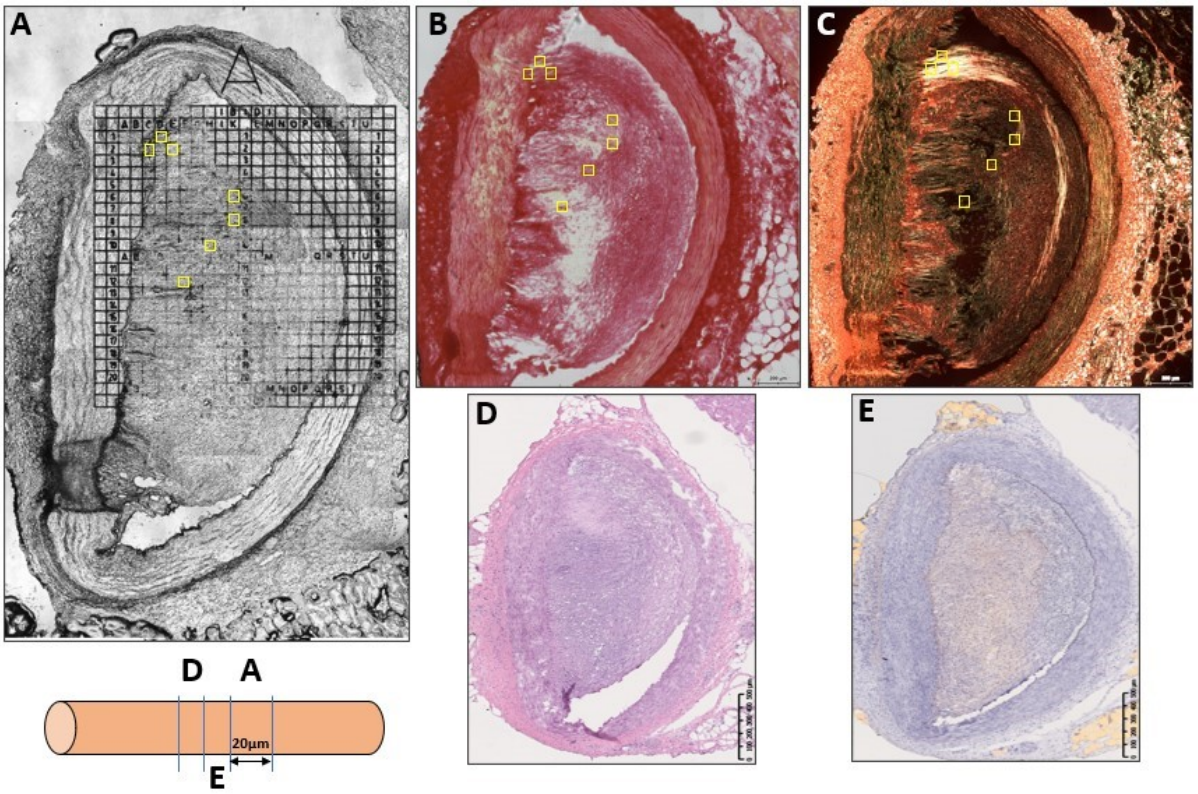

Figure 42 Approach to co-registration of AFM measurement locations to the local collagen microstructure in atherosclerotic coronary plaques. (A) Brightfield image of a tissue section with indentation locations (50µm x 50µm) shown in yellow. (B) Same section stained with Picrosirius Red imaged with brightfield light, (C) Same section stained with Picrosirius Red imaged with linearly polarised light, (D) Adjacent section stained with Hematoxylin and Eosin, (E) Adjacent section stained with Oil-Red-O (lipids).

Mechanical testing

Immediately after sectioning, the tissue samples were picked up with gridded coverslips (Ibidi GmbH, Martinsried, Germany) precoated with 0.1%w/v poly-L-lysine (Sigma Aldrich, St. Louis, MO, USA). To prevent any condensation from forming the coverslip was put inside a petri dish that was sealed with parafilm (Sigma Aldrich, St.

Louis, MO, USA). The tissue was probed with a MNSL-10F probe (Bruker, Germany) with a nominal cantilever stiffness of 0.6 N/m on a NanoWizard4 bio-AFM machine. The probe was calibrated with the thermal noise method (Butt and Jaschke 1995) prior to mechanical testing. The tissue was indented until a force of 10nN had been reached with a constant indentation speed of 2μm/sec (default). Overall, the indentation parameters were tuned so that the force curve corresponded to the linear elastic regime (<10% of tissue thickness, or 2μm). To prevent signal degradation, the duration of the scan was limited to one hour. All scans took place in room temperature (~23°C) and the tissue was submerged in a physiological solution (PBS). The probes were regularly decontaminated by submerging them in a 3 mg/ml collagenase solution at 37.0°C for 1 hour.

Extraction of Young's modulus from force curves

The raw force-displacement curves were imported to JPKSPM Data Processing (v6.1) software. A custom-made subroutine that was created from a list of standard curve processing operations was applied uniformly in the entire cohort of force curves. A Hertzian contact mechanics model was fitted to the experimental force curves in order to extract Young's Modulus (YM) according to the equation 1:

$$F = \frac{2}{\pi}\frac{YM}{1-\nu^2}\tan(a)\,\delta^2 \quad \text{(Eq. 1)}$$

where F: Recorded force,
δ: Indentation depth
YM: Young's Modulus,
ν: Poisson's ratio (ν=0.5),
α: Half-opening angle of tip

Assuming no adhesion and friction forces, when a sample is probed with a pyramidal tip the force increases parabolically with respect to the indentation depth (Bilodeau 1992). The first 2μm (10% of sample thickness) of the indentation depth was fitted with the contact model. The extraction of Young's Modulus was done without reference to the outputs of the post-processing software.

The root mean square (RMS) of the force residuals was used to assess the goodness of fit. Raw force curves were rejected from fitting process according to the criteria: contact point not clearly defined, sign of material yield, low signal to noise ratio

(RMS>200nN), increase of adhesion forces which interfered with smooth engagement and disengagement of the tip and contamination of probe.

Staining, polarised light imaging, and digitization

After mechanical testing, the same tissue section was stained with Picrosirius red for collagen, whereas adjacent sections (cut at 10μm thickness) were stained with Hematoxylin and Eosin (general pathology) and Oil-Red-O (lipids). Picrosirius Red stained sections were analysed using a Zeiss AxioObserver (Jena, Germany) microscope equipped and a built-in capacity for linearly polarised (dark field) microscopy. Acquisition was done with a 20x (Zeiss EC Plan-Neofluar 20x/0.5) objective. Image acquisition took place under identical conditions (exposure time, lamp intensity). Background illumination correction was applied in all samples. The images were stored in a high-resolution format (.tiff) and were imported in ImageJ v1.53c (NIH, USA) and analysed.

Quantification of collagen microstructure

A measure of the total (all types) collagen density was extracted by converting the polarised light image to grayscale. Grayscale images were subjected to an identical threshold level (level: 75/255) that resulted in binary images from which collagen density was derived as the percentage of white pixels within a ROI. The threshold level was selected by validating the collagen content of the medial layer against measurements of collagen content from porcine coronary arteries derived with second harmonic generation microscopy (Chen and Kassab 2016).

Statistical analysis

For each indentation location twenty-five (n=25) force curves were obtained. For each curve, a Young's Modulus was extracted and the median value of the twenty-five values was assigned to be the representative stiffness of the indentation location. Each value of Young's Modulus (median of 25 values) was paired with one value of collagen fibre density. We previously estimated the co-registration error as 4.02% (see **General Methods**, Chapter 3.4). Log-normalisation of Young's Modulus frequency distributions obtained from indentation tests is common in the literature (Hayenga et al. 2011; Grant

and Twigg 2013; Beenakker et al. 2012), and this was the method used to show frequency/histogram distributions of stiffness.

The log-normalised pairs of Young's Modulus and collagen fibre density were categorised into bins according to the following procedure. First, the collagen fibre density data were sorted from lowest to highest re-arranging the Young's Modulus values. A bin size of six data points was defined. Then for every six values of the collagen fibre density or Young's Modulus data, the median value was calculated and replaced the former six values creating new pairs. Statistical comparisons were made with Wilcoxon Rank Sum and Wilcoxon signed rank tests and a p-value of less than 0.05 was considered statistically significant. Matlab 2020b (Natick, Massachusetts) was used for statistical analyses.

1. Results

In total, n=1898 force curves were collected (average discard rate: 20%) from 90 locations (50μm x 50μm square regions) in n=16 tissue sections from atherosclerotic porcine coronary arteries.

Although selection of the indentation locations was guided by the brightfield AFM microscope images (**Figure 42** A), their full histological classification was done post-measurement with the aid of adjacent 10μm tissue sections stained with Hematoxylin & Eosin, Oil-Red-O and CD68 where available. The indentation locations within the plaques were sub-classified as follows: 20 locations (n=392 curves) were found to reside within a lipid rich necrotic core (LRNC), 70 locations within a fibrous cap, 40 (n=868 curves) of them were identified to reside in the middle of the cap (MC) and the remaining 30 (n=638 curves) in the shoulder of the cap (SH).

Overall, the mechanical properties of the healthy vessel wall (median = 11.0 kPa, n=1379 force curves) were found to be significantly stiffer ($p=1.34\cdot10^{-10}$) than plaque tissue (median=4.3 kPa, n=1898 force curves) (**Table 9**). Within plaques, lipid-rich areas (median=2.2 kPa, n=392 force curves) were found significantly softer ($p=1.47\cdot10^{-4}$) than areas rich in collagen, such as the fibrous cap (median=4.9 kPa, n=1506 force curves). No statistical difference (p=0.89) was found between measurements in the middle of the fibrous cap (median=4.8 kPa, n=868 force curves) and the cap shoulder (median=5.1 kPa, n=638 force curves). The median collagen content of the fibrous cap was estimated as

16.2% (n=24 locations), half of that of healthy coronary media (32.4%, n=68 locations). The stiffness of the fibrous cap was found to be almost half as much as that of healthy tissue.

Table 9 Summary of nano-mechanical properties (panel A) and collagen microstructure measurements (panel B) per histological group. Plaque group consists of measurements in lipid-rich necrotic core and measurements in the fibrous cap. Fibrous cap group consists of measurements in the fibrous cap shoulder and mid-cap. Discard rate is considered in the final number of processable force curves. Estimation of collagen content is shown in panel B. Due to technical difficulties collagen metrics for the diseased group were gathered from a limited number of tissue sections, thus histological classification of AFM measurements (panel A) was done on the basis of adjacent H&E and Oil-Red-O sections.

	Nano-mechanical properties			**Collagen microstructure**	
	Number of force curves	Young's Modulus (kPa)		Collagen density (%)	Number of ROIs
		Median	IQR		
Healthy wall	1379	11.0	8.6	32.4	67
Plaque	1898	4.4	2.8	-	-
Lipid-rich necrotic core	392	2.2	1.7	2.7	7
Fibrous cap	1506	5.0	3.1	16.2	24
Shoulder	638	4.8	3.4	17.8	14
Mid-cap	868	5.1	2.8	14.7	10

In addition, the frequency distribution of the log-transformed Young's Moduli of healthy and plaque regions was plotted (**Figure 43A**). The lower stiffness of lipid-rich areas was found to shift the distribution to lower stiffness values (**Figure 43B**).

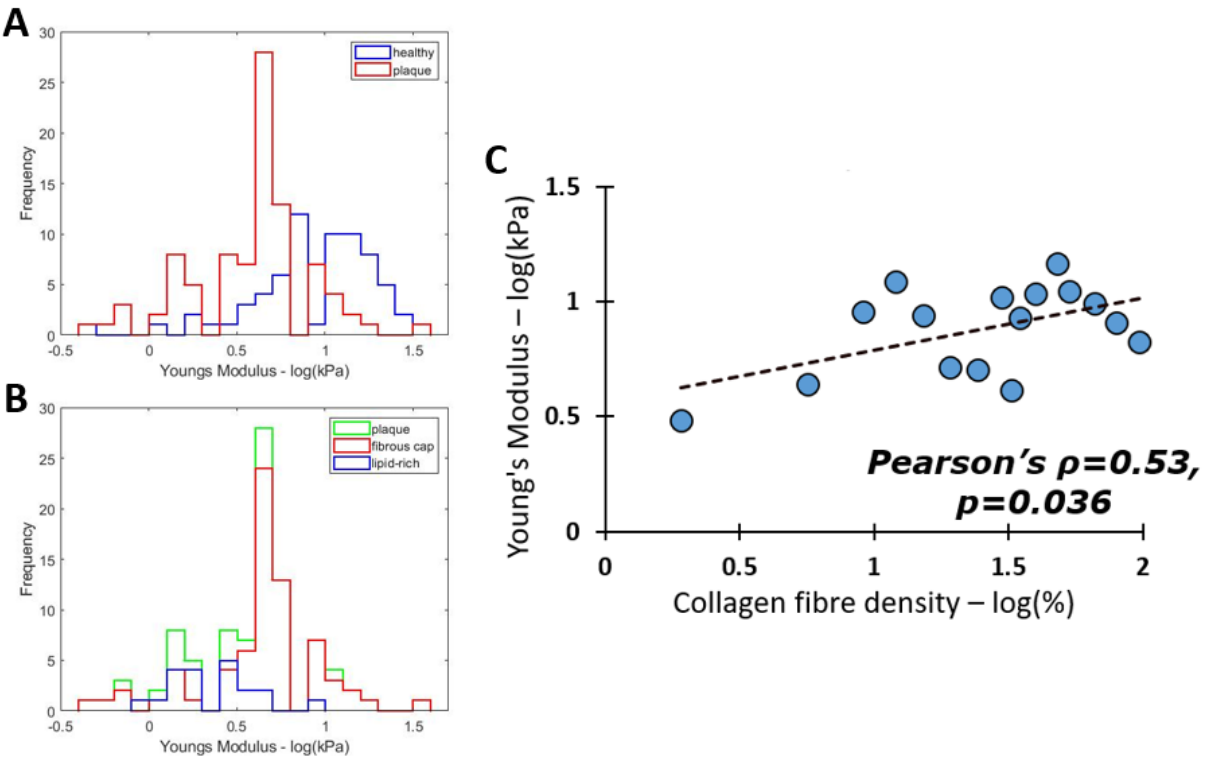

Figure 43 (left) Frequency distributions of log-normalised Young's Modulus values of different histology groups. (A) Healthy: blue, plaque: red. (B) Plaque: green, fibrous cap: red, lipid-rich: blue. Lipid-rich areas were defined as areas with <5% collagen density and with paucity of cells on H&E and high in lipid (red stain) in Oil-Red-O stain. (C) Scatterplot of co-registered collagen fibre density and Young's Modulus measurements located in healthy coronary wall (n=67) and fibrous cap (n=24). The co-registered datapoints were binned to 17 groups of 6 data points each. A moderate, positive correlation (Pearson's ρ=0.53, p=0.036) was found to relate the variables.

2. Discussion

Local plaque strength is believed to be determined by local plaque composition and structure. Knowledge of plaque material properties are essential for biomechanical models that estimate plaque rupture risk. So far, the literature regarding effect of plaque composition on local plaque strength is scant due to the fact that tensile testing method being preferred as the testing modality for interrogating the mechanical properties of atherosclerotic plaques (Walsh et al. 2014; Teng et al. 2014; Akyildiz, Speelman, and Gijsen 2014). In this chapter we measured the local mechanical properties of porcine coronary plaques with indentation testing and attempted to relate them to histological structure.

A major challenge of mechanical characterisation methods is the ability to link accurately the material properties to the underlying histological structure**.** Herein, the co-registration is conducted with the aid of a gridded coverslip and by staining the exact same tissue section that was used for mechanical testing. We focused on the primary structural constituents which give plaque the greatest degree of anisotropy, namely collagen and lipid. The presence of soft and stiff plaque components within advanced plaques is believed to be an origin of stress concentrations (Cheng et al. 1993a; Finet, Ohayon, and Rioufol 2004; Maldonado et al. 2012) that can trigger plaque rupture if local material strength is exceeded.

To summarise our findings, plaque tissue was found significantly softer than healthy coronary media. Within plaques, stiffness of the fibrous cap was found to be independent of the location within the cap (mid cap vs shoulder). Lipid-rich areas exhibited significantly lower Young's Modulus than fibrous cap areas.

One of the most surprising findings was that fibrous cap has lower Young's Modulus than healthy wall. A question worth asking is whether this estimate is representative and accurate and there are quite a few reasons to consider otherwise. First and foremost, indentation measurements were done on unstained tissue which made precise localisation of collagen-rich areas difficult on the basis of brightfield microscopy. Given the spatial heterogeneity of plaque tissue, plaque constituents other than collagen, namely cells and lipids might have influenced the force signal and gave rise to lower stiffness values. Secondly, evolving plaques from animal models might not have the advanced features such as crosslinked collagen deposition with paucity of cells, calcification which can shift fibrous cap stiffness to higher values when compared to advanced coronary plaques from humans (Rezvani-Sharif, Tafazzoli-Shadpour, and Avolio 2019b). Thirdly, we estimated the collagen content of the fibrous cap as 16.2% half that of that of the healthy coronary wall. Even though a reduction in collagen content could explain the reduction in Young's Modulus, it is arguable that fibrous cap has that low collagen density. Even though the co-registration process was facilitated with the use of gridded coverslips, more often than not the tissue was laid away from a grid therefore co-registration was just done on the basis of visual registration. On top of that, the estimate is derived from a low number of ROIs (square regions of interest).

To the best of our knowledge there is only one study which has investigated the mechanical properties of atherosclerotic human coronary arteries using an indentation testing set-up (Rezvani-Sharif, Tafazzoli-Shadpour, and Avolio 2019b) (**Table 8**). In that report forty (n=40), 20μm frozen tissue sections from advanced coronary plaques were probed with a nano-indenter, similar to our study. The tissue sections were kept hydrated with PBS throughout the indentation experiments. Different areas within plaques namely fibrous intima, fibrous cap, lipid rich and calcified areas were probed. Collectively, the fibrous caps were found to be 1.4 times stiffer than healthy coronary media in contrast to our study where stiffness of the fibrous cap was half as that of the healthy coronary media. There was a greater degree of agreement when comparing the mechanical properties of lipid-rich areas between the two studies. They reported that lipid-rich areas were found to be approximately 3 times softer than healthy coronary media, whilst our results indicated that lipid-rich areas are 5 times softer than healthy coronary media.

There are several reasons to explain why our findings differ when compared with that study. One aspect concerns methodological reasons. It is true that Rezvani-Sharif, Tafazzoli-Shadpour, and Avolio (2019b) gathered data from a much higher sample size (number of force curves) This is also reflected in the comparatively lower variability of the reported average stiffness values across histology groups. Despite the much higher sample size, the reported stiffness of healthy human coronary media (average=10.7 kPa) is almost identical to the one reported in the previous Data Chapter for healthy porcine coronary media (median=11.0 kPa).

Another study conducted in mice (Tracqui et al. 2011) (**Table 8**) compared the Young's Modulus between areas of different composition within aortic plaques guided by serial histological staining. They divided the plaques into three distinct regions: hypocellular fibrotic, lipid-rich and cellular fibrotic, based on three stains: (i) a trichrome, haematoxylin, erythrosine, safran (HES) stain, (ii) an oil red-O staining of lipid deposits, and (iii) a smooth muscular cell (SMC) staining. Hypocellular fibrotic areas (or, rich in fibrosis) were found to be the stiffest among all three (59.4 ± 47.4 kPa), whereas lipid-rich areas were found the softest among all (5.5 ± 3.5 kPa). Cellular fibrotic regions exhibited an average Young's Modulus of 10.5 ± 5.7 kPa.

Chai et al. (2013) (**Table 8**) utilised an indentation test and inverse-FE method to estimate the mechanical properties of advanced human carotid plaques. Within those plaques, areas with different composition and structure were measured. They reported significant differences between the properties of lipid-rich (necrotic core) and collagen-rich regions (fibrous cap), which is consistent with our findings. In addition, they showed that collagen structure within fibrous caps might not play a significant role since they reported no significant differences in the Young's Moduli of middle of cap and shoulder of cap; our findings also confirm that.

Despite the difference in the Young's Modulus which can be explained by difference in the species, anatomical location, plaque maturity, tissue preparation, most of the studies in **Table 8** report a high variation/dispersion in their results (coefficient of variation >=50%) which showcases the challenge of characterising plaques with a single value of stiffness.

So far, we have investigated the effect of collagen content on local mechanical properties, but collagen orientation might have a greater bearing on the mechanical properties. In a recent study (Johnston, Gaul, and Lally 2021), fibrous caps from carotid plaques (n=20) were subjected to tensile testing and histological quantification of collagen content and orientation. Fibrous caps whose collagen fibre orientation was predominantly in the circumferential direction of the native vessel showed higher ultimate tensile strength than cap strips whose predominant orientation was axial. Moreover, collagen density quantified by Picrosirius Red was found to be uncorrelated with tensile strength of the tissue strips.

There are many limitations of this work. In general, mechanical properties of plaque are anisotropic and hyperelastic. Although at present it is not straight forward to derive hyperelastic material properties from indentation data due to limited application range of the contact mechanical models. Herein we measured the axial compressive properties of coronary plaques we assumed that the properties are isotropic. There is concrete evidence that circumferential properties are stiffer than axial properties (Akyildiz, Speelman, and Gijsen 2014; Johnston, Gaul, and Lally 2021). Nevertheless, this section-by-section method of material testing has the potential of being paired with 3-D Histology (Segers et al. 2007) towards obtaining regional

differences in plaque stiffness which can shed light in local mechanisms involved in determining plaque rupture risk.

Another limitation is the fact that the plaques tested are less mature than advanced coronary plaques which tend to be more fibrous, calcified and as a result stiffer. Therefore, our findings cannot be extrapolated for advanced human plaques, but it may be that in fibrous caps, structure may be more important than pure composition. Interestingly, it has been recently demonstrated (Johnston, Gaul, and Lally 2021) that fibrous caps whose collagen fibres align with the loading direction (quantified by small angle light scattering) exhibit higher ultimate strength than caps whose fibres align perpendicular to the loading direction. Their findings indicate that collagen content alone may not play a major role in plaque strength. They did not witness a correlation between the collagen content and ultimate tensile stress and strain of the plaque caps. In reality, the collagen network in plaques displays a three dimensional distribution as visualised with novel imaging techniques such as small angle light scattering (SALS) (Akyildiz et al. 2017) and magnetic resonance diffusion tensor imaging (DTI) (Opriessnig et al. 2018) and clearly a section-by-section staining strategy is agnostic to this distribution.

Also, another limitation was the difficulty in accurately locating the area where the AFM measurements where made in some sections where the tissue was not laid in the area where the coverslip grid was located. In other studies, such as Chai et al. (2013) (**Table 8**), a fluorescent probe was used to visualise collagen architecture in carotid plaque prior to indentation testing. This method might aid in targeting locations with different collagen content. It is very challenging to do that on the basis of brightfield microscopy. Finally, while there is a body of literature discussing swelling effects of collagen with PBS (Andriotis et al. 2015; Andrews et al. 2015), quantification and study of the effect of hydration on the mechanical properties of coronary arteries was out of the scope of this work. It is generally established that the less hydrated the collagen, the stiffer it is (Grant et al. 2008). We decided to perform the measurements in a hydrated environment so as to mimic the hydration state of the *in vivo* environment as close as possible.

To conclude, in this study we investigated the degree to which collagen content affects the compressive axial mechanical properties of atherosclerotic porcine coronary

arteries. We related regional differences in Young's Modulus to presence or absence of local collagen microstructure and compared the result against measurements in healthy coronary arteries. Coronary plaques from porcine models of atherosclerosis can be a valuable source for testing and development of novel mechanical characterisation, such as nano-indentation testing, for biomechanical modelling of atherosclerotic plaques.

Chapter 5: General Discussion

Experimental and clinical data show that biomechanical forces have an important role in the natural history of coronary atherosclerosis (Brown et al. 2016). Therefore, computational approaches which analyse the biomechanical environment of atherosclerotic plaques have come to the forefront over the last 15 years. So far, macroscopic (tensile/compressive/inflation) methods have been extensively used to derive mechanical properties of atherosclerotic plaques that are inputted into biomechanical models to investigate a potential role of plaque structural stress in coronary plaque progression/regression or acute rupture. This work was motivated by the inadequacy of such material testing techniques to address the heterogenous mechanical properties of plaques from a constituent point of view.

Herein, a microstructural approach was adopted to measure the mechanical properties of healthy and atherosclerotic coronary vessel wall. An indentation technique, Atomic Force Microscopy, was used for that reason. Given the critical role of collagen in the biomechanical properties of healthy and atherosclerotic arteries we hypothesised that those are contingent on the local collagen microstructure. Due to the lack of a well-established indentation methodology, we developed and optimised a robust nano-indentation protocol which enables high-resolution measurements on tissue sections and co-registers them with the local collagen microstructure.

In the first data chapter we investigated the degree to which collagen content affects the local axial compressive mechanical properties of healthy coronary arteries. We conducted measurements in n=14 arterial cross sections from three non-atherosclerotic coronary arteries. We did not find a positive correlation between collagen fibre density and Young's Modulus which refuted our initial hypothesis. There are multiple reasons for this, methodological and biological, as discussed in the chapter. To address that it is evident that sample size needs to be increased in order a more robust relation between collagen fibre density and Young's Modulus to be derived. Still, however, we have to bear in mind that a nano-structural approach has been taken to assess the mechanical properties of a markedly heterogenous material, the healthy arterial wall, and this should balance our expectation – having a very high-resolution material testing modality can be a double-edged sword.

In the second data chapter we measured the nano-mechanical properties of advanced atherosclerotic plaques using a porcine model of atherosclerosis as a surrogate for the human condition. We found that plaque was on average softer than the normal arterial wall which is consistent with relevant literature. Stiffness within plaques depended on local collagen microstructure as lipid-rich areas were significantly softer than regions within fibrous caps. Fibrous cap stiffness seemed to be independent of location (mid-cap, shoulder), a finding that is consistent with other indentation studies on human carotid plaques (Chai et al. 2013). What was surprising was that the mechanical properties of the fibrous cap were significantly softer than those of the healthy wall. By contrast, in Rezvani-Sharif, Tafazzoli-Shadpour, and Avolio (2019b) it was reported that fibrous cap regions within advanced human coronary plaques were 1.7 times stiffer than the healthy coronary wall. The reason behind this discrepancy may lie in the maturity of the advanced plaques studied herein which are only 18 weeks old. It is known that early during cap formation, caps are heavily infiltrated by SMCs, macrophages and T lymphocytes (Falk 1992). Lee et al. (1991) assessed 27 intact human aortic fibrous caps and found that caps deficient in cells (hypocellular) were 1-2 times stiffer than cellular caps. Moreover, collagen may not be crosslinked during early cap formation which leads to weakened mechanical properties. It has been observed that early plaques are more prone to rupture than more advanced, severely stenotic ones (Ambrose et al. 1988; Little et al. 1988). This finding seems to corroborate with our findings which show that early plaques might have softer mechanical properties leading to this higher susceptibility to rupture.

Even though the sample sizes used in this study are comparable to other studies, still more measurements need to be conducted to decrease overall variability. Increase of sample size will also help to exclude sections which have staining artefacts towards establishing a stronger correlation between the local collagen fibre density and Young's Modulus. This work focused on quantification of collagen area density as a metric of collagen microstructure. However, collagen fibre orientation is another metric that seems to affect the mechanical properties of arterial tissue (Chen and Kassab 2016; Johnston, Gaul, and Lally 2021). However, investigation of the effect of collagen orientation on the local stiffness of arterial tissue has not been done herein.

Chapter 6: Future work

The measurements done in this work in healthy and atherosclerotic arterial tissue can be used towards informing material models for characterisation of healthy and plaque tissue within FE or FSI models of healthy and atherosclerotic coronary arteries. As mentioned previously, it is customary for modelling approaches to utilise material properties coming from macroscopic testing (tensile, compression or inflation). Utilisation of indentation measurements directly (force curves) is not a straightforward task given that the stretch/compression range (1-1.2) for indentation tests and uniaxial/biaxial testing differ markedly (1-1.7).

One potential way of implementing the experimental results into a literature-based hyperelastic material model would be to derive a scale factor which could be used to tune it according to the local collagen microstructure. Given that the correlation of collagen area density and Young's Modulus was weak, all measurements within healthy tissue could be used to extract one estimation of the Young's Modulus. The next step could be to extract the Young's Modulus of the hyperelastic model (curve tangent at 10% strain). The ratio of the nano-measured Young's Modulus to the one derived from the hyperelastic material model could be multiplied with the entire stress-stretch (literature-based) curve to yield a hyperelastic material model. A similar methodology could be used for all histological groups within diseased tissue sections (lipid-rich areas, fibrous cap) yielding hyperelastic properties but with Young's Moduli tuned according to the nano-mechanical measurements.

Bibliography

Akhtar, R., H. K. Graham, B. Derby, M. J. Sherratt, A. W. Trafford, R. S. Chadwick, and N. Gavara. 2016. “Frequency-Modulated Atomic Force Microscopy Localises Viscoelastic Remodelling in the Ageing Sheep Aorta.” *Journal of the Mechanical Behavior of Biomedical Materials* 64: 10–17. https://doi.org/10.1016/j.jmbbm.2016.07.018.

Akhtar, Riaz, N. Schwarzer, M. J. Sherratt, R. E.B. Watson, H. K. Graham, A. W. Trafford, P. M. Mummery, and B. Derby. 2009. “Nanoindentation of Histological Specimens: Mapping the Elastic Properties of Soft Tissues.” *Journal of Materials Research* 24 (3): 638–46. https://doi.org/10.1557/jmr.2009.0130.

Akyildiz, Ali C., Chen Ket Chai, Cees W.J. Oomens, Aad van der Lugt, Frank P.T. Baaijens, Gustav J. Strijkers, and Frank J.H. Gijsen. 2017. “3D Fiber Orientation in Atherosclerotic Carotid Plaques.” *Journal of Structural Biology* 200 (1): 28–35. https://doi.org/10.1016/j.jsb.2017.08.003.

Akyildiz, Ali C., Lambert Speelman, and Frank J H Gijsen. 2014. “Mechanical Properties of Human Atherosclerotic Intima Tissue.” *Journal of Biomechanics* 47 (4): 773–83. https://doi.org/10.1016/j.jbiomech.2014.01.019.

Al-Mashhadi, Rozh H., Charlotte B. Sørensen, Peter M. Kragh, Christina Christoffersen, Martin B. Mortensen, Lars P. Tolbod, Troels Thim, et al. 2013. “Familial Hypercholesterolemia and Atherosclerosis in Cloned Minipigs Created by DNA Transposition of a Human PCSK9 Gain-of-Function Mutant.” *Science Translational Medicine* 5 (166). https://doi.org/10.1126/scitranslmed.3004853.

Ali, Mir H, Daryl P Pearlstein, Carol E Mathieu, and Paul T Schumacker. 2004. “Mitochondrial Requirement for Endothelial Responses to Cyclic Strain: Implications for Mechanotransduction.” *Am J Physiol Lung Cell Mol Physiol* 287 (3): 486–96. https://doi.org/10.1152/ajplung.00389.2003.

Ambrose, John A., Mark A. Tannenbaum, Dimitrios Alexopoulos, Craig E. Hjemdahl-Monsen, Jeffrey Leavy, Melvin Weiss, Susan Borrico, Richard Gorlin, and Valentin Fuster. 1988. “Angiographic Progression of Coronary Artery Disease and the Development of Myocardial Infarction.” *Journal of the American College of Cardiology* 12 (1): 56–62. https://doi.org/10.1016/0735-1097(88)90356-7.

Andel, Carolien van, Peter V Pistecky, and Cornelius Borst. 2003. “Mechanical Properties of Porcine and Human Arteries: Implications for Coronary Anastomotic Connectors.” *Annals of Thoracic Surgery* 76 (1): 64–65. https://doi.org/10.1016/S0003-4975(03)00541-1.

Andrews, Stephen H J, Jerome B Rattner, Nigel G Shrive, and Janet L Ronsky. 2015. “Swelling Significantly Affects the Material Properties of the Menisci in Compression.” *Journal of Biomechanics* 48 (8): 1485–89. https://doi.org/10.1016/j.jbiomech.2015.02.001.

Andriotis, O. G., S. W. Chang, M. Vanleene, P. H. Howarth, D. E. Davies, S. J. Shefelbine, M. J. Buehler, and P. J. Thurner. 2015. “Structure-Mechanics Relationships of Collagen Fibrils in the Osteogenesis Imperfecta Mouse Model.” *Journal of the Royal Society Interface* 12 (111). https://doi.org/10.1098/rsif.2015.0701.

Arbab-Zadeh, Armin, and Valentin Fuster. 2019. “From Detecting the Vulnerable Plaque to Managing the Vulnerable Patient.” *Journal of the American College of Cardiology* 74 (12): 1582–93. https://doi.org/10.1016/j.jacc.2019.07.062.

Bakhach, Joseph. 2009. “The Cryopreservation of Composite Tissues.” *Organogenesis* 5 (3): 119–26. https://doi.org/10.4161/org.5.3.9583.

Balligand, J.-L., O. Feron, and C. Dessy. 2009. “ENOS Activation by Physical Forces: From Short-Term Regulation of Contraction to Chronic Remodeling of Cardiovascular Tissues.” *Physiological Reviews* 89 (2): 481–534. https://doi.org/10.1152/physrev.00042.2007.

Barrett, Hilary E., Kim Van der Heiden, Eric Farrell, Frank J.H. Gijsen, and Ali C. Akyildiz.

2019. “Calcifications in Atherosclerotic Plaques and Impact on Plaque Biomechanics.” *Journal of Biomechanics* 87: 1–12. https://doi.org/10.1016/j.jbiomech.2019.03.005.
Barrett, S. R.H., M. P.F. Sutcliffe, S. Howarth, Z. Y. Li, and J. H. Gillard. 2009. “Experimental Measurement of the Mechanical Properties of Carotid Atherothrombotic Plaque Fibrous Cap.” *Journal of Biomechanics* 42 (11): 1650–55. https://doi.org/10.1016/j.jbiomech.2009.04.025.
Beenakker, Jan Willem M., Brian A. Ashcroft, Jan H.N. Lindeman, and Tjerk H. Oosterkamp. 2012. “Mechanical Properties of the Extracellular Matrix of the Aorta Studied by Enzymatic Treatments.” *Biophysical Journal* 102 (8): 1731–37. https://doi.org/10.1016/j.bpj.2012.03.041.
Bentzon, Jacob Fog, Fumiyuki Otsuka, Renu Virmani, and Erling Falk. 2014. “Mechanisms of Plaque Formation and Rupture.” *Circulation Research* 114 (12): 1852–66. https://doi.org/10.1161/CIRCRESAHA.114.302721.
Bhatnagar, Prachi, Kremlin Wickramasinghe, Elizabeth Wilkins, and Nick Townsend. 2016. “Trends in the Epidemiology of Cardiovascular Disease in the UK.” *Heart* 102: 1945–52. https://doi.org/10.1136/heartjnl-2016-309573.
Bilodeau, G. G. 1992. “Regular Pyramid Punch Problem.” *Journal of Applied Mechanics, Transactions ASME* 59 (3): 519–23. https://doi.org/10.1115/1.2893754.
Bongiorno, Tom, Jena L. Chojnowski, James D. Lauderdale, and Todd Sulchek. 2016. “Cellular Stiffness as a Novel Stemness Marker in the Corneal Limbus.” *Biophysical Journal* 111 (8): 1761–72. https://doi.org/10.1016/j.bpj.2016.09.005.
Bourantas, Christos V., Farouc A. Jaffer, Frank J. Gijsen, Gijs Van Soest, Sean P. Madden, Brian K. Courtney, Ali M. Fard, et al. 2017. “Hybrid Intravascular Imaging: Recent Advances, Technical Considerations, and Current Applications in the Study of Plaque Pathophysiology.” *European Heart Journal* 38 (6): 400-412b. https://doi.org/10.1093/eurheartj/ehw097.
Bourantas, Christos V., Erhan Tenekecioglu, Maria Radu, Lorenz Räber, and Patrick W. Serruys. 2017. “State of the Art: Role of Intravascular Imaging in the Evolution of Percutaneous Coronary Intervention - A 30-Year Review.” *EuroIntervention* 13 (6): 644–53. https://doi.org/10.4244/EIJ-D-17-00471.
Brown, Adam J., Daniel R. Obaid, Charis Costopoulos, Richard A. Parker, Patrick A. Calvert, Zhongzhao Teng, Stephen P. Hoole, Nick E.J. West, Martin Goddard, and Martin R. Bennett. 2015. “Direct Comparison of Virtual-Histology Intravascular Ultrasound and Optical Coherence Tomography Imaging for Identification of Thin-Cap Fibroatheroma.” *Circulation: Cardiovascular Imaging* 8 (10): 1–10. https://doi.org/10.1161/CIRCIMAGING.115.003487.
Brown, Adam J., Zhongzhao Teng, Patrick A. Calvert, Nikil K. Rajani, Orla Hennessy, Nitesh Nerlekar, Daniel R. Obaid, et al. 2016. “Plaque Structural Stress Estimations Improve Prediction of Future Major Adverse Cardiovascular Events after Intracoronary Imaging.” *Circulation: Cardiovascular Imaging* 9 (6): 1–9. https://doi.org/10.1161/CIRCIMAGING.115.004172.
Brown, Adam J., Zhongzhao Teng, Paul C. Evans, Jonathan H. Gillard, Habib Samady, and Martin R. Bennett. 2016. “Role of Biomechanical Forces in the Natural History of Coronary Atherosclerosis.” *Nature Reviews Cardiology* 13 (4): 210–20. https://doi.org/10.1038/nrcardio.2015.203.
Brugaletta, Salvatore, Hector M. Garcia-Garcia, Patrick W. Serruys, Sanneke De Boer, Jurgen Ligthart, Josep Gomez-Lara, Karen Witberg, et al. 2011. “NIRS and IVUS for Characterization of Atherosclerosis in Patients Undergoing Coronary Angiography.” *JACC: Cardiovascular Imaging* 4 (6): 647–55. https://doi.org/10.1016/j.jcmg.2011.03.013.
Budday, Silvia, Timothy C. Ovaert, Gerhard A. Holzapfel, Paul Steinmann, and Ellen Kuhl. 2019. *Fifty Shades of Brain: A Review on the Mechanical Testing and Modeling of Brain Tissue*. *Archives of Computational Methods in Engineering*. Vol. 27. Springer Netherlands. https://doi.org/10.1007/s11831-019-09352-w.
Butt, H. J., and M. Jaschke. 1995. “Calculation of Thermal Noise in Atomic Force

Microscopy." *Nanotechnology* 6 (1): 1–7. https://doi.org/10.1088/0957-4484/6/1/001.
Butt, Hans Jürgen, Brunero Cappella, and Michael Kappl. 2005. "Force Measurements with the Atomic Force Microscope: Technique, Interpretation and Applications." *Surface Science Reports* 59 (1–6): 1–152. https://doi.org/10.1016/j.surfrep.2005.08.003.
Cardamone, L., A. Valentin, J. F. Eberth, and J. D. Humphrey. 2009. "Origin of Axial Prestretch and Residual Stress in Arteries." *Biomech Model Mechanobiol* 6 (8). https://doi.org/10.1097/MPG.0b013e3181a15ae8.Screening.
Cárdenas-Pérez, Stefany, José Jorge Chanona-Pérez, Juan Vicente Méndez-Méndez, Israel Arzate-Vázquez, Josué David Hernández-Varela, and Norma Güemes Vera. 2019. "Recent Advances in Atomic Force Microscopy for Assessing the Nanomechanical Properties of Food Materials." *Trends in Food Science and Technology* 87 (December 2017): 59–72. https://doi.org/10.1016/j.tifs.2018.04.011.
Cardoso, Luis, and Sheldon Weinbaum. 2014. "Changing Views of the Biomechanics of Vulnerable Plaque Rupture: A Review." *Ann Biomed Eng* 42 (2): 415–31. https://doi.org/10.1007/s10439-013-0855-x.
Caro, C G. 2009. "Discovery of the Role of Wall Shear in Atherosclerosis." *Arterioscler Thromb Vasc Biol* 29: 158–62. https://doi.org/10.1161/ATVBAHA.108.166736.
Caro, C G, J M Fitz-Gerald, and R C Schroeter. 1971. "Atheroma and Arterial Wall Shear - Observation, Correlation and Proposal of a Shear Dependent Mass Transfer Mechanism for Atherogenesis." *Proc Roy Soc Lond* 177.
Chai, Chen Ket, Ali C. Akyildiz, Lambert Speelman, Frank J.H. Gijsen, Cees W.J. Oomens, Marc R.H.M. van Sambeek, Aad van der Lugt, and Frank P.T. Baaijens. 2013. "Local Axial Compressive Mechanical Properties of Human Carotid Atherosclerotic Plaques-Characterisation by Indentation Test and Inverse Finite Element Analysis." *Journal of Biomechanics* 46 (10): 1759–66. https://doi.org/10.1016/j.jbiomech.2013.03.017.
Chai, Chen Ket, Lambert Speelman, Cees W.J. Oomens, and Frank P.T. Baaijens. 2014. "Compressive Mechanical Properties of Atherosclerotic Plaques - Indentation Test to Characterise the Local Anisotropic Behaviour." *Journal of Biomechanics* 47 (4): 784–92. https://doi.org/10.1016/j.jbiomech.2014.01.018.
Chang, Zhuo, Paolo Paoletti, Steve D. Barrett, Ya Hua Chim, Eva Caamaño-Gutiérrez, Maria Lyck Hansen, Hans Christian Beck, Lars Melholt Rasmussen, and Riaz Akhtar. 2018. "Nanomechanics and Ultrastructure of the Internal Mammary Artery Adventitia in Patients with Low and High Pulse Wave Velocity." *Acta Biomaterialia* 73: 437–48. https://doi.org/10.1016/j.actbio.2018.04.036.
Chang, Zhuo, Paolo Paoletti, Maria Lyck Hansen, Hans Christian Beck, Po Yu Chen, Lars Melholt Rasmussen, Riaz Akhtar, and Andreas Stylianou. 2018. "AFM Characterization of the Internal Mammary Artery as a Novel Target for Arterial Stiffening." *Scanning* 2018. https://doi.org/10.1155/2018/6340425.
Chatzizisis, Yiannis S., Aaron B. Baker, Galina K. Sukhova, Konstantinos C. Koskinas, Michail I. Papafaklis, Roy Beigel, Michael Jonas, et al. 2011. "Augmented Expression and Activity of Extracellular Matrix-Degrading Enzymes in Regions of Low Endothelial Shear Stress Colocalize with Coronary Atheromata with Thin Fibrous Caps in Pigs." *Circulation* 123 (6): 621–30. https://doi.org/10.1161/CIRCULATIONAHA.110.970038.
Chatzizisis, Yiannis S., Ahmet Umit Coskun, Michael Jonas, Elazer R. Edelman, Charles L. Feldman, and Peter H. Stone. 2007. "Role of Endothelial Shear Stress in the Natural History of Coronary Atherosclerosis and Vascular Remodeling. Molecular, Cellular, and Vascular Behavior." *JACC* 49 (25): 2379–93. https://doi.org/10.1016/j.jacc.2007.02.059.
Chen, H., and G. S. Kassab. 2017. "Microstructure-Based Constitutive Model of Coronary Artery with Active Smooth Muscle Contraction." *Scientific Reports* 7 (1): 1–15. https://doi.org/10.1038/s41598-017-08748-7.
Chen, Huan, and Ghassan S. Kassab. 2016. "Microstructure-Based Biomechanics of Coronary Arteries in Health and Disease." *Journal of Biomechanics* 49 (12): 2548–59. https://doi.org/10.1016/j.jbiomech.2016.03.023.
Chen, Huan, Yi Liu, Mikhail N. Slipchenko, Xuefeng Zhao, Ji Xin Cheng, and Ghassan S. Kassab. 2011. "The Layered Structure of Coronary Adventitia under Mechanical Load."

Biophysical Journal 101 (11): 2555–62. https://doi.org/10.1016/j.bpj.2011.10.043.
Chen, Huan, Tong Luo, Xuefeng Zhao, Xiao Lu, Yunlong Huo, and Ghassan S. Kassab. 2013. “Microstructural Constitutive Model of Active Coronary Media.” *Biomaterials* 34 (31): 7575–83. https://doi.org/10.1016/j.biomaterials.2013.06.035.
Cheng, Caroline, Rien Van Haperen, Monique De Waard, Luc C.A. Van Damme, Dennie Tempel, Laurens Hanemaaijer, Gert W.A. Van Cappellen, et al. 2005. “Shear Stress Affects the Intracellular Distribution of ENOS: Direct Demonstration by a Novel in Vivo Technique.” *Blood* 106 (12): 3691–98. https://doi.org/10.1182/blood-2005-06-2326.
Cheng, G. C., H. M. Loree, R. D. Kamm, M. C. Fishbein, and R. T. Lee. 1993a. “Distribution of Circumferential Stress in Ruptured and Stable Atherosclerotic Lesions: A Structural Analysis with Histopathological Correlation.” *Circulation* 87 (4): 1179–87. https://doi.org/10.1161/01.CIR.87.4.1179.
Cheng, G C, H M Loree, R D Kamm, M C Fishbein, and R T Lee. 1993b. “Distribution of Circumferential Stress in Ruptured and Stable Atherosclerotic Lesions. A Structural Analysis with Histopathological Correlation.” *Circulation* 87 (4): 1179–87. https://doi.org/10.1161/01.CIR.87.4.1179.
Chien, Shu. 2007. “Mechanotransduction and Endothelial Cell Homeostasis: The Wisdom of the Cell.” *American Journal of Physiology - Heart and Circulatory Physiology* 292 (3). https://doi.org/10.1152/ajpheart.01047.2006.
Chiu, J. J., and S. Chien. 2011. “Effects of Disturbed Flow on Vascular Endothelium: Pathophysiological Basis and Clinical Perspectives.” *Physiol Rev* 91 (1). https://doi.org/10.1152/physrev.00047.2009.Effects.
Chuong, C J, and Y C Fung. 1986. “On Residual Stresses in Arteries.” *J Biomech Eng* 108 (May 1986): 189–92.
Clark, John M, and Seymour Glagov. 1985. “Transmural Organization of the Arterial Media The Lamellar Unit Revisited.” *Arteriosclerosis, Thrombosis, and Vascular Biology* 5 (1): 19–34. https://doi.org/10.1161/01.ATV.5.1.19.
Connell, Mary K O, Sushila Murthy, Samson Phan, Chengpei Xu, Joann Buchanan, Ryan Spilker, Ronald L Dalman, Christopher K Zarins, Winfried Denk, and Charles A Taylor. 2008. “The Three-Dimensional Micro- and Nanostructure of the Aortic Medial Lamellar Unit Measured Using 3D Confocal and Electron Microscopy Imaging.” *Matrix Biol* 27: 171–81. https://doi.org/10.1016/j.matbio.2007.10.008.
Costopoulos, Charis, Akiko Maehara, Yuan Huang, Adam J. Brown, Jonathan H. Gillard, Zhongzhao Teng, Gregg W. Stone, and Martin R. Bennett. 2020. “Heterogeneity of Plaque Structural Stress Is Increased in Plaques Leading to MACE: Insights From the PROSPECT Study.” *JACC: Cardiovascular Imaging* 13 (5). https://doi.org/10.1016/j.jcmg.2019.05.024.
Costopoulos, Charis, Lucas H. Timmins, Yuan Huang, Olivia Y. Hung, David S. Molony, Adam J. Brown, Emily L. Davis, et al. 2019. “Impact of Combined Plaque Structural Stress and Wall Shear Stress on Coronary Plaque Progression, Regression, and Changes in Composition.” *European Heart Journal* 40 (18): 1411–22. https://doi.org/10.1093/eurheartj/ehz132.
Dalager, Søren, William P. Paaske, Ingrid Bayer Kristensen, Jacob Marsvin Laurberg, and Erling Falk. 2007. “Artery-Related Differences in Atherosclerosis Expression: Implications for Atherogenesis and Dynamics in Intima-Media Thickness.” *Stroke* 38 (10): 2698–2705. https://doi.org/10.1161/STROKEAHA.107.486480.
Darling, E. M., S. Zauscher, and F. Guilak. 2006. “Viscoelastic Properties of Zonal Articular Chondrocytes Measured by Atomic Force Microscopy.” *Osteoarthritis and Cartilage* 14 (6): 571–79. https://doi.org/10.1016/j.joca.2005.12.003.
Davies, Peter F. 2009. “Hemodynamic Shear Stress and the Endothelium in Cardiovascular Pathophysiology.” *Nature Clinical Practice Cardiovascular Medicine* 6 (1): 16–26. https://doi.org/10.1038/ncpcardio1397.
Dayan, D., Y. Hiss, A. Hirshberg, J. J. Bubis, and M. Wolman. 1989. “Are the Polarization Colors of Picrosirius Red-Stained Collagen Determined Only by the Diameter of the Fibers?” *Histochemistry* 93 (1): 27–29. https://doi.org/10.1007/BF00266843.

Delfino, A, N Stergiopulos, J E Moore, and J J Meister. 1997. “Residual Strain Effects on the Stress Field in a Thick Wall Finite Element Model of the Human Carotid Bifurcation.” *J Biomech* 30 (8): 777–86. https://doi.org/Doi: 10.1016/s0021-9290(97)00025-0.

Demicheva, Elena, Markus Hecker, and Thomas Korff. 2008. “Stretch-Induced Activation of the Transcription Factor Activator Protein-1 Controls Monocyte Chemoattractant Protein-1 Expression during Arteriogenesis.” *Circulation Research* 103 (5): 477–84. https://doi.org/10.1161/CIRCRESAHA.108.177782.

Devireddy, R A M V, D Ph, Michael R Neidert, John C Bischof Ph D, and Robert T Tranquillo. 2003. “Cryopreservation of Collagen-Based Tissue Equivalents I. Effect of Freezing in the Absence of Cryoprotective Agents.” *Tiss Eng* 9 (6).

Dimitriadis, Emilios K., Ferenc Horkay, Julia Maresca, Bechara Kachar, and Richard S. Chadwick. 2002. “Determination of Elastic Moduli of Thin Layers of Soft Material Using the Atomic Force Microscope.” *Biophysical Journal* 82 (5): 2798–2810. https://doi.org/10.1016/S0006-3495(02)75620-8.

Ding, Zhaohua, Hui Zhu, and Morton H. Friedman. 2002. “Coronary Artery Dynamics in Vivo.” *Annals of Biomedical Engineering* 30 (4): 419–29. https://doi.org/10.1114/1.1467925.

Dingemans, Koert P., Peter Teeling, Jaap H. Lagendijk, and Anton E. Becker. 2000. “Extracellular Matrix of the Human Aortic Media: An Ultrastructural Histochemical and Immunohistochemical Study of the Adult Aortic Media.” *The Anatomical Record* 258 (1): 1–14. https://doi.org/10.1002/(SICI)1097-0185(20000101)258:1<1::AID-AR1>3.0.CO;2-7.

Do, Anh-vu, Behnoush Khorsand, Sean M Geary, Aliasger K Salem, Experimental Therapeutics, and Iowa City. 2015. “3D Printing of Scaffolds for Tissue Regeneration Applications.” *Adv Healthc Mater* 4 (12): 1742–62. https://doi.org/10.1002/adhm.201500168.3D.

Douglas, Graeham R., Adam J. Brown, Jonathan H. Gillard, Martin R. Bennett, Michael P.F. Sutcliffe, and Zhongzhao Teng. 2017. “Impact of Fiber Structure on the Material Stability and Rupture Mechanisms of Coronary Atherosclerotic Plaques.” *Annals of Biomedical Engineering* 45 (6): 1462–74. https://doi.org/10.1007/s10439-017-1827-3.

Drifka, Cole R., Agnes G. Loeffler, Kara Mathewson, Guneet Mehta, Adib Keikhosravi, Yuming Liu, Stephanie Lemancik, et al. 2016. “Comparison of Picrosirius Red Staining With Second Harmonic Generation Imaging for the Quantification of Clinically Relevant Collagen Fiber Features in Histopathology Samples.” *Journal of Histochemistry and Cytochemistry* 64 (9): 519–29. https://doi.org/10.1369/0022155416659249.

Ebenstein, Donna M., Dezba Coughlin, Joan Chapman, Cheng Li, and Lisa A. Pruitt. 2009. “Nanomechanical Properties of Calcification, Fibrous Tissue, and Hematoma from Atherosclerotic Plaques.” *Journal of Biomedical Materials Research - Part A* 91 (4): 1028–37. https://doi.org/10.1002/jbm.a.32321.

Eshtehardi, Parham, Adam J. Brown, Ankit Bhargava, Charis Costopoulos, Olivia Y. Hung, Michel T. Corban, Hossein Hosseini, Bill D. Gogas, Don P. Giddens, and Habib Samady. 2017. “High Wall Shear Stress and High-Risk Plaque: An Emerging Concept.” *International Journal of Cardiovascular Imaging* 33 (7): 1089–99. https://doi.org/10.1007/s10554-016-1055-1.

Falk, Erling. 1992. “Why Do Plaques Rupture ?” *Circulation* 86 (6): 30–42.

———. 2006. “Pathogenesis of Atherosclerosis.” *J Am Coll Cardiol* 47 (8 Suppl C): 0–5. https://doi.org/10.1016/j.jacc.2005.09.068.

Falk, Erling, Masataka Nakano, Jacob Fog Bentzon, Aloke V. Finn, and Renu Virmani. 2013a. “Update on Acute Coronary Syndromes: The Pathologists’ View.” *European Heart Journal* 34: 719–28. https://doi.org/10.1093/eurheartj/ehs411.

———. 2013b. “Update on Acute Coronary Syndromes: The Pathologists’ View.” *European Heart Journal* 34 (10): 719–28. https://doi.org/10.1093/eurheartj/ehs411.

Falk, Erling, Prediman K. Shah, and Valentin Fuster. 1995. “Coronary Plaque Disruption.” *Circulation* 92 (3): 657–71. https://doi.org/10.1161/01.CIR.92.3.657.

Finet, Gérard, Jacques Ohayon, and Gilles Rioufol. 2004. “Biomechanical Interaction

between Cap Thickness, Lipid Core Composition and Blood Pressure in Vulnerable Coronary Plaque: Impact on Stability or Instability." *Coronary Artery Dis* 15 (1): 13–20. https://doi.org/10.1097/00019501-200402000-00003.
Finn, Aloke V., Masataka Nakano, Jagat Narula, Frank D. Kolodgie, and Renu Virmani. 2010. "Concept of Vulnerable/Unstable Plaque." *Arterioscler Thromb Vasc Biol* 30 (7): 1282–92. https://doi.org/10.1161/ATVBAHA.108.179739.
Fomovsky, Gregory M., Stavros Thomopoulos, and Jeffrey W. Holmes. 2010. "Contribution of Extracellular Matrix to the Mechanical Properties of the Heart." *Journal of Molecular and Cellular Cardiology* 48 (3): 490–96. https://doi.org/10.1016/j.yjmcc.2009.08.003.
Frangos, Spiros G, Vivian Gahtan, and Sumpio Bauer. 1999. "Localization of Atherosclerosis." *Arch Surg* 134: 1142–49.
Fratzl, Peter. 2008. *Collagen: Structure and Mechanics*. *Springer*. Vol. 39. Springer.
Fuster, Valentin, and Bryony M. Mearns. 2009. "The CVD Paradox: Mortality vs Prevalence." *Nature Reviews Cardiology* 6 (11): 669. https://doi.org/10.1038/nrcardio.2009.187.
Gambillara, Veronica, Céline Chambaz, Gabriela Montorzi, Sylvain Roy, Nikos Stergiopulos, and Paolo Silacci. 2006. "Plaque-Prone Hemodynamics Impair Endothelial Function in Pig Carotid Arteries." *American Journal of Physiology - Heart and Circulatory Physiology* 290 (6): 2320–28. https://doi.org/10.1152/ajpheart.00486.2005.
Gasser, T. Christian, Ray W. Ogden, and Gerhard A. Holzapfel. 2006. "Hyperelastic Modelling of Arterial Layers with Distributed Collagen Fibre Orientations." *Journal of the Royal Society Interface* 3 (6): 15–35. https://doi.org/10.1098/rsif.2005.0073.
Gautier, Hélène O.B., Amelia J. Thompson, Sarra Achouri, David E. Koser, Kathrin Holtzmann, Emad Moeendarbary, and Kristian Franze. 2015. "Atomic Force Microscopy-Based Force Measurements on Animal Cells and Tissues." In *Methods in Cell Biology*, 125:211–35. https://doi.org/10.1016/bs.mcb.2014.10.005.
Gavara, Núria. 2017. "A Beginner's Guide to Atomic Force Microscopy Probing for Cell Mechanics." *Microscopy Research and Technique* 80 (1): 75–84. https://doi.org/10.1002/jemt.22776.
Gavara, Núria, and Richard S. Chadwick. 2013. "Determination of the Elastic Moduli of Thin Samples and Adherent Cells Using Conical AFM Tips." *Nature Nanotechnology* 7 (11): 733–36. https://doi.org/10.1038/nnano.2012.163.Determination.
Getz, Godfrey S., and Catherine A. Reardon. 2012. "Animal Models of Atherosclerosis." *Arteriosclerosis, Thrombosis, and Vascular Biology* 32 (5): 1104–15. https://doi.org/10.1161/ATVBAHA.111.237693.
Gijsen, Frank J.H., Jolanda J. Wentzel, Attila Thury, Frits Mastik, Johannes A. Schaar, Johan C.H. Schuurbiers, Cornelis J. Slager, et al. 2008. "Strain Distribution over Plaques in Human Coronary Arteries Relates to Shear Stress." *American Journal of Physiology - Heart and Circulatory Physiology* 295 (4): 1608–14. https://doi.org/10.1152/ajpheart.01081.2007.
Gijsen, Frank, Yuki Katagiri, Peter Barlis, Christos Bourantas, Carlos Collet, Umit Coskun, Joost Daemen, et al. 2019. "Expert Recommendations on the Assessment of Wall Shear Stress in Human Coronary Arteries: Existing Methodologies, Technical Considerations, and Clinical Applications." *European Heart Journal* 40 (41): 3421–33. https://doi.org/10.1093/eurheartj/ehz551.
Glagov, Seymour, Raymond P Vito, Don P. Giddens, and Christopher K Zarins. 1992. "Microarchitecture and Composition of Artery Wall: Relationship to Location, Diameter and the Distribution of Mechanical Stress." *J Hypertens* 10.
Glass, Christopher, and Joseph Witztum. 2001. "Atherosclerosis: The Road Ahead." *Cell* 104: 503–16. https://doi.org/10.1177/000331978503601001.
Goettsch, Claudia, Winfried Goettsch, Alexander Arsov, Lorenz C Hofbauer, Stefan R Bornstein, and Henning Morawietz. 2009. "Long-Term Cyclic Strain Downregulates Endothelial Nox4." *Antioxid Redox Sign* 11 (10): 2385–97. https://doi.org/10.1089/ARS.2009.2561.
Gosline, J., M. Lillie, E. Carrington, P. Guerette, C. Ortlepp, and K. Savage. 2002. "Elastic Proteins: Biological Roles and Mechanical Properties." *Philosophical Transactions of the*

Royal Society B: Biological Sciences 357 (1418): 121–32. https://doi.org/10.1098/rstb.2001.1022.
Grant, Colin A., David J. Brockwell, Sheena E. Radford, and Neil H. Thomson. 2008. “Effects of Hydration on the Mechanical Response of Individual Collagen Fibrils.” *Applied Physics Letters* 92 (23). https://doi.org/10.1063/1.2937001.
Grant, Colin A., and Peter C. Twigg. 2013. “Pseudostatic and Dynamic Nanomechanics of the Tunica Adventitia in Elastic Arteries Using Atomic Force Microscopy.” *ACS Nano* 7 (1): 456–64. https://doi.org/10.1021/nn304508x.
Groen, Harald C., Frank J H Gijsen, Aad Van Der Lugt, Marina S. Ferguson, Thomas S. Hatsukami, Anton F W Van Der Steen, Chun Yuan, and Jolanda J. Wentzel. 2007. “Plaque Rupture in the Carotid Artery Is Localized at the High Shear Stress Region: A Case Report.” *Stroke* 38 (8): 2379–81. https://doi.org/10.1161/STROKEAHA.107.484766.
Guo, Xiaoya, Don P. Giddens, David Molony, Chun Yang, Habib Samady, Jie Zheng, Mitsuaki Matsumura, et al. 2019. “A Multimodality Image-Based Fluid–Structure Interaction Modeling Approach for Prediction of Coronary Plaque Progression Using IVUS and Optical Coherence Tomography Data With Follow-Up.” *Journal of Biomechanical Engineering* 141 (9): 1–9. https://doi.org/10.1115/1.4043866.
Harrison, David, Kathy K Griendling, Ulf Landmesser, Burkhard Hornig, and Helmut Drexler. 2003. “Role of Oxidative Stress in Atherosclerosis.” *Am J Cardiol* 91 (3): 7–11. https://doi.org/10.1016/S0002-9149(02)03144-2.
Hayenga, H. N., A. Trache, J. Trzeciakowski, and J. D. Humphrey. 2011. “Regional Atherosclerotic Plaque Properties in ApoE-/-Mice Quantified by Atomic Force, Immunofluorescence, and Light Microscopy.” *Journal of Vascular Research* 48 (6): 495–504. https://doi.org/10.1159/000329586.
He, Yong, FeiFei Yang, HaiMing Zhao, Qing Gao, Bing Xia, and JianZhong Fu. 2016. “Research on the Printability of Hydrogels in 3D Bioprinting.” *Sci Rep* 6 (1): 29977. https://doi.org/10.1038/srep29977.
Hemmasizadeh, Ali, Kurosh Darvish, and Michael Autieri. 2012. “Characterization of Changes to the Mechanical Properties of Arteries Due to Cold Storage Using Nanoindentation Tests.” *Ann Biomed Eng* 40 (7): 1434–42. https://doi.org/10.1007/s10439-011-0506-z.
Hemmasizadeh, Ali, Alkiviadis Tsamis, Rabee Cheheltani, Soroush Assari, Antonio D’Amore, Michael Autieri, Mohammad F. Kiani, et al. 2015. “Correlations between Transmural Mechanical and Morphological Properties in Porcine Thoracic Descending Aorta.” *Journal of the Mechanical Behavior of Biomedical Materials* 47: 12–20. https://doi.org/10.1016/j.jmbbm.2015.03.004.
Hertz, H. 1881. “H. Hertz, Über Die Berührung Fester Elastischer Körper, Journal Für Die Reine Und Angewandte Mathematik 92, 156-171 (1881).” *Journal Für Die Reine Und Angewandte Mathematik* 171: 156–71.
Himburg, H. A., Deborah M Grzybowski, Andrew L Hazel, Jeffrey A Lamack, Xue-mei Li, and Morton H Friedman. 2004. “Spatial Comparison between Wall Shear Stress Measures and Porcine Arterial Endothelial Permeability.” *AJP: Heart Circ Physiol* 286 (5): H1916–22. https://doi.org/10.1152/ajpheart.00897.2003.
Hishikawa, Keiichi, Barry S. Oemar, Zhihong Yang, and Thomas F. Lüscher. 1997. “Pulsatile Stretch Stimulates Superoxide Production and Activates Nuclear Factor-Kb in Human Coronary Smooth Muscle.” *Circulation Research* 81 (5): 797–803. https://doi.org/10.1161/01.RES.81.5.797.
Holzapfel, G. A., and R. W. Ogden. 2010. “Constitutive Modelling of Arteries.” *Proc Roy Soc A: Math Phys Eng Sci* 466 (2118): 1551–97. https://doi.org/10.1098/rspa.2010.0058.
Holzapfel, Gerhard A., Thomas C. Gasser, and Ray W. Ogden. 2000. “A New Constitutive Framework for Arterial Wall Mechanics and a Comparative Study of Material Models.” *J Elasticity* 61 (1–3): 1–48. https://doi.org/10.1023/A:1010835316564.
Holzapfel, Gerhard A., John J. Mulvihill, Eoghan M. Cunnane, and Michael T. Walsh. 2014. “Computational Approaches for Analyzing the Mechanics of Atherosclerotic Plaques: A

Review.” *J Biomech* 47 (4): 859–69. https://doi.org/10.1016/j.jbiomech.2014.01.011.
Holzapfel, Gerhard a., and Ray W Ogden. 2010. “Modelling the Layer-Specific Three-Dimensional Residual Stresses in Arteries, with an Application to the Human Aorta.” *J R Soc Interface* 7 (46): 787–99. https://doi.org/10.1098/rsif.2009.0357.
Holzapfel, Gerhard A., Gerhard Sommer, Christian T. Gasser, and Peter Regitnig. 2005. “Determination of Layer-Specific Mechanical Properties of Human Coronary Arteries with Nonatherosclerotic Intimal Thickening and Related Constitutive Modeling.” *Am J Physiol Heart Circ Physiol*, no. 289: 2048–58. https://doi.org/10.1152/ajpheart.00934.2004.
Holzapfel, Gerhard A., Michael Stadler, and Thomas C. Gasser. 2005. “Changes in the Mechanical Environment of Stenotic Arteries during Interaction with Stents: Computational Assessment of Parametric Stent Designs.” *Journal of Biomechanical Engineering* 127 (1): 166–80. https://doi.org/10.1115/1.1835362.
Hwang, Juliana, Michael H. Ing, Adler Salazar, Bernard Lassègue, Kathy Griendling, Mohamad Navab, Alex Sevanian, and Tzung K. Hsiai. 2003. “Pulsatile Versus Oscillatory Shear Stress Regulates NADPH Oxidase Subunit Expression: Implication for Native LDL Oxidation.” *Circulation Research* 93 (12): 1225–32. https://doi.org/10.1161/01.RES.0000104087.29395.66.
Johnson, K. L., K. Kendall, and A.D. Roberts. 1971. “Surface Energy and the Contact of Elastic Solids.” *Proceedings of the Royal Society of London. A. Mathematical and Physical Sciences* 324 (1558): 301–13. https://doi.org/10.1098/rspa.1971.0141.
Johnston, Robert D., Robert T. Gaul, and Caitríona Lally. 2021. “An Investigation into the Critical Role of Fibre Orientation in the Ultimate Tensile Strength and Stiffness of Human Carotid Plaque Caps.” *Acta Biomaterialia* 124: 291–300. https://doi.org/10.1016/j.actbio.2021.02.008.
Jufri, Nurul F, Abidali Mohamedali, Alberto Avolio, and Mark S Baker. 2015. “Mechanical Stretch: Physiological and Pathological Implications for Human Vascular Endothelial Cells.” *Vascular Cell* 7: 8. https://doi.org/10.1186/s13221-015-0033-z.
Junhee Seok, H. Shaw Warren, G. Cuenca Alex, N. Mindrinos Michael, V. Baker Henry, Weihong Xu, Daniel R. Richards, et al. 2013. “Genomic Responses in Mouse Models Poorly Mimic Human Inflammatory Diseases.” *Proceedings of the National Academy of Sciences of the United States of America* 110 (9): 3507–12. https://doi.org/10.1073/pnas.1222878110.
Junqueira, L. C.U., G. Bignolas, and R. R. Brentani. 1979. “Picrosirius Staining plus Polarization Microscopy, a Specific Method for Collagen Detection in Tissue Sections.” *The Histochemical Journal* 11 (4): 447–55. https://doi.org/10.1007/BF01002772.
Kelly-Arnold, A., N. Maldonado, D. Laudier, E. Aikawa, L. Cardoso, and S. Weinbaum. 2013. “Revised Microcalcification Hypothesis for Fibrous Cap Rupture in Human Coronary Arteries.” *Proc Natl Acad Sci USA* 110 (26): 10741–46. https://doi.org/10.1073/pnas.1308814110.
Kenjeres, S., and A. de Loor. 2013. “Modelling and Simulation of Low-Density Lipoprotein Transport through Multi-Layered Wall of an Anatomically Realistic Carotid Artery Bifurcation.” *Journal of The Royal Society Interface* 11 (91): 20130941–20130941. https://doi.org/10.1098/rsif.2013.0941.
Kim, H. J., I. E. Vignon-Clementel, J. S. Coogan, C. A. Figueroa, K. E. Jansen, and C. A. Taylor. 2010. “Patient-Specific Modeling of Blood Flow and Pressure in Human Coronary Arteries.” *Annals of Biomedical Engineering* 38 (10): 3195–3209. https://doi.org/10.1007/s10439-010-0083-6.
Kobayashi, Satoshi, Masato Nagino, Shunichiro Komatsu, Keiji Naruse, Yuji Nimura, Makoto Nakanishi, and Masahiro Sokabe. 2003. “Stretch-Induced IL-6 Secretion from Endothelial Cells Requires NF-KB Activation.” *Biochemical and Biophysical Research Communications* 308 (2): 306–12. https://doi.org/10.1016/S0006-291X(03)01362-7.
Kok, Annette M., David S. Molony, Lucas H. Timmins, Yi-An Ko, Eric Boersma, Parham Eshtehardi, Jolanda J. Wentzel, and Habib Samady. 2019. “The Influence of Multidirectional Shear Stress on Plaque Progression and Composition Changes in

Human Coronary Arteries." *EuroIntervention* 15 (8): 692–99. https://doi.org/10.4244/eij-d-18-00529.
Kol, Nitzan, Yu Shi, Marianna Tsvitov, David Barlam, Roni Z. Shneck, Michael S. Kay, and Itay Rousso. 2007. "A Stiffness Switch in Human Immunodeficiency Virus." *Biophysical Journal* 92 (5): 1777–83. https://doi.org/10.1529/biophysj.106.093914.
Koskinas, Konstantinos C., Galina K. Sukhova, Aaron B. Baker, Michail I. Papafaklis, Yiannis S. Chatzizisis, Ahmet U. Coskun, Thibaut Quillard, et al. 2013a. "Thin-Capped Atheromata with Reduced Collagen Content in Pigs Develop in Coronary Arterial Regions Exposed to Persistently Low Endothelial Shear Stress." *Arteriosclerosis, Thrombosis, and Vascular Biology* 33 (7): 1494–1504. https://doi.org/10.1161/ATVBAHA.112.300827.
———. 2013b. "Thin-Capped Atheromata with Reduced Collagen Content in Pigs Develop in Coronary Arterial Regions Exposed to Persistently Low Endothelial Shear Stress." *Arterioscler Thromb Vasc Biol* 33 (7): 1494–1504. https://doi.org/10.1161/ATVBAHA.112.300827.
Koskinas, Konstantinos C, Yiannis S Chatzizisis, Aaron B Baker, Elazer R Edelman, Peter H Stone, and Charles L Feldman. 2009. "The Role of Low Endothelial Shear Stress in the Conversion of Atherosclerotic Lesions from Stable to Unstable Plaque." *Curr Opin Cardiol* 24 (6): 580–90. https://doi.org/10.1097/HCO.0b013e328331630b.
Krieg, Michael, Gotthold Fläschner, David Alsteens, Benjamin M. Gaub, Wouter H. Roos, Gijs J.L. Wuite, Hermann E. Gaub, Christoph Gerber, Yves F. Dufrêne, and Daniel J. Müller. 2019. "Atomic Force Microscopy-Based Mechanobiology." *Nature Reviews Physics* 1 (1): 41–57. https://doi.org/10.1038/s42254-018-0001-7.
Ku, David N, Don P Giddens, Christopher K Zarins, and Seymour Glagov. 1985. "Pulsatile Flow and Atherosclerosis in the Human Carotid Bifurcation Positive Correlation between Plaque Location and Low and Oscillating Shear Stress." *Arterioscler Thromb Vasc Biol* 5 (3).
Lally, C, A J Reid, and P J Prendergast. 2004. "Elastic Behavior of Porcine Coronary Artery Tissue under Uniaxial and Equibiaxial Tension." *Ann Biomed Eng* 32 (10): 1355–64.
Leach, Joseph R., Vitaliy L. Rayz, Bruno Soares, Max Wintermark, Mohammad R K Mofrad, and David Saloner. 2010. "Carotid Atheroma Rupture Observed in Vivo and FSI-Predicted Stress Distribution Based on Pre-Rupture Imaging." *Ann Biomed Eng* 38 (8): 2748–65. https://doi.org/10.1007/s10439-010-0004-8.
Lee, R T, a J Grodzinsky, E H Frank, R D Kamm, and F J Schoen. 1991. "Structure-Dependent Dynamic Mechanical Behavior of Fibrous Caps from Human Atherosclerotic Plaques." *Circulation* 83 (5): 1764–70. https://doi.org/10.1161/01.CIR.83.5.1764.
Lee, Richard T., Frederick J. Schoen, Howard M. Loree, Michael W. Lark, and Peter Libby. 1996. "Circumferential Stress and Matrix Metalloproteinase 1 in Human Coronary Atherosclerosis: Implications for Plaque Rupture." *Arteriosclerosis, Thrombosis, and Vascular Biology* 16 (8): 1070–73. https://doi.org/10.1161/01.ATV.16.8.1070.
Lehoux, S., Y. Castier, and A. Tedgui. 2006. "Molecular Mechanisms of the Vascular Responses to Haemodynamic Forces." *J Intern Med* 259 (4): 381–92. https://doi.org/10.1111/j.1365-2796.2006.01624.x.
Liang, Xuan, Michalis Xenos, Yared Alemu, Suraj H. Rambhia, Ifat Lavi, Ran Kornowski, Luis Gruberg, Shmuel Fuchs, Shmuel Einav, and Danny Bluestein. 2013. "Biomechanical Factors in Coronary Vulnerable Plaque Risk of Rupture: Intravascular Ultrasound-Based Patient-Specific Fluid-Structure Interaction Studies." *Coronary Artery Disease* 24 (2): 75–87. https://doi.org/10.1097/MCA.0b013e32835bbe99.
Libby, Peter. 2012. "Inflammation in Atherosclerosis." *Arterioscler Thromb Vasc Biol* 32: 2045–52. https://doi.org/10.1161/ATVBAHA.108.179705.
Libby, Peter, and Gerard Pasterkamp. 2015. "Requiem for the 'Vulnerable Plaque.'" *European Heart Journal* 36 (43): 2984–87. https://doi.org/10.1093/eurheartj/ehv349.
Lin, David C., David I. Shreiber, Emilios K. Dimitriadis, and Ferenc Horkay. 2009. "Spherical Indentation of Soft Matter beyond the Hertzian Regime: Numerical and Experimental Validation of Hyperelastic Models." *Biomechanics and Modeling in Mechanobiology* 8

(5): 345–58. https://doi.org/10.1007/s10237-008-0139-9.
Little, W. C., M. Constantinescu, R. J. Applegate, M. A. Kutcher, M. T. Burrows, F. R. Kahl, and W. P. Santamore. 1988. “Can Coronary Angiography Predict the Site of a Subsequent Myocardial Infarction in Patients with Mild-to-Moderate Coronary Artery Disease?” *Circulation* 78 (5 I): 1157–66. https://doi.org/10.1161/01.CIR.78.5.1157.
Loree, H. M., B. J. Tobias, L. J. Gibson, R. D. Kamm, D. M. Small, and R. T. Lee. 1994. “Mechanical Properties of Model Atherosclerotic Lesion Lipid Pools.” *Arteriosclerosis and Thrombosis* 14 (2): 230–34. https://doi.org/10.1161/01.atv.14.2.230.
Loree, Howard M., Roger D. Kamm, Richard G. Stringfellow, and Richard T. Lee. 1992. “Effects of Fibrous Cap Thickness on Peak Circumferential Stress in Model Atherosclerotic Vessels.” *Circulation Research* 71 (4): 850–58. https://doi.org/10.1161/01.RES.71.4.850.
Lu, D., and G. S. Kassab. 2011. “Role of Shear Stress and Stretch in Vascular Mechanobiology.” *Journal of The Royal Society Interface* 8 (63): 1379–85. https://doi.org/10.1098/rsif.2011.0177.
Mahmood, B, C Ewertsen, J Carlsen, and M B Nielsen. 2016. “Ultrasound Vascular Elastography as a Tool for Assessing Atherosclerotic Plaques – A Systematic Literature Review.” *Ultrasound Int*, 106–12.
Maldonado, N., A. Kelly-Arnold, Y. Vengrenyuk, D. Laudier, J. T. Fallon, R. Virmani, L. Cardoso, and S. Weinbaum. 2012. “A Mechanistic Analysis of the Role of Microcalcifications in Atherosclerotic Plaque Stability: Potential Implications for Plaque Rupture.” *Am J Physiol Heart Circ Physiol* 303 (5): 619–28. https://doi.org/10.1152/ajpheart.00036.2012.
Malek, Adel M, Seth L Alper, and Seigo Izumo. 1999. “Hemodynamic Shear Stress and Its Role in Atherosclerosis.” *JAMA* 282 (21): 2035–42.
Mantella, Laura Eve, Adrian Quan, and Subodh Verma. 2015. “Variability in Vascular Smooth Muscle Cell Stretch-Induced Responses in 2D Culture.” *Vascular Cell* 7 (1): 1–9. https://doi.org/10.1186/s13221-015-0032-0.
Mariappan, Yogesh K, Kevin J Glaser, and Richard L Ehman. 2010. “Magnetic Resonance Elastography: A Review.” *Clinical Anatomy* 23 (5): 497–511. https://doi.org/10.1002/ca.21006.MAGNETIC.
Mark, K. Von Der. 1981. “Localization of Collagen Types in Tissues.” *International Review of Connective Tissue Research* Vol. 9: 265–324. https://doi.org/10.1016/b978-0-12-363709-3.50012-7.
Marques, Koen M.J., Hugo J. Spruijt, Christa Boer, Nico Westerhof, Cees A. Visser, and Frans C. Visser. 2002. “The Diastolic Flow-Pressure Gradient Relation in Coronary Stenoses in Humans.” *Journal of the American College of Cardiology* 39 (10): 1630–36. https://doi.org/10.1016/S0735-1097(02)01834-X.
Masson, Ingrid, Anne Fialaire-Legendre, Caroline Godin, Pierre Boutouyrie, Philippe Bierling, and Mustapha Zidi. 2009. “Mechanical Properties of Arteries Cryopreserved at -80 °C and -150 °C.” *Med Eng Phys* 31 (7): 825–32. https://doi.org/10.1016/j.medengphy.2009.03.009.
Matsumoto, Takeo, Taisuke Goto, Takao Furukawa, and Masaaki Sato. 2004. “Residual Stress and Strain in the Lamellar Unit of the Porcine Aorta: Experiment and Analysis.” *Journal of Biomechanics* 37 (6): 807–15. https://doi.org/10.1016/j.jbiomech.2003.08.014.
McKee, Clayton T., Julie A. Last, Paul Russell, and Christopher J. Murphy. 2011. “Indentation versus Tensile Measurements of Young’s Modulus for Soft Biological Tissues.” *Tissue Engineering - Part B: Reviews* 17 (3): 155–64. https://doi.org/10.1089/ten.teb.2010.0520.
Mohamied, Yumnah, Ethan M. Rowland, Emma L. Bailey, Spencer J. Sherwin, Martin A. Schwartz, and Peter D. Weinberg. 2015. “Change of Direction in the Biomechanics of Atherosclerosis.” *Annals of Biomedical Engineering* 43 (1): 16–25. https://doi.org/10.1007/s10439-014-1095-4.
Montes, G. S., and L. C. Junqueira. 1991. “The Use of the Picrosirius-Polarization Method for

the Study of the Biopathology of Collagen." *Memórias Do Instituto Oswaldo Cruz*. https://doi.org/10.1590/S0074-02761991000700002.
Murata, Katsurni, T. Motayama, and C. Kotake. 1986. "Collagen Types in Various Layers of the Human Aorta and Their Changes with the Atherosclerotic Process." *Atherosclerosis* 60 (3): 251–62. https://doi.org/10.1016/0021-9150(86)90172-3.
Nissen, Steven E. 2016. "IVUS Virtual Histology Unvalidated Gimmick or Useful Technique?" *Journal of the American College of Cardiology* 67 (15): 1784–85. https://doi.org/10.1016/j.jacc.2016.02.037.
Ohayon, Jacques, Gilles Rioufol, Olivier Dubreuil, and De Lyon. 2005. "A Three-Dimensional Finite Element Analysis of Stress Distribution in a Coronary Atherosclerotic Plaque:" *Biomechanics Applied to Computer Assisted Surgery* 661 (2): 225–41.
Oie, Tomonori, Yoshinobu Murayama, Toru Fukuda, Chiharu Nagai, Sadao Omata, Keiichi Kanda, Hitoshi Yaku, and Yasuhide Nakayama. 2009. "Local Elasticity Imaging of Vascular Tissues Using a Tactile Mapping System." *Journal of Artificial Organs* 12 (1): 40–46. https://doi.org/10.1007/s10047-008-0440-5.
Ooshima, Akira, and Yasuteru Muragaki. 1990. "Collagen Metabolism in Atherogenesis." *Annals of the New York Academy of Sciences* 598 (1): 582–84. https://doi.org/10.1111/j.1749-6632.1990.tb42355.x.
Opriessnig, Peter, Günther Silbernagel, Stefanie Krassnig, and Gernot Reishofer. 2018. "Magnetic Resonance Microscopy Diffusion Tensor Imaging of Collagen Fibre Bundles Stabilizing an Atherosclerotic Plaque of the Common Carotid Artery." *European Heart Journal* 39 (35): 3337. https://doi.org/10.1093/eurheartj/ehy146.
Pan, Shi. 2009. "Molecular Mechanisms Responsible for the Atheroprotective Effects of Laminar Shear Stress." *Antioxid Redox Sign* 11 (7): 1669–82. https://doi.org/10.1089/ars.2009.2487.
Pan, Yihui, Yuexing Zhan, Huanyun Ji, Xinrui Niu, and Zheng Zhong. 2016. "Can Hyperelastic Material Parameters Be Uniquely Determined from Indentation Experiments?" *RSC Advances* 6 (85): 81958–64. https://doi.org/10.1039/c6ra15747e.
Papafaklis, Michail I., Christos V. Bourantas, Taishi Yonetsu, Rocco Vergallo, Anna Kotsia, Shimpei Nakatani, Lampros S. Lakkas, et al. 2015. "Anatomically Correct Three-Dimensional Coronary Artery Reconstruction Using Frequency Domain Optical Coherence Tomographic and Angiographic Data: Head-to-Head Comparison with Intravascular Ultrasound for Endothelial Shear Stress Assessment in Humans." *EuroIntervention* 11 (4): 407–15. https://doi.org/10.4244/EIJY14M06_11.
Pedrigi, R., R. de Silva, S. M. Bovens, V. V. Mehta, E. Petretto, and R. Krams. 2014. "Thin-Cap Fibroatheroma Rupture Is Associated With a Fine Interplay of Shear and Wall Stress." *Arterioscler Thromb Vasc Biol* 34 (10): 2224–31. https://doi.org/10.1161/ATVBAHA.114.303426.
Pedrigi, Ryan M., Christian Bo Poulsen, Vikram V. Mehta, Niels Ramsing Holm, Nilesh Pareek, Anouk L. Post, Ismail Dogu Kilic, et al. 2015. "Inducing Persistent Flow Disturbances Accelerates Atherogenesis and Promotes Thin Cap Fibroatheroma Development in D374Y-PCSK9 Hypercholesterolemic Minipigs." *Circulation* 132 (11): 1003–12. https://doi.org/10.1161/CIRCULATIONAHA.115.016270.
Pedrigi, Ryan, Vikram V. Mehta, Sandra M. Bovens, Zahra Mohri, Christian Bo Poulsen, Willy Gsell, Jordi L. Tremoleda, et al. 2016. "Influence of Shear Stress Magnitude and Direction on Atherosclerotic Plaque Composition." *Royal Society Open Science* 3 (10): 160588. https://doi.org/10.1098/rsos.160588.
Peiffer, Veronique, Spencer J. Sherwin, and Peter D. Weinberg. 2013. "Does Low and Oscillatory Wall Shear Stress Correlate Spatially with Early Atherosclerosis? A Systematic Review." *Cardiovasc Res* 99 (2): 242–50. https://doi.org/10.1093/cvr/cvt044.
Plodinec, Marija, Marko Loparic, Christophe A. Monnier, Ellen C. Obermann, Rosanna Zanetti-Dallenbach, Philipp Oertle, Janne T. Hyotyla, et al. 2012. "The Nanomechanical Signature of Breast Cancer." *Nature Nanotechnology* 7 (11): 757–65. https://doi.org/10.1038/nnano.2012.167.
Rekhter, MD. 1999. "Collagen Synthesis in Atherosclerosis: Too Much and Not Enough."

Cardiovascular Research, no. 41: 376–84.
Rezvan, Amir, Sanjoli Sur, and Hanjoong Jo. 2015. “Novel Animal Models of Atherosclerosis.” *Biomed Eng Lett* 5 (3): 181–87. https://doi.org/10.1007/s13534-015-0200-4.
Rezvani-Sharif, Alireza, Mohammad Tafazzoli-Shadpour, and Alberto Avolio. 2019a. “Mechanical Characterization of the Lamellar Structure of Human Abdominal Aorta in the Development of Atherosclerosis: An Atomic Force Microscopy Study.” *Cardiovascular Engineering and Technology* 10 (1): 181–92. https://doi.org/10.1007/s13239-018-0370-1.
———. 2019b. “Progressive Changes of Elastic Moduli of Arterial Wall and Atherosclerotic Plaque Components during Plaque Development in Human Coronary Arteries.” *Medical and Biological Engineering and Computing* 57 (3): 731–40. https://doi.org/10.1007/s11517-018-1910-4.
Rhodin, Johannes A. G. 1980. “Architecture of the Vessel Wall.” *Comprehensive Physiology*, 1–31. https://doi.org/10.1002/cphy.cp020201.
Ricard-Blum, Sylvie. 2011. “The Collagen Family.” *Cold Spring Harbor Perspectives in Biology* 3 (1): 1–19. https://doi.org/10.1101/cshperspect.a004978.
Rich, Lillian, and Peter Whittaker. 2005. “Collagen and Picrosirius Red Staining : A Polarized Light Assessment of Fibrillar Hue and Spatial Distribution.” *Braz J Morphol Sci* 22 (2): 97–104. http://jms.org.br/PDF/v22n2a06.pdf.
Richardson, P D, M J Davies, and G V Born. 1989. “Influence of Plaque Configuration and Stress Distribution on Fissuring of Coronary Atherosclerotic Plaques.” *Lancet (London, England)* 2 (8669): 941–44. https://doi.org/10.1016/s0140-6736(89)90953-7.
Ridker, Paul M, Brendan M. Everett, Tom Thuren, Jean G. MacFadyen, William H. Chang, Christie Ballantyne, Francisco Fonseca, et al. 2017. “Antiinflammatory Therapy with Canakinumab for Atherosclerotic Disease.” *New England Journal of Medicine* 377 (12): 1119–31. https://doi.org/10.1056/nejmoa1707914.
Rittie, Laure. 2017. “Method for Picrosirius Red-Polarization Detection of Collagen Fibers in Tissue Sections.” In *Fibrosis: Methods and Protocols, Methods in Molecular Biology*, edited by Springer, 1627:395–407. https://doi.org/10.1007/978-1-4939-7113-8.
Saez, P., E. Pena, and M. A. Martinez. 2014. “A Structural Approach Including the Behavior of Collagen Cross-Links to Model Patient-Specific Human Carotid Arteries.” *Ann Biomed Eng* 42 (6): 1158–69. https://doi.org/10.1007/s10439-014-0995-7.
Schaar, Johannes A., Anton F.W. van der Steen, Frits Mastik, Radj A. Baldewsing, and Patrick W. Serruys. 2006. “Intravascular Palpography for Vulnerable Plaque Assessment.” *Journal of the American College of Cardiology* 47 (8 SUPPL.). https://doi.org/10.1016/j.jacc.2006.01.035.
Schwartz, Stephen M., Renu Virmani, and Michael E. Rosenfeld. 2000. “The Good Smooth Muscle Cells in Atherosclerosis.” *Current Atherosclerosis Reports* 2 (5): 422–29. https://doi.org/10.1007/s11883-000-0081-5.
Segers, Dolf, Frank Helderman, Caroline Cheng, Luc C.A. Van Damme, Dennie Tempel, Eric Boersma, Patrick W. Serruys, et al. 2007. “Gelatinolytic Activity in Atherosclerotic Plaques Is Highly Localized and Is Associated with Both Macrophages and Smooth Muscle Cells in Vivo.” *Circulation* 115 (5): 609–16. https://doi.org/10.1161/CIRCULATIONAHA.106.636415.
Segura, Tatiana, Brian C. Anderson, Peter H. Chung, Rebecca E. Webber, Kenneth R. Shull, and Lonnie D. Shea. 2005. “Crosslinked Hyaluronic Acid Hydrogels: A Strategy to Functionalize and Pattern.” *Biomaterials* 26 (4): 359–71. https://doi.org/10.1016/j.biomaterials.2004.02.067.
Selby, Alastair, Carole Maldonado-Codina, and Brian Derby. 2014. “Influence of Specimen Thickness on the Nanoindentation of Hydrogels: Measuring the Mechanical Properties of Soft Contact Lenses.” *Journal of the Mechanical Behavior of Biomedical Materials* 35: 144–56. https://doi.org/10.1016/j.jmbbm.2013.11.023.
Shah, P. K., E. Falk, J. J. Badimon, A. Fernandez-Ortiz, A. Mailhac, G. Villareal- Levy, J. T. Fallon, J. Regnstrom, and V. Fuster. 1995. “Human Monocyte-Derived Macrophages

Induce Collagen Breakdown in Fibrous Caps of Atherosclerotic Plaques: Potential Role of Matrix-Degrading Metalloproteinases and Implications for Plaque Rupture." *Circulation* 92 (6): 1565–69.
Shekhonin, B. V., S. P. Domogatsky, G. L. Idelson, V. E. Koteliansky, and V. S. Rukosuev. 1987. "Relative Distribution of Fibronectin and Type I, III, IV, V Collagens in Normal and Atherosclerotic Intima of Human Arteries." *Atherosclerosis* 67 (1): 9–16. https://doi.org/10.1016/0021-9150(87)90259-0.
Shim, J., R. H. Al-Mashhadi, C. B. Sørensen, and J. F. Bentzon. 2016. "Large Animal Models of Atherosclerosis - New Tools for Persistent Problems in Cardiovascular Medicine." *Journal of Pathology* 238 (2): 257–66. https://doi.org/10.1002/path.4646.
Sicard, Delphine, Laura E. Fredenburgh, and Daniel J. Tschumperlin. 2017. "Measured Pulmonary Arterial Tissue Stiffness Is Highly Sensitive to AFM Indenter Dimensions." *Journal of the Mechanical Behavior of Biomedical Materials* 74 (February): 118–27. https://doi.org/10.1016/j.jmbbm.2017.05.039.
Small, Donald M. 1988. "Progression and Regression of Atherosclerotic Lesions - Insigths from Lipid Physical Biochemistry." *Arteriosclerosis* 8: 103–29.
Sneddon, Ian N. 1965. "The Relation between Load and Penetration in the Axisymmetric Boussinesq Problem for a Punch of Arbitrary Profile." *International Journal of Engineering Science* 3 (1): 47–57. https://doi.org/10.1016/0020-7225(65)90019-4.
Stone, Gregg W., Akiko Maehara, Alexandra J. Lansky, Bernard De Bruyne, Ecaterina Cristea, Gary S. Mintz, Roxana Mehran, et al. 2011. "A Prospective Natural-History Study of Coronary Atherosclerosis." *New England Journal of Medicine* 364 (3): 226–35. https://doi.org/10.1056/NEJMoa1002358.
Stone, Peter H., Akiko Maehara, Ahmet Umit Coskun, Charles C. Maynard, Marina Zaromytidou, Gerasimos Siasos, Ioannis Andreou, et al. 2018. "Role of Low Endothelial Shear Stress and Plaque Characteristics in the Prediction of Nonculprit Major Adverse Cardiac Events: The PROSPECT Study." *JACC: Cardiovascular Imaging* 11 (3): 462–71. https://doi.org/10.1016/j.jcmg.2017.01.031.
Stone, Peter H., Shigeru Saito, Saeko Takahashi, Yasuhiro Makita, Shigeru Nakamura, Tomohiro Kawasaki, Akihiko Takahashi, et al. 2012. "Prediction of Progression of Coronary Artery Disease and Clinical Outcomes Using Vascular Profiling of Endothelial Shear Stress and Arterial Plaque Characteristics: The PREDICTION Study." *Circulation* 126 (2): 172–81. https://doi.org/10.1161/CIRCULATIONAHA.112.096438.
Stylianou, Andreas, Stylianos Vasileios Kontomaris, Colin Grant, and Eleni Alexandratou. 2019. "Atomic Force Microscopy on Biological Materials Related to Pathological Conditions." *Scanning* 2019. https://doi.org/10.1155/2019/8452851.
Svensson, René B., Tue Hassenkam, Colin A. Grant, and S. Peter Magnusson. 2010. "Tensile Properties of Human Collagen Fibrils and Fascicles Are Insensitive to Environmental Salts." *Biophysical Journal* 99 (12): 4020–27. https://doi.org/10.1016/j.bpj.2010.11.018.
Takeda, Hideo, Kimihiro Komori, Naomichi Nishikimi, Yuji Nimura, Masahiro Sokabe, and Keiji Naruse. 2006. "Bi-Phasic Activation of ENOS in Response to Uni-Axial Cyclic Stretch Is Mediated by Differential Mechanisms in BAECs." *Life Sciences* 79 (3): 233–39. https://doi.org/10.1016/j.lfs.2005.12.051.
Tang, Dale D., and Yana Anfinogenova. 2008. "Physiologic Properties and Regulation of the Actin Cytoskeleton in Vascular Smooth Muscle." *Journal of Cardiovascular Pharmacology and Therapeutics* 13 (2): 130–40. https://doi.org/10.1177/1074248407313737.
Tang, Dalin, Chun Yang, Jie Zheng, Pamela K. Woodard, Gregorio A. Sicard, Jeffrey E. Saffitz, and Chun Yuan. 2004. "3D MRI-Based Multicomponent FSI Models for Atherosclerotic Plaques." *Annals of Biomedical Engineering* 32 (7): 947–60. https://doi.org/10.1023/B:ABME.0000032457.10191.e0.
Teng, Zhongzhao, Adam J Brown, Patrick A Calvert, Richard A Parker, Daniel R Obaid, Yuan Huang, Stephen P Hoole, Nick E J West, Jonathan H Gillard, and Martin R Bennett. 2014. "Coronary Plaque Structural Stress Is Associated with Plaque

Composition and Subtype and Higher in Acute Coronary Syndrome - The BEACON I Study." *Circ Cardiovasc Imaging* 7. https://doi.org/10.1161/CIRCIMAGING.113.001526.
Teng, Zhongzhao, Yongxue Zhang, Yuan Huang, Jiaxuan Feng, Jianmin Yuan, Qingsheng Lu, Michael P.F. Sutcliffe, Adam J. Brown, Zaiping Jing, and Jonathan H. Gillard. 2014. "Material Properties of Components in Human Carotid Atherosclerotic Plaques: A Uniaxial Extension Study." *Acta Biomaterialia* 10 (12): 5055–63. https://doi.org/10.1016/j.actbio.2014.09.001.
Thim, T., M. K. Hagensen, J. F. Bentzon, and E. Falk. 2008. "From Vulnerable Plaque to Atherothrombosis." *Journal of Internal Medicine* 263 (5): 506–16. https://doi.org/10.1111/j.1365-2796.2008.01947.x.
Thim, Troels, Mette Kallestrup Hagensen, David Wallace-Bradley, Juan F. Granada, Greg L. Kaluza, Ludovic Drouet, William P. Paaske, Hans Erik Bøtker, and Erling Falk. 2010. "Unreliable Assessment of Necrotic Core by Virtual Histology Intravascular Ultrasound in Porcine Coronary Artery Disease." *Circulation: Cardiovascular Imaging* 3 (4): 384–91. https://doi.org/10.1161/CIRCIMAGING.109.919357.
Thomas, Hana, Jaime Diamond, Adrianna Vieco, Shaoli Chaudhuri, Eliezer Shinnar, Sara Cromer, Pablo Perel, et al. 2011. "Global Atlas of Cardiovascular Disease 2000-2016: The Path to Prevention and Control." *Global Heart* 13 (3): 143–63. https://doi.org/10.1016/j.gheart.2018.09.511.
Thondapu, Vikas, Christos V. Bourantas, Nicolas Foin, Ik Kyung Jang, Patrick W. Serruys, and Peter Barlis. 2017. "Basic Science for the Clinician: Biomechanical Stress in Coronary Atherosclerosis: Emerging Insights from Computational Modelling." *European Heart Journal* 38 (2): 81–92. https://doi.org/10.1093/eurheartj/ehv689.
Tomaniak, Mariusz, Yuki Katagiri, Rodrigo Modolo, Ranil de Silva, Ramzi Y Khamis, Christos V Bourantas, Ryo Torii, et al. 2020. "Vulnerable Plaques and Patients: State-of-the-Art." *European Heart Journal*, 1–10. https://doi.org/10.1093/eurheartj/ehaa227.
Tracqui, Philippe, Alexis Broisat, Jackub Toczek, Nicolas Mesnier, Jacques Ohayon, and Laurent Riou. 2011. "Mapping Elasticity Moduli of Atherosclerotic Plaque in Situ via Atomic Force Microscopy." *Journal of Structural Biology* 174 (1): 115–23. https://doi.org/10.1016/j.jsb.2011.01.010.
Tulis, David A. 2007. "Histological and Morphometric Analyses for Rat Carotid Balloon Injury Model." *Methods in Molecular Medicine* 139 (919): 31–66. https://doi.org/10.1007/978-1-59745-571-8_2.
Vancraeynest, David, Agnes Pasquet, Véronique Roelants, Bernhard L. Gerber, and Jean Louis J. Vanoverschelde. 2011. "Imaging the Vulnerable Plaque." *Journal of the American College of Cardiology* 57 (20): 1961–79. https://doi.org/10.1016/j.jacc.2011.02.018.
Venkatasubramanian, Ramji T., Erin D. Grassl, Victor H. Barocas, Daniel Lafontaine, and John C. Bischof. 2006. "Effects of Freezing and Cryopreservation on the Mechanical Properties of Arteries." *Ann Biomed Eng* 34 (5): 823–32. https://doi.org/10.1007/s10439-005-9044-x.
Venkatasubramanian, Ramji T., Wim F. Wolkers, Mithun M. Shenoi, Victor H. Barocas, Daniel Lafontaine, Charles L. Soule, Paul A. Iaizzo, and John C. Bischof. 2010. "Freeze-Thaw Induced Biomechanical Changes in Arteries: Role of Collagen Matrix and Smooth Muscle Cells." *Annals of Biomedical Engineering* 38 (3): 694–706. https://doi.org/10.1007/s10439-010-9921-9.
Virmani, Renu, Allen P Burke, Andrew Farb, and Frank D Kolodgie. 2006. "Pathology of the Vulnerable Plaque." *J Am Coll Cardiol* 47 (8 Suppl C): C13-8. https://doi.org/10.1016/j.jacc.2005.10.065.
Virmani, Renu, Allen P Burke, Frank D Kolodgie, and Andrew Farb. 2003. "Pathology of the Thin-Cap Fibroatheroma: A Type of Vulnerable Plaque." *J Interv Cardiol* 16 (3): 267–72. https://doi.org/10.1034/j.1600-0854.2003.8042.x.
Virmani, Renu, Frank D Kolodgie, Allen P Burke, Andrew Farb, and Stephen M Schwartz. 2000. "Lessons From Sudden Coronary Death. A Comprehensive Morphological Classification Scheme for Atherosclerotic Lesions." *Arterioscler Thromb Vasc Biol* 20:

1262–75. https://doi.org/10.1161/01.ATV.20.5.1262.
Vogel, Benjamin, Hanna Siebert, Ulrich Hofmann, and Stefan Frantz. 2015. “Determination of Collagen Content within Picrosirius Red Stained Paraffin-Embedded Tissue Sections Using Fluorescence Microscopy.” *MethodsX* 2: 124–34. https://doi.org/10.1016/j.mex.2015.02.007.
Waksman, Ron, Carlo Di Mario, Rebecca Torguson, Ziad A. Ali, Varinder Singh, William H. Skinner, Andre K. Artis, et al. 2019. “Identification of Patients and Plaques Vulnerable to Future Coronary Events with Near-Infrared Spectroscopy Intravascular Ultrasound Imaging: A Prospective, Cohort Study.” *The Lancet* 394 (10209): 1629–37. https://doi.org/10.1016/S0140-6736(19)31794-5.
Walsh, M. T., E. M. Cunnane, J. J. Mulvihill, A. C. Akyildiz, F. J.H. Gijsen, and G. A. Holzapfel. 2014. “Uniaxial Tensile Testing Approaches for Characterisation of Atherosclerotic Plaques.” *Journal of Biomechanics* 47 (4): 793–804. https://doi.org/10.1016/j.jbiomech.2014.01.017.
Wang, Bao-Wei, Hang Chang, Shankung Lin, Peiliang Kuan, and Kou-Gi Shyu. 2003. “Induction of Matrix Metalloproteinases-14 and -2 by Cyclical Mechanical Stretch Is Mediated by Tumor Necrosis Factor-Alpha in Cultured Human Umbilical Vein Endothelial Cells.” *Cardiovasc Res* 59 (2): 460–69. https://doi.org/10.1016/s0008-6363(03)00428-0.
Wang, Chong, Marisa Garcia, Xiao Lu, Yoram Lanir, and Ghassan S. Kassab. 2006. “Three-Dimensional Mechanical Properties of Porcine Coronary Arteries: A Validated Two-Layer Model.” *American Journal of Physiology - Heart and Circulatory Physiology* 291 (3): 1200–1209. https://doi.org/10.1152/ajpheart.01323.2005.
Wegner, Kyle A., Adib Keikhosravi, Kevin W. Eliceiri, and Chad M. Vezina. 2017. “Fluorescence of Picrosirius Red Multiplexed With Immunohistochemistry for the Quantitative Assessment of Collagen in Tissue Sections.” *Journal of Histochemistry and Cytochemistry* 65 (8): 479–90. https://doi.org/10.1369/0022155417718541.
Wenger, Marco P.E., Laurent Bozec, Michael A. Horton, and Patrick Mesquidaz. 2007. “Mechanical Properties of Collagen Fibrils.” *Biophysical Journal* 93 (4): 1255–63. https://doi.org/10.1529/biophysj.106.103192.
Wentzel, Jolanda J., Yiannis S. Chatzizisis, Frank J H Gijsen, George D. Giannoglou, Charles L. Feldman, and Peter H. Stone. 2012. “Endothelial Shear Stress in the Evolution of Coronary Atherosclerotic Plaque and Vascular Remodelling: Current Understanding and Remaining Questions.” *Cardiovasc Res* 96 (2): 234–43. https://doi.org/10.1093/cvr/cvs217.
Winkel, Leah C., Ayla Hoogendoorn, Ruoyu Xing, Jolanda J. Wentzel, and Kim Van der Heiden. 2015. “Animal Models of Surgically Manipulated Flow Velocities to Study Shear Stress-Induced Atherosclerosis.” *Atherosclerosis* 241 (1): 100–110. https://doi.org/10.1016/j.atherosclerosis.2015.04.796.
Wonseok, Lee, Lee Hyungbeen, Lee Gyudo, and Yoon Dae Sung. 2016. “Advances in AFM Imaging Applications for Characterizing the Biophysical Properties of Amyloid Fibrils.” In *Intech*, 13. https://www.intechopen.com/books/advanced-biometric-technologies/liveness-detection-in-biometrics.
Zhang, Shuai, Maria Andreasen, Jakob T. Nielsen, Lei Liu, Erik H. Nielsen, Jie Song, Gang Ji, et al. 2013. “Coexistence of Ribbon and Helical Fibrils Originating from HIAPP 20-29 Revealed by Quantitative Nanomechanical Atomic Force Microscopy.” *Proceedings of the National Academy of Sciences of the United States of America* 110 (8): 2798–2803. https://doi.org/10.1073/pnas.1209955110.
Zhao, Yutong, Peter V. Usatyuk, Irina A. Gorshkova, Donghong He, Ting Wang, Liliana Moreno-Vinasco, Alison S. Geyh, et al. 2009. “Regulation of COX-2 Expression and IL-6 Release by Particulate Matter in Airway Epithelial Cells.” *American Journal of Respiratory Cell and Molecular Biology* 40 (1): 19–30. https://doi.org/10.1165/rcmb.2008-0105OC.
Zoumi, Aikaterini, Xiao Lu, Ghassan S. Kassab, and Bruce J. Tromberg. 2004. “Imaging Coronary Artery Microstructure Using Second-Harmonic and Two-Photon Fluorescence

Microscopy.” *Biophysical Journal* 87 (4): 2778–86. https://doi.org/10.1529/biophysj.104.042887.